Master's thesis

NTNU
Norwegian University of Science and Technology
Faculty of Social and Educational Sciences
Department of Geography

Einar Torjul Trøen Rufsvoll

Landslides in Brumunddalen Area, Norway; Evidence of Post-Glacial Earthquakes

A GIS and Field Study

Master's thesis in Geography with Teacher Education
Supervisor: Ola Fredin

May 2021

NTNU
Norwegian University of Science and Technology

Einar Torjul Trøen Rufsvoll

Landslides in Brumunddalen Area, Norway; Evidence of Post-Glacial Earthquakes

A GIS and Field Study

Master's thesis in Geography with Teacher Education
Supervisor: Ola Fredin
May 2021

Norwegian University of Science and Technology
Faculty of Social and Educational Sciences
Department of Geography

NTNU
Norwegian University of
Science and Technology

To cite this master thesis: Rufsvoll, E. T. T. (2021). *Landslides in Brumunddalen Area, Norway; Evidence of Post-Glacial Earthquakes.* Master thesis in Geography with Teatcher Education. Department of Geography. Norwegian University of Sience and Technology

For å sitere denne masteroppgaven: Rufsvoll, E. T. T. (2021). *Landslides in Brumunddalen Area, Norway; Evidence of Post-Glacial Earthquakes.* Masteroppgave for lektor i geografi. Geografisk institutt. Norges teknisk-naturvitenskapelige universitet, Trondheim

Abstract

The presence of seismically induced landslides is well documented and discussed in literature worldwide. It has become clear that liquefaction as a result of seismic shaking is valid and quite common. In Norway, Sweden, and Finland, faults and landslide scars have been tied to the seismic activity caused by the glacial isostatic adjustment following the deglaciation of Fennoscandia. This thesis aims to figure out if landslide scars in the area around Brumunddalen, Norway, was derived through landslides triggered by post-glacial seismicity or if other processes can explain the abundance of landslide scars.

The results presented were derived through Fieldwork, GIS analysis and sediment analysis. During the fieldwork, sediment samples were collected, slopes were measured, and topography observed. The GIS analysis consisted of mapping the landslide scars, measuring slopes and analysing data layers. The sediment samples collected were processed through dry sieving to obtain the soil's grain size distribution.

Slope failure due to "normal" gravitational processes is generally not expected in slopes with an inclination under 25 – 30°. The slope inclination measured in GIS and during the fieldwork was, for the most part, gentler. In GIS, the general slope inclination was measured to approximately 6°. The sediment analysis disclosed that the grain size distribution fit the grain size graph plotted in other studies where similar material liquefied due to seismicity. The fractions of silt and sand also resembled that presented in studies of liquefied materials.

The results and theory indicate that the slopes are too gentle for slope failure to occur due to normal gravitational processes. Therefore, it is fair to assume that another factor has played a part in triggering the slope failure. As the soil exhibits characteristics similar to that of other liquefied areas, this might explain landsliding in gentle terrain. The research presents results posing arguments for landsliding due to post-glacial seismicity, but further research is required to rule out other triggering factors.

Keywords: *Geographical information systems, Sediment analysis, Grain size distribution, Fieldwork, Post-glacial seismicity, Landsliding.*

Sammendrag

Skred forårsaket av seismisk aktivitet er godt dokumentert i forskning fra hele verden, og man har kommet til enighet om at seismisk aktivitet kan få sedimenter til å likvifere, noe som kan føre til skred i relativt slakt terreng. Studier fra blant annet Norge, Sverige og Finland har funnet at isostatisk justering forårsaket av deglasiasjonen av Fennoskadia har resultert i seismisk aktivitet, forkastninger og skred. Denne masteroppgaven har som mål å finne ut om skredsårene man kan finne i området rundt Brumunddalen kan være forårsaket av postglasial seismisitet, eller om andre mekanismer har utløst disse skredene.

Feltarbeid, GIS analyse og sedimentanalyse er blant metodene som er tatt i bruk for å komme nærmere et svar på om postglasial seismisitet kan ha vært en utløsende faktor for skred i dette området. Feltarbeidet bestod av å samle sedimentprøver, måle skråningshellninger og observere områdets topografi. GIS analysen bestod av å kartlegge skredsår, måle skråningshellning og analysere datalag. Sedimentanalysen ble gjennomført for å kunne si noe om løsmassenes stabilitet og sannsynlighet for å likvifere.

Skred grunnet «vanlige» gravitasjonsprosesser forventes vanligvis ikke i skråninger med hellning under 25 – 30°. Majoriteten av skråninger målt i området var slakere enn dette, generellt sett rundt 6°. Sedimentanalysen avslørte at kornstørrelsesfordelingen av prøvene lignet de målt i lignende studier. Sedimentprøvenes silt og sand prosent var sammenfalte med det målt i områder hvor overflatematerialet har likvifert.

Resultatene fra forskningsarbeidet, med bakgrunn i teorien som er presentert og lignende studier, viser at skråningshellningen i området generelt sett er for slak til at normale gravitasjonsprosesser kan ha forårsaket skred. Det kan derfor forventes at andre prosesser har vært med å utløse skredene. Kornstørrelsesfordelingen ligner den funnet i andre områder hvor likvifaksjon har forårsaket skred i relativt slakt terreng. Det kan altså argumenteres for at postglasial seismisitet har forårsaktet likvifaksjon i området, som kan forklare det store antallet skressår, men videre forskning bør gjennomføres for å styrke mistanken.

Nøkkelord: *Geografiske informasjonssystemer, Sedimentanalyse, Kornstørrelsesfordeling, Feltarbeid, Postglasial seismisitet, Skred*

Acknowledgement

I would like to thank my supervisor Ola Fredin (PhD), for the immense support throughout the research and writing of the thesis. His contributions to the planning of fieldwork, sieving analysis, GIS mapping and analysis, and writing and constructing this thesis has been invaluable. His first-hand knowledge in the field and experience with writing has elevated the quality of my work. Furthermore, he has been of great moral support in ups and downs in the process. I would also like to thank the researchers at NGU (Norwegian geological surveys) for providing the datasets of grain size distribution and landslides mapped.

I would further like to thank Vibeke Uthaug (fellow master student at NTNU) for ten incredible days in field. She was of great help when sediment samples were collected and documented and of great support through the cold and rainy days.

Furthermore, I would like to show my greatest appreciations to Camilla Finnstad Pedersen for taking the time to proofread my thesis and ensure the quality of the language throughout it.

Finally, I would like to thank friends, family, and my better half for the moral support, and uplifting words.

Table of Contents

ABSTRACT ..... **VII**
SAMMENDRAG ..... **IX**
ACKNOWLEDGEMENT ..... **XI**
LIST OF FIGURES ..... **XV**
LIST OF TABLES ..... **XIX**
ABBREVIATION ..... **XXI**
CHAPTER 1 INTRODUCTION **1**
CHAPTER 1.1 COMPREHENSIVE RESEARCH QUESTION 3
Chapter 1.1.1 Subordinate Questions *3*
CHAPTER 1.2 RELEVANCE FOR TEACHER PROFESSION 4
CHAPTER 2 GEOLOGICAL SETTING **6**
CHAPTER 2.1 BEDROCK 8
CHAPTER 2.2 SURFICIAL DEPOSITS 9
CHAPTER 3 THEORY **10**
CHAPTER 3.1 GIS 10
Chapter 3.1.1 Raster and Vector *10*
Chapter 3.1.2 LiDAR *12*
Chapter 3.1.3 Digital Elevation Model (DEM) and Remote Sensing *14*
Chapter 3.1.4 Interpolating *15*
Chapter 3.1.5 Data processing and analysis in GIS *17*
CHAPTER 3.2 SEDIMENT SAMPLING 20
Chapter 3.2.1 Size of sediment sample *20*
Chapter 3.2.2 Analysing sediment samples *21*
CHAPTER 3.3 LITERATURE REVIEW OF IMPORTANT EARTH SCIENCE CONCEPTS 23
Chapter 3.3.1 Glacial isostasy and rebound *23*
Chapter 3.3.2 Post-glacial Earthquakes *25*
Chapter 3.3.3 Liquefaction *28*

Chapter 3.3.4 Landslides and "normal" slope processes *30*
CHAPTER 4 METHODS AND MATERIALS **32**
CHAPTER 4.1 TOOLS AND PROCESSES IN ARCGIS PRO – BEFORE FIELDWORK 33
CHAPTER 4.2 FIELDWORK 35
Chapter 4.2.1 Preparation *35*
Chapter 4.2.2 Fieldwork and sampling *36*
CHAPTER 4.3 GRAIN SIZE DISTRIBUTION 38
Chapter 4.3.1 Procedure *38*
CHAPTER 4.4 TOOLS AND PROCESSES IN ARCGIS PRO – AFTER FIELDWORK 41
Chapter 4.4.1 Cut and fill *41*
CHAPTER 5 RESULTS **42**
CHAPTER 5.1 FIELDWORK OBSERVATIONS 43
CHAPTER 5.2 GIS ANALYSIS 47
Chapter 5.2.1 Hillshade and manual mapping *47*
Chapter 5.2.2 Slope inclination *48*
Chapter 5.2.3 Cut Fill *50*
CHAPTER 5.3 GRAIN SIZE ANALYSIS 54
Chapter 5.3.1 NGUs sediment samples and grain size distribution *67*
CHAPTER 6 DISCUSSION **71**
CHAPTER 7 LIMITATIONS AND FUTURE WORK **84**
CHAPTER 8 CONCLUSION **85**
REFERENCES **87**
CHAPTER 9 APPENDIX 1 ..... **1**

List Of Figures

Figure 1 Overview over post-glacial faults, landslides, and possible post-glacial faults in Norway, Sweden, and Finland (From: Lagerbäck & Sundh, 2008) 1

Figure 2 Overview map. The purple polygon represents the studied area, while the other polygons represent where sliding due to post-glacial seismicity may have occurred elsewhere in Norway. All polygons are drawn on the border for each municipality except Haram municipality (Light green) and the studied area (Purple). Haram Municipality was absorbed by Ålesund municipality in 2020, and the polygon for the studied area consists of multiple municipalities in Innlandet county (data derived from Kartverket.no). 6

Figure 3 Bedrock map illustrating the main rock types dominating the different areas surrounding Brumunddalen. The data is collected and supplied by NGU, but modified to use in this thesis. Different types of sandstone, limestone, gneiss were merged together into separate classes. Some rock types were placed into the category "other" to clarify the cartographic design (Data from NGU) 8

Figure 4 Surficial deposits map. Data collected and distributed by NGU. 9

Figure 5 Schematic illustration of Vector and Raster. 10

Figure 6 Illustration of how LiDAR points typically are collected. Two GPS stations, an INS and a laser scanner emitting light pulses perpendicular to the direction of the aircraft (From: Rombouts, 2006) 12

Figure 7 Multiple feedbacks from one imaginary laser puls when conducting a LiDAR scanning. Return 1- 3 is a branch from a tree, return 4 is a bush, and the last return is the ground. Return 1-4 does not return the entire laser puls, but some of it passes on to the next surface – giving multiple returns (From: Michez et al., 2016). 13

Figure 8 Data stack of layers created using a point cloud derived from a LiDAR scanning. The bottom to the top is an orthophoto, rectified/georeferenced using DEM, DTM colour coded with elevation data, DSM LiDAR-derived forest coverage and contour lines (From: MSDI, 2021) 14

Figure 9 Points used from a LiDAR scanning to create a DSM and DTM. The blue dots represent the points, and the red line the continuous raster (From: CHARIM, 2021). 14

Figure 10 Thiessen Polygon – The polygon's point determines the values for all points within the polygon leading to a sharp/distinct transition between areas. (From: Geowizzard, 2021) 16

Figure 11 Kriging – Each of the adjacent points (Blue) are weighted according to proximity and degree of variation between the different points to create a value for the point missing value (red)(From: Esri, 2016) 17

Figure 12 Illustration of DTM to Hillshade for visual analysis. Hillshade created with Azimuth 315° and Altitude 45°. The same extent and location used in both DTM and Hillshade. 18

Figure 13 Illustration of how cut and fill works. a) is the cross section of the valley before, b) is a cross section of the valley after, and c) after the two profiles are run in cut fill in ArcGIS Pro. Red illustrates where mass gain has occurred, and blue where mass is lost. (From: Esri, 2021f) 19

Figure 14 Examples of percentage passing plotted in a scatterplot where A) illustrates a well graded soil B) illustrates a uniformly graded soil distribution, C) illustrate a gap graded soil distribution (From: Sivakugan & Das, 2009) 22

Figure 15 Illustration of a well-graded soil sample and how the size of different soil types can be distinguished from one another. Exemplifies the D10, D20, D30, D50 and D60 value for the soil sample (From: Fredlund et al., 2000). Clay, silt and sand approximations added to the figure. 22

Figure 16 Illustration of the crust-mantle equilibrium and the effect of crustal loading/unloading on the mantle flow. When mass is added to the crust, the crust is pushed down to satisfy the equilibrium, and mantle flow (green arrows) is directed outward. When crustal unloading is happening, crustal rebound (black arrows) occurs, and slow mantle flow fill the void to satisfy the equilibrium (From: Earle & Vancouver Island university, 2019) 23

Figure 17 Illustration of ice sheets effect on the isostatic adjustment and crust-mantle equilibrium. Black arrows illustrate the direction in which the crust is forced (From: Wolf, 1993) 24

Figure 18 Seismic activity (Measured 1980-2012) in Fennoscandia (From: Keiding et al., 2018) 26

Figure 19 Flow failure diagram. When liquefaction occurs beneath the topmost layer of the surface, soil loses strength and flows down as a slope as a viscous mass. Soil stabilises when the pore water escapes and becomes stable once again. A) Prior to sliding. B) Earthquake shakes the ground and triggers liquefaction. C) Liquefied material relaxes. D) Present day situation (From: Lagerbäck & Sundt, 2008) 29

Figure 20 simplified overview of the overall workflow. 32

Figure 21 ArcGIS Pro workflow - most processes included. 33

Figure 22 Mosaic raster data to new cohesive raster (From: Gisgeography, 2020) 33

Figure 23 Picture from sampling point were not suitable for sampling or sieving analysis 36

Figure 24 Overview of the sampling procedure in field.Green circle: bigger rocks manually sorted out. Blue circle: intact surface cover to cover up after digging. Red circle: plastic bags to store samples and field notebook. Purple circle: Sampling hole. Orange circle: shovels to dig the hole. Pink circle: Gardening shovel to collect the sample. Yellow circle: tarpaulin to collect sediments. 37

Figure 25 Stacked sieves, mallet, brush, weight, spoon, brush, spreadsheet and samples used in sieving analysis 39

Figure 26 Mechanic shaker used in the sieving analysis 40

Figure 27 Samples before (to the left) and after (to the right) sieving 40

Figure 28 Picture from fieldwork. Illustrates the inclination in the area as well as the overall vegetation 43

Figure 29 Pit dug for sediment sampling 43

Figure 30 Hillshade landslide mapping and sampling points 45

Figure 31 Map showing the area where only slope measurement was conducted and not sediment sampling 46

Figure 32 Slope inclination in ° over the sampled area. 48

Figure 33 Slope map overview 49

Figure 34 Histogram of the slope inclination values in °. The normal distribution is marked by a black line and x 50

Figure 35 Cut fill landslide 1 51

Figure 36 Cut fill landslide 2 52

Figure 37 Cut fill landslide 3 53

Figure 38 Overview of the sampling points. The colour of the border on each of the hillshades coincides with that of the extent indicator in the navigation map. 54

Figure 39 Logarithmic grain size distribution chart - all samples 54

Figure 40 Location of sampling point 1.1.1, 1.2.1 and 1.3.1. Black square is the extent indicator showing where the sample is collected. 56

Figure 41 Percentage finer plotted in a logarithmic scatterplot graph with D10-, D30-, D50-, and D60-values. 57

Figure 42 Percentage finer plotted in a logarithmic scatterplot graph with D10-, D30-, D50-, and D60-values. 58

Figure 43 Percentage finer plotted in a logarithmic scatterplot graph with D10-, D30-, D50-, and D60-values. 59

Figure 44 Location of sampling point 2.1.2, 2.2.2 and 2.3.2. Black square is the extent indicator showing where the sample is collected. 60

Figure 45 Percentage finer plotted in a logarithmic scatterplot graph with D10-, D30-, D50-, and D60-values. 61

Figure 46 Location of sampling point 2.2.3 and 2.1.3. Black square is the extent indicator showing where the sample is collected. 62

Figure 47 Percentage finer plotted in a logarithmic scatterplot graph with D10-, D30-, D50-, and D60-values. 63

Figure 48 Percentage finer plotted in a logarithmic scatterplot graph with D10-, D30-, D50-, and D60-values. 64

Figure 49 Location of sampling point 4.1.4. Black square is the extent indicator showing where the sample is collected. 65

Figure 50 Percentage finer plotted in a logarithmic scatterplot graph with D10-, D30-, D50-, and D60-values. 66

Figure 51 Percentage finer plotted in a logarithmic scatterplot graph with D10-, D30-, D50-, and D60-values. 67

Figure 52 Percentage finer plotted in a logarithmic scatterplot graph with D10-, D30-, D50-, and D60-values. 68

Figure 53 Percentage finer plotted in a logarithmic scatterplot graph with D10-, D30-, D50-, and D60-values. 69

Figure 54 Percentage finer plotted in a logarithmic scatterplot graph with D10-, D30-, D50-, and D60-values. 70

Figure 55 Landslides mapped in Sweden (SGU, 2016). Orange circle is the mapped and studied area around Brumunddalen. Blue dots (spår av jordskred I moränmark/traces of slides in morain surface) is the most interesting in regards to the results presented in thiis thesis 71

Figure 56 Fennoscandian ice thickness (in m) and extent during the LGM (From Holger & Wu, 2011). Orange circle contains the studied area around Brumunddalen, and some of the area shown in Figure 55. 72

Figure 57 Illustration of where sliding has cut off landforms and cluster of sliding incidences. a) illustrates an area where sliding incidences are especially clustered together and not only at the base of the slope as per criterion (4) in Jibson (2009) and Jibson (2009) in general. At closer inspection it appears as if the landslide scars cuts drumlins, implying that landslide activity happened after the deglaciation b) shows where the landslide deposit partly overlays what looks like an esker meaning the sliding has happened after the ice cover melted away (Orange circle esker as a whole. Yellow circle where the esker is cut of) 77

Figure 58 Landslides mapped by Palmu et al. (2015). The white arrows point at the landslide scars, and the yellow star indicates the drilling location. The blue area is the lowest rising surface at 181 masl. while the red is highest rising 531 masl. (From Palmu et al., 2015) 80

Figure 59 Suspected earth ovens in the Brumunddalen area. Circles mark where earth ovens are present 82

List of Tables

Table 1 Lists the inclination of the area around where sediment samples were collected and the area around landslide scars where only inclination was measured. The inclination values are presented in °. Some additional information on the quality of the sample is also provided. ... 42

Table 2 Cut and fill values landslide 1 51

Table 3 Cut and fill values landslide 2 52

Table 4 Cut and fill values landslide 3 53

Abbreviation

DEM – digital elevation model

DSM – Digital surface model

DTM – Digital terrain model

Esri - Environmental System Research Institutes

GIA – Glacial isostatic adjustment

GIS – Geographical information systems

GPS – Global positioning system

IDW – Inverse-Distance Weight

IMU – Inertial measurement unit

INS – Inertial navigation system

LGM – Last glacial maximum

LiDAR – Light detection and ranging

M – Magnitude

NGU –Norges geologiske undersøkelser

NVE –Norges Vassdrags-og Energidirektorat

PGS – Post-glacial seismicity

PGU – Post-glacial uplift

UiB – University of Bergen

UTM–Universal Transverse Mercator

WGS –World Geodatic System

Chapter 1 Introduction

Norway and Scandinavia are far away from major tectonic boundaries, and the possibility of strong seismic activity may thus seem unlikely (Dehls et al., 2000; Bungum et al., 2010). However, in more recent years, intraplate seismicity has been recorded in Scandinavia (Dehls et al., 2000). As illustrated in Figure 1 and Figure 2, these areas include the north of Finland, central and northern parts of Sweden and Finnmark, Rana, Møre og Romsdal, Vestland, and areas around Oslo in Norway (Olesen et al., 2000; Olesen et al., 2003; Lagerbäck & Sundh, 2008; Olesen et al., 2013; Smith et al., 2014; Sutinen et al., 2014; Mikko et al., 2015; Palmu et al., 2015; Mangerud et al., 2018). In the research from our neighbouring countries, Sweden and Finland, extensive geographical information system (GIS) and remote sensing mapping and fieldwork have been conducted to uncover the triggering mechanisms of the sliding incidents. From the research, it becomes clear that post-glacial seismicity (PGS) due to glacial isostatic adjustment (GIA) is a real and relatively common process. The mapping of parts of Sweden and Finland suggests that

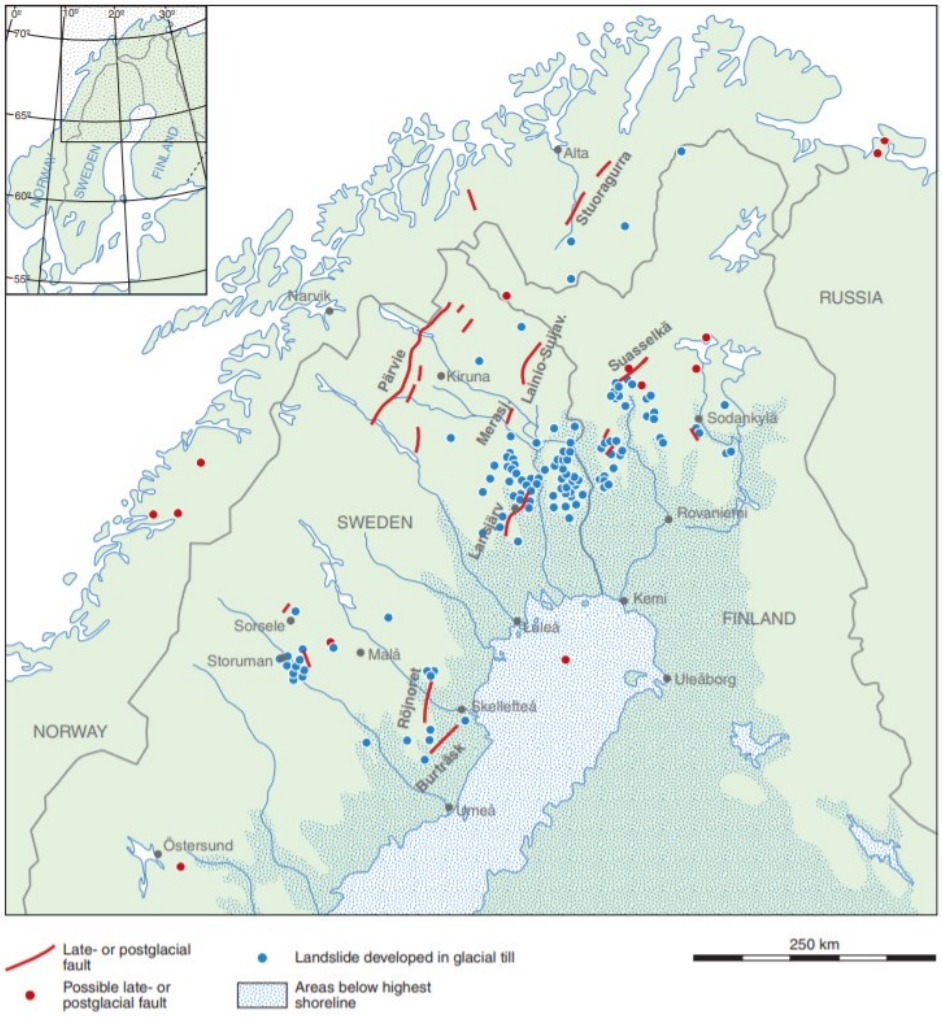

Figure 1 Overview over post-glacial faults, landslides, and possible post-glacial faults in Norway, Sweden, and Finland (From: Lagerbäck & Sundh, 2008)

landslides and faulting in areas where the conditions usually do not result in faulting and sliding due to normal slope processes show that PGS due to GIA is the most probable cause (Smith et al., 2014; Mikko et al., 2015; Palmu et al., 2015). Recently, researchers at the Geological Survey of Norway (NGU) and the University of Bergen (UiB) have mapped a large number of landslides tentatively tied to post-glacial seismicity in the Brumunddalen area (Personal communication O.Fredin, 2021). However, further research is required to determine the likelihood of PGS as the cause of the sliding.

Up until quite recently, aerial photography was the only source for mapping many features on the Earth's surface – for instance topography, land use, geology and change detection. New technology, such as Light detection and ranging (LiDAR), has, to some degree, made aerial photographs redundant (Harvey & Hill, 2001; Lang & McCarty, 2009; Scheiber et al., 2015; Palmu et al., 2015). The data collected through aerial photography has had great success in mapping many features on the Earth's surface. However, aerial photography often does not reveal small landforms in densely forested areas due to vegetation obscuring the process. Recent advances in LiDAR technology has made mapping of these areas possible (Harvey & Hill, 2001; Lang & McCarty, 2009; Su et al., 2016). The implementation of LiDAR as a data source in Norway started around the year 2007, and in 2016, Kartverket (the Norwegian mapping authorities) started a project called "prosjektet nasjonal detaljert høydemodell" (Project national detailed height model (*my translation*)) to ensure the best possible coverage. At the time of writing, Kartverket has covered most of Norway, including the studied area for this thesis (Kartverket, 2020b). The new LiDAR data collected results in a high resolution dataset with a resolution of 50 points per m^2 to two points per m^2, which makes it possible to work in three dimensions – height, width and elevation (Christensen, 2016).

GIS software is generally accepted as one of the primary means of digital spatial analysis. There is a widespread agreement that the analysis of patterns and relationships should be a central function in GIS. For a long time, researchers have developed different spatial analysis methods through GIS. Previously, GIS was mostly used as a statistical tool, as a means to classify clusters or categorise different features and objects on the Earth's surface (Cope & Elwood, 2009, pp. 1-3; Bayley, 2013; Teixeira, 2016). However, the trend is to utilise GIS as a qualitative method wherein it is an addition to or a replacement for fieldwork. The Qualitative GIS is a mixed-method GIS, implementing multiple methods to unveil the truth. A problem with this approach is that different methods can reach different conclusions or

processes, leading qualitative GIS to shift the research. One of the advantages of mixed methods is that knowledge in science tends to be viewed as partial. One can never know the whole truth, and applying multiple methods is a technique to get closer to the absolute truth. Qualitative GIS is further based on the notion that mixed methods build on the relation of epistemology and methods, and that most scientific findings and knowledge are, to some degree, political. Using mixed methods is a way to ensure the quality of knowledge and results derived from the research (Cope & Elwood, 2009, pp. 1-3; Bayley, 2013; Teixeira, 2016).

In general, this paper aims to uncover if landsliding due to PGS has happened in the area around Brumunddalen in south-central Norway. There are many different ways to uncover the likelihood of landsliding due to PGS, and this research has mainly focused on GIS analysis, fieldwork, grain size analysis and literature study to find an answer to the hypothesis. The fieldwork conducted consisted of retrieving sediment samples from interesting areas, measuring slope incline, and observing the area in general. A spatial analysis was conducted through the use of ArcGIS Pro®. In addition to ArcGIS Pro®, ArcMap® and Survey123® were used to collect locations and measurements during the fieldwork. The samples collected during the fieldwork went through dry sieving to determine the ratios of different grain size fractions in the samples. Furthermore, a literature study was conducted to compare results and findings with similar studies in Norway and other areas.

Chapter 1.1 Comprehensive Research Question

There is a large number of landslide scars in the thick till deposits in the Brumunddalen area. This thesis will map and characterise these fossil landslides through the use of GIS analysis of high-resolution digital terrain models (DTM), field mapping, and characterisation of soil samples. This is done to test the following hypothesis: ***Most or all of these landslide scars were derived through landslides triggered by post-glacial seismicity (earthquakes)***.

Chapter 1.1.1 Subordinate Questions

The main research question is broad and comprehensive. To determine whether or not most or all of these landslide scars were derived through post-glacial seismicity (earthquakes), all possible explanations for the sliding that has occurred in Brumunddalen needs to be

researched, and a wide variety of slides needs to be researched. The extent of a master thesis is not suitable to give a complete and comprehensive answer to this, but instead, start the research. A break-down of the hypothesis is therefore presented in the following four bullet points. This is done to narrow the extent of research and be able to provide some quality instead of quantity of findings.

1. Is the terrain in the area surrounding Brumunddalen steep enough for "normal" gravitational landslide processes to occur, or is post-glacial seismicity a more likely mechanism?

2. Can the landslides be tied to the time after the last glacial maximum and deglaciation of the Fennoscandian ice sheet?

3. Is the grain size distribution of the sediment samples from Brumunddalen distributed in a way that liquefaction of the soil due to an earthquake could have occurred?

4. Does the area around Brumunddalen resemble other Scandinavian areas susceptible to post-glacially induced earthquakes?

Chapter 1.2 Relevance for Teacher Profession

As the thesis forms a part of a **masters degree in geography with teacher education**, it is natural to look at how this thesis can be relevant to the teaching profession. In Norway, the curriculum is divided into multiple chapters, some of which are supposed to be implemented in all subjects and some for each respective subjects with *competency aims* that students are supposed to meet at the end of each education component. The Norwegian education system is divided into primary school (1-4 grade and 5-7 grade), lower secondary school (8-10 grade) and upper secondary school (1-3 grade), where the curriculum has different goals throughout the education system. Geography consists as part of social studies in primary- and lower secondary school; however, it is its own subject in upper secondary school.

This thesis is relevant for the teaching profession through multiple chapters in the curriculum. The first chapter is *basic skills,* where digital skills are weighted (Kunnskapsdepartementet, 2020). In the previous curriculum (LK06) (Valid for 2. Grade in upper secondary school until

01.08.2021), competence related to geographic sources and tools is among the main goals. The goal includes reading and using maps, simple map analysis, and GIS and digital maps (Utdanningsdirektoratet, 2006). Therefore, the argument that these goals still are important can be made. Understanding, analysing and producing maps is an essential tool in the geographical world. It is used to conduct fieldwork, analyse landforms and analyse social phenomena in relation to place. In a continuously digitalising world, most maps used in everyday life are digital; therefore, mastering GIS and spatial data sources is vital in the teaching profession.

In upper secondary school, geography is its own subject, not part of social studies. The curriculum specifies many *competency aims*, and more than a few themes are covered throughout the research conducted in this thesis. Some of those *competency aims* are listed below (the most relevant part is emphasised using bold lettering). Throughout the research conducted in this thesis, fieldwork, spatial analysis in GIS, grain size distribution and literature studies, skills and knowledge relevant to teaching about these themes were acquired. A deep and comprehensive understanding of many processes implemented in these *competency aims* is beneficial when compiling educational activities. The first-hand knowledge of all parts of conducting fieldwork, preparation, execution and the concluding and presenting is an opportunity to implement innovative education methods.

- To **explore and present geographical conditions and processes** using different sources, including **maps** (Utdanningsdirektoratet, 2020/2021, *my translation*).
- **Explain how inner and outer forces have influenced the landscape,** and explore and give examples of how humans use these resources (Utdanningsdirektoratet, 2020/2021, *my translation*).
- **Explore and explain the causes of a current natural-** or environmental **disaster** and the **consequences for humans, society and nature** (Utdanningsdirektoratet, 2020/2021, *my translation*).
- **Conduct fieldwork to investigate and present geographical conditions** (Utdanningsdirektoratet, 2020/2021, *my translation*).

Chapter 2 Geological Setting

The fieldwork, sediment sampling and GIS analysis took place in the area around Brumunddal. Brumunddal is the largest settlement in Ringsaker municipality and is located approximately 60.88° North and 10.93° East, between Lillehammer and Hamar. Brumunddalen is situated at the north end of Mjøsa, Norway's biggest lake, which is mainly surrounded by agricultural lands and forests. Brumunddalen is relatively small compared to other Norwegian cities with a population of about 10 919 (2020) (Store Norske Leksikon, 2020a), but has the largest population in Ringsaker – total population of 34 488 (Store Norske Leksikon, 2020b).

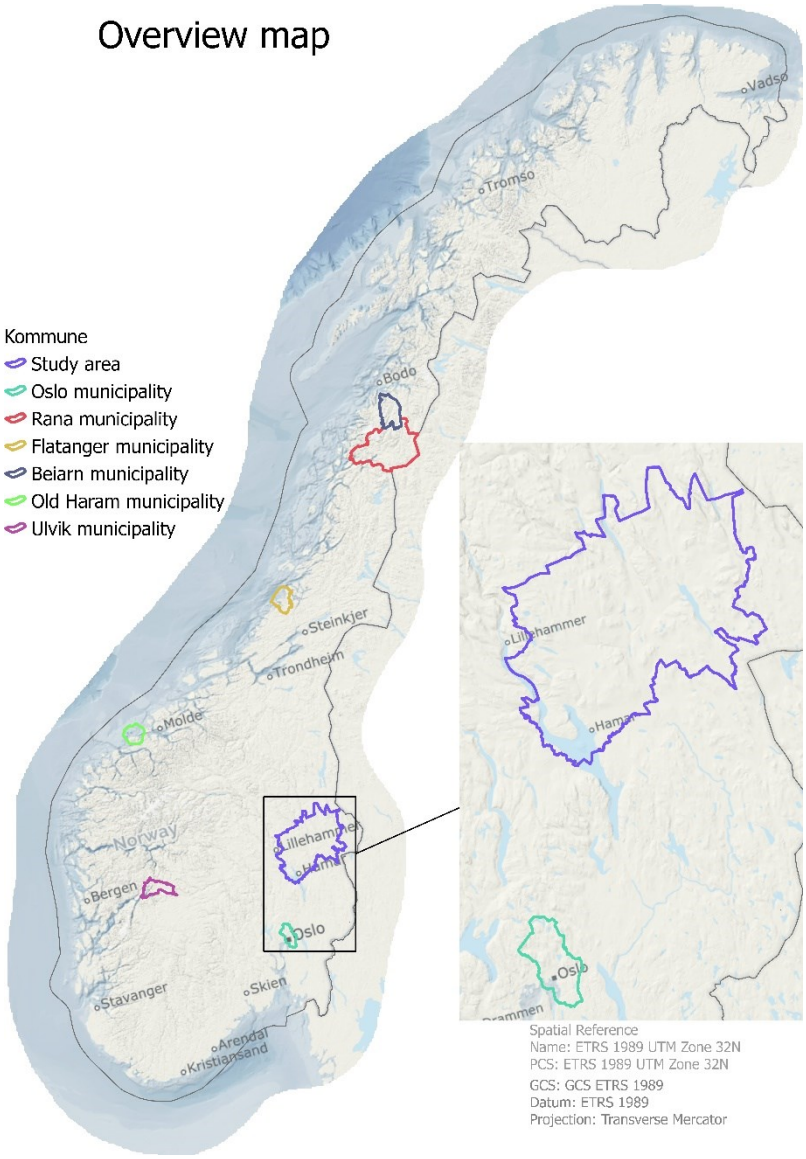

Figure 2 Overview map. The purple polygon represents the studied area, while the other polygons represent where sliding due to post-glacial seismicity may have occurred elsewhere in Norway. All polygons are drawn on the border for each municipality except Haram municipality (Light green) and the studied area (Purple). Haram Municipality was absorbed by Ålesund municipality in 2020, and the polygon for the studied area consists of multiple municipalities in Innlandet county (data derived from Kartverket.no).

In Norway, since after the second world war, geomorphical mapping has been carried out using Aerial Photography (Chapter 3.1.2) and field reconnosaince, including landforms and deposits from within the fields of glacial, fluvial, slope and geohazards (Sollid et al., 1973; Sollid & Sørbel, 1994; Andersen et al., 1995). However, identification and mapping of landforms are hampered in aerial photographs due to vegetation cover (Harvey & Hill, 2001; Aronoff & Petrie, 2005, pp. 230-231; Liu, 2008; Mallet & Bretar, 2009). By using LiDAR,

the GIS operator can effectively strip away vegetation cover and see an undisturbed view of the land surface, such that landforms are much easier recognised and mapped. It is thus likely that there are still many undetected landforms in the Norwegian landscape that will emerge when using LiDAR data (Aronoff & Petrie, 2005, pp. 230-231; Liu, 2008; Mallet & Bretar, 2009). One example, directly related to this study, is that of Ola Fredin (NGU/NTNU) and Marie Keiding (NGU/GEUS). They have discovered that the area around Brumunddalen possibly has been subjected to PGS, as landslides emboss the surface, even though the terrain slope of the area is quite gentle (O. Fredin, personal communication., 2020). Landslides, suspected to be a result of PGS, have been discovered in large parts of central and northern Sweden, northern Finland and is suspected in Oslo, Ulvik, Haram, Flatanger, Rana and Beiarn in Norway (see Figure 2) (Olesen et al., 2003; Lagerbäck & Sundh, 2008; Olesen et al., 2013; Smith et al., 2014; Palmu et al., 2015). These areas were covered by the Fennoscandian ice sheet and are part of the same continental plate (Holger & Wu, 2011). When areas on the same continental plate, in close proximity to one another, have experienced landsliding due to PGS, it is fair to assume that other, nearby areas have experienced it as well.

Mangerud et al. (2018) have mapped and dated a likely PGS triggered landslide scar in Hemma, Ringsaker, an area close to the study area. Although possible, the landslide presented in their analysis is much less visible than those mapped in this thesis. Therefore, findings from Brumunddalen might be evidence of the landslide scar in Mangerud et al. (2018) being induced by PGS, whilst data from their research might be of interest in regards to the findings in this thesis, considering the proximity of the two sites.

Chapter 2.1 Bedrock

The area is dominated by the Oslo Rift formation, which formed during the last phase of the Variscian orogeny by which the Pangaea supercontinent was created in late Karbon and Perm. The rifting resulted in a NS-trending graben structure with extensive intrusive activity and volcanism. Today, the Oslo Rift extends from the Oslofjord in the south to the southern Oppland and Hedmark in the north. It is bounded by large normal faults on both sides (Ramberg et al., 2013).

The bedrock in the studied area is dominated by sandstone of the Hedmark group (Nystuen, 1982), as seen in Figure 3. The remaining three dominating rock types, clearly present, is Hedmark group limestone, tillite and Paleoproterozoic gneiss-granite (www.ngu.no).

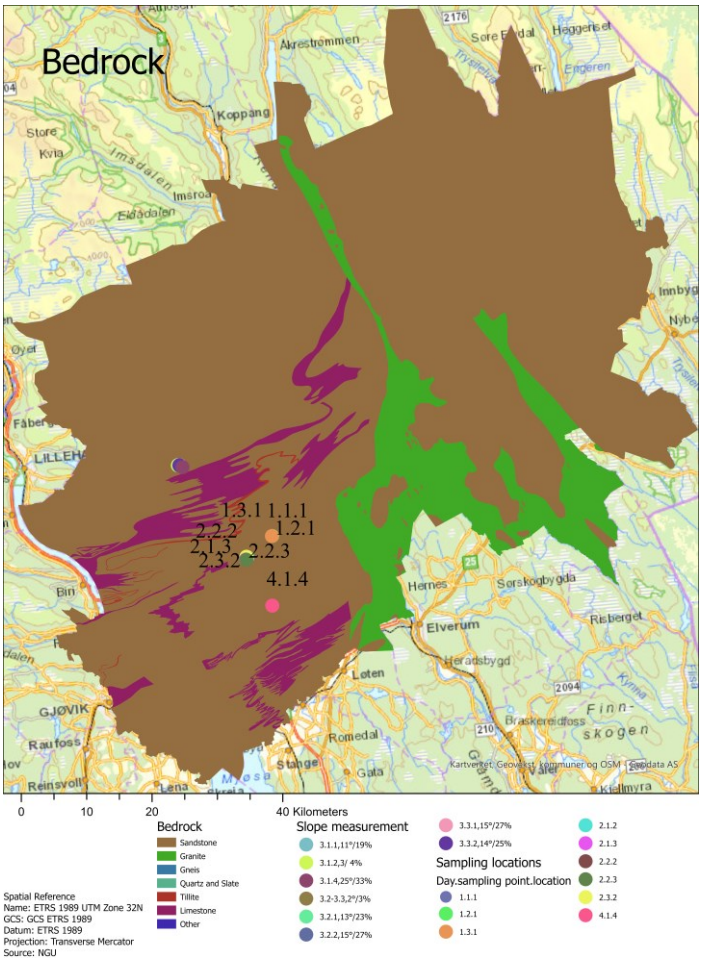

Figure 3 Bedrock map illustrating the main rock types dominating the different areas surrounding Brumunddalen. The data is collected and supplied by NGU, but modified to use in this thesis. Different types of sandstone, limestone, gneiss were merged together into separate classes. Some rock types were placed into the category "other" to clarify the cartographic design (Data from NGU) .

Chapter 2.2 Surficial Deposits

The area's soil primarily consists of till material (Figure 4) – deposited by one or several of the ice sheets that have covered Scandinavia during Quaternary time. Other prominent Surficial deposits components are peat, glacifluvial deposition and melt-out till. As seen during the fieldwork (see Chapter 4.2 and Chapter 5.1) and in the grain size analysis (see Chapter 4.3 and Chapter 5.3), did the soil consist of large parts of sand and silt.

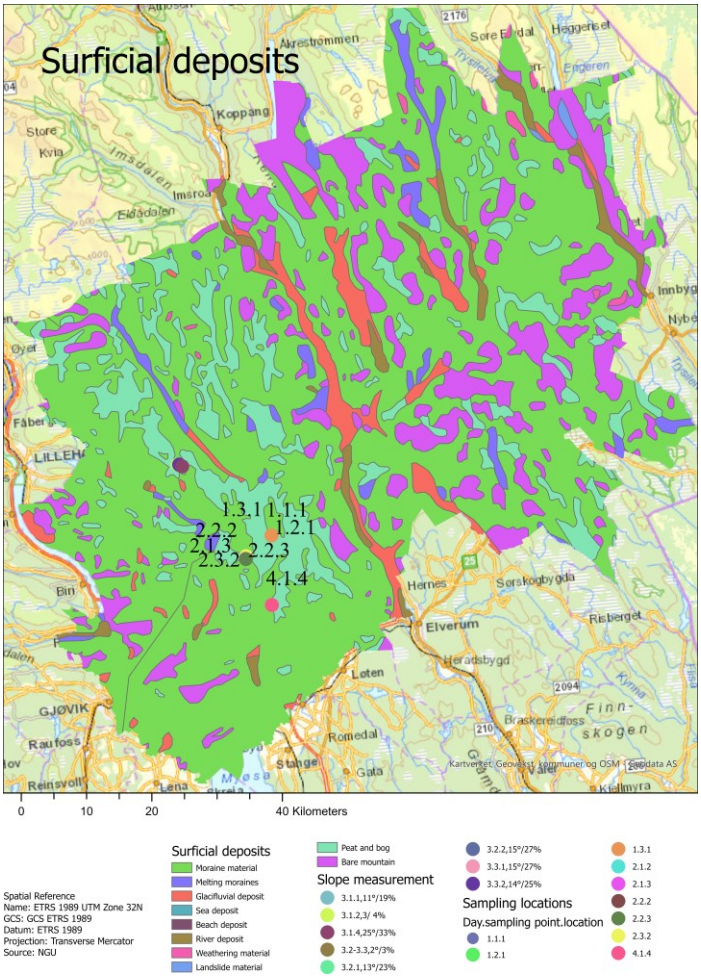

Figure 4 Surficial deposits map. Data collected and distributed by NGU.

Glacial till, which dominates the area, is generally of local origin. This happens through glacial erosion where the ice sheet erodes (plucking and abrasion) of the underlying bedrock incorporating bedrock clasts, sand and silt into the till (Follestad et al., 2013). As the bedrock is mainly sandstone, it is natural that the soil, which is mostly till material deposited by the ice sheet, consists of large amounts of sand and silt (Follestad et al., 2013).

Chapter 3 Theory

Chapter 3.1 GIS

GIS is used in many different disciplines; common for most of them is that spatial data is used to describe the Earth or at least part of the Earth. Burrough and Rød describe GIS as a collection of tools to collect, save, manipulate, analyse, present and distribute spatial or geospatial data (Burrough, 1986, p. 6; Rød, 2012, p. 17). However, Rød emphasises how this description may encode the meaning of GIS for people without the required technical knowledge and proposes an alternate description, inspired by Green: "GIS as a set of tools used to convert geographic data to geographic information and increase knowledge and/or solve geographical problems" (Rød, 2012, p. 17. *My translation*). GIS is, in short, a collective term used to describe computer programs designed to manipulate spatial or geospatial data to gain information and knowledge. There are many different providers of GIS software. In this thesis, the Environmental System Research Institutes (ESRI®) product ArcGIS Pro® has been the main software, but Esri Survey123® and Esri Arcmap® have also been used where necessary or convenient.

Chapter 3.1.1 Raster and Vector

The GIS software distinguishes between two main types of data – vector and raster. A useful explanation of the two data types is that they are different data models to represent the real world. The two formats bring forth different advantages and disadvantages, making them suitable for different use.

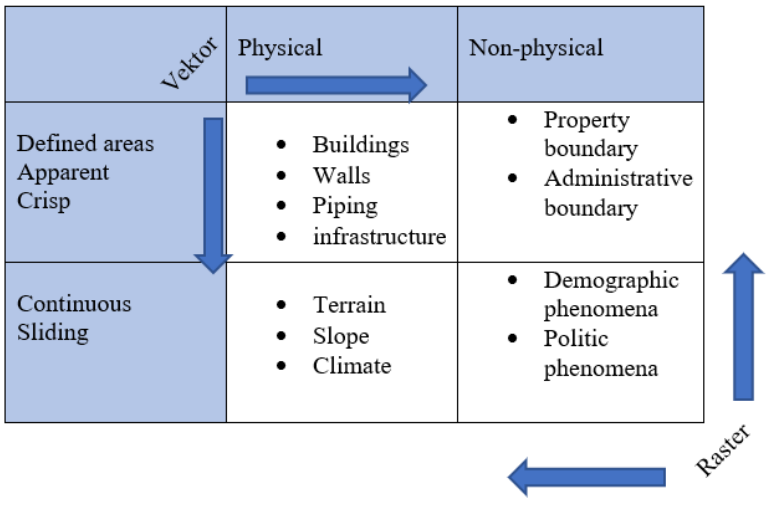

Figure 5 Schematic illustration of Vector and Raster.

Raster data represents real-world objects through arrays of cells or pixels (see Figure 5). These cells are usually rectangles but can be represented by other geometric shapes as well. Each cell can hold several values in its attribute table, for instance, height, soil type or type of

building, but only one of the attributes can be represented in the map at a given time. Buildings, soil type and vegetation are usually mapped through infrared aerial photography (manual, semi-automatic, or automatic classification). Height can be retrieved through different methods such as aerial photo photogrammetry, satellite image photogrammetry, radar inferometry and LiDAR. Raster data is further divided into discrete raster and continuous raster, where the latter consist of decimal values while the former only whole numbers. A discrete raster is suitable for representing objects with definable boundaries, such as roads, lakes or buildings. On the other hand are continuous rasters best suited to represent continuous values such as elevation, incline or terrain, as each cell potentially can represent unique values (Rød, 2015, pp. 36-41; Longley et al., 2015, pp. 66-67). A raster is further described by it is resolution – the number and size of cells. The resolution, sometimes called ground sampling distance, determines how much detail is derived from remote sensing and describes how small objects on the ground can be distinguished. A high-resolution raster contains a lot of details but loads slowly, has a high processing time and requires a lot of storage space. A lower-resolution raster load faster, has a faster processing time and requires less space, but displays fewer details (Rød, 2015, pp. 36-41; Longley et al., 2015, pp. 66-67).

Vector data is best suited to represent definite and categorical values (see Figure 5). It consists of feature classes – points, polylines and polygons. When working with vectors, the representation of real-world objects is limited to generalisation, as the shape is not suited to represent varieties in the dataset. Vector data is a simplification of real-life objects such as trees, buildings, roads and lakes. The different feature classes can represent one or multiple categories, depending on the values in the attribute table. Feature classes are usually divided into thematic layers, where one layer only contains one feature class. These layers can represent the same object in the real world, but the imagery is different. The visualisation of feature classes is determined by the shape and the attribute used to symbolise it. One feature class representing buildings can distinguish between private homes, churches, hospitals, schools, depending on the attribute used to symbolise it. Therefore, vector data is ideal when visualising finite objects (Rød, 2015, pp. 23-33; Longley et al., 2015, pp. 68-69).

When interpreting and analysing the surface in ArcGIS Pro, it is beneficial to have a tool to mark the map's different findings. The *create feature class* is a way to represent objects, usually finite, from the real world. ArcGIS shapefiles are vectors and can create points, lines

or polygons, depending on what they represent. Points can represent cities, lines can represent roads and polygons counties.

Chapter 3.1.2 LiDAR

As with the difference between raster and vector, the different remote sensing technologies used to produce digital elevation models (DEM) have different qualities, and as a result, strengths and weaknesses. The three types of remote sensing technologies most used today are photogrammetric analysis of stereo aerial photography, radar interferometry (inSAR) and LiDAR (Aronoff & Petrie, 2005, p. 239; Liu, 2008). This thesis's spatial analysis and remote sensing processes are based on LiDAR data derived and maintained by statens kartverk, and made available through the geonorge web portal (www.geonorge.no). To acquire LiDAR data, the scanner combines three main technologies, a laser light, a global positioning system (GPS) and an inertial measuring unit (IMU) in an airborne platform such as an aeroplane. The IMU and GPS are most commonly found as part of the inertial navigation system (INS) in the aeroplane. The most crucial part of the collection process is the laser light, as it measures the distance from the sensors, in the aeroplane, to the ground surface. The GPS is used to determine the sensors' precise geographical location (X, Y, Z), while IMU is used to determine the sensor's rotation and tilt. In addition, a high-performance computer, high capacity storage to process and store the data collected and a highly accurate clock to determine the ellipsed time is needed. A GPS is also stationed on the ground to revise the posting's positioning and secure its accuracy (Aronoff & Petrie, 2005, pp. 229-230; Liu, 2008; Longley et al., 2015, pp. 180-181).

LiDAR scanning of the surface is carried out by emitting pulses of light from the sensor in a perpendicular line from the plane's flight direction and measuring the exact time it takes to reflect back off the surface to the sensor, as visualised in Figure 6. The speed of light is

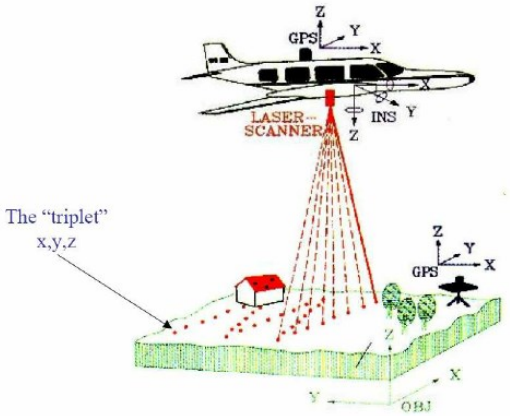

Figure 6 Illustration of how LiDAR points typically are collected. Two GPS stations, an INS and a laser scanner emitting light pulses perpendicular to the direction of the aircraft (From: Rombouts, 2006)

constant and known, making calculations precise. The slant range distance (elapsed time) and three-dimensional positions can be calculated by factoring in the light's angle when it hits the sensor, height from the GPS and orientation from the IMU. The precision of measurements is often between fifteen cm and four m for terrain mapping, as current systems emit around 2 million pulses/second. The postings, although emitted regularly, might create an irregular pattern, as not all of the pulses will generate detectable reflections. If an area does not have any postings, interpolating (see Chapter 3.1.4) of the data is required to create a regular digital surface model (DSM) and digital terrain model (DTM) grid (Aronoff & Petrie, 2005, p. 229-231; Liu, 2008).

LiDAR scans can not penetrate fog or clouds, which radar can, and needs a visible surface for laser pulses to reach the ground. As a result, LiDAR data needs to interpolate the irregular postings to create a DEM and therefore has the potential to be less detailed and geometrically precise than aerial photography and radar. However, LiDAR does create orthoimages (aerial photographs or satellite images that are geometrically corrected) from x, y, and z-values. Since the laser pulses creating LiDAR data do not penetrate vegetation, it gets multiple returns from each puls (Figure 7), generating detailed data used for DSM generation (Aronoff & Petrie, 2005, pp. 230-231; Liu, 2008; Mallet & Bretar, 2009; Su et al., 2016).

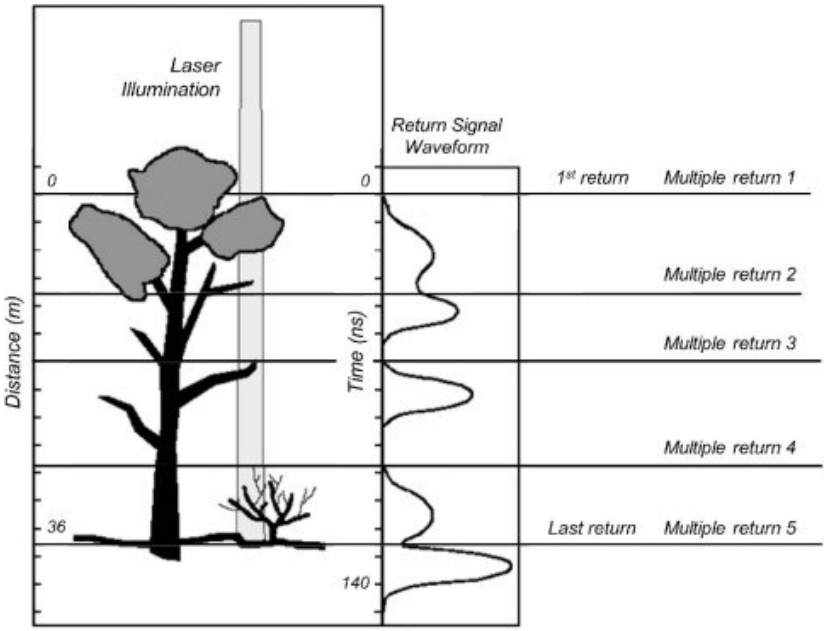

Figure 7 Multiple feedbacks from one imaginary laser puls when conducting a LiDAR scanning. Return 1- 3 is a branch from a tree, return 4 is a bush, and the last return is the ground. Return 1-4 does not return the entire laser puls, but some of it passes on to the next surface – giving multiple returns (From: Michez et al., 2016).

Earlier, point clouds (points collected from the lidar scanning) needed to be processed to remove objects on the surface, such as trees, buildings and cars (Aronoff & Petrie, 2005, pp. 230-231; Liu, 2008; Mallet & Bretar, 2009; Longley et al., 2015, pp. 180-181). It was a

crucial part of collecting LiDAR data used for DTM's. Today, the advances in LiDAR technology have made it possible to classify the returns based on the pulse waveform. GIS can classify returns as vegetation layers, water, buildings and ground, based on the laser pulses' waveform. The last return is usually the ground, as long as the whole puls is not reflected by vegetation or buildings. This simplifies the process of creating surface models (Figure 8) and is done by analysing the waves' form – seeing as different materials have different feedback and, in turn, looks different in the point return data (Mallet & Bretar, 2009; ASPRS, 2013; Su et al., 2016). Even when the postings are classified as vegetation or buildings before processing has started, objects on the surface can block the entire puls. To maintain the best possible resolution of the raster data, interpolating is required. There are several different methods to interpolate a raster dataset, but the goal is to create synthetic points to complete the data coverage and create a raster with regular spacing (ground sampling distance) (Aronoff & Petrie, 2005, pp. 230-231; Liu, 2008; Mallet & Bretar, 2009).

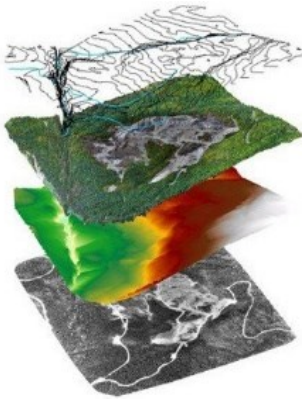

Figure 8 Data stack of layers created using a point cloud derived from a LiDAR scanning. The bottom to the top is an orthophoto, rectified/georeferenced using DEM, DTM colour coded with elevation data, DSM LiDAR-derived forest coverage and contour lines (From: MSDI, 2021)

Chapter 3.1.3 Digital Elevation Model (DEM) and Remote Sensing

DEM is a data model constructed by remote sensing points in regularly spaced intervals over the terrain and represents heights (Aronoff & Petrie, 2005, p. 214). Remote sensing is the collection and analysis of data derived from aerial photography, satellite imagery and radar remote sensing sources (Aronoff, 2005, pp. 1-2). The DEM points are characterised by geographic position in three dimensions – length, width, and height (X, Y, Z). The level of detail found in a DEM is determined by the postings; closer postings lead to greater detail in the

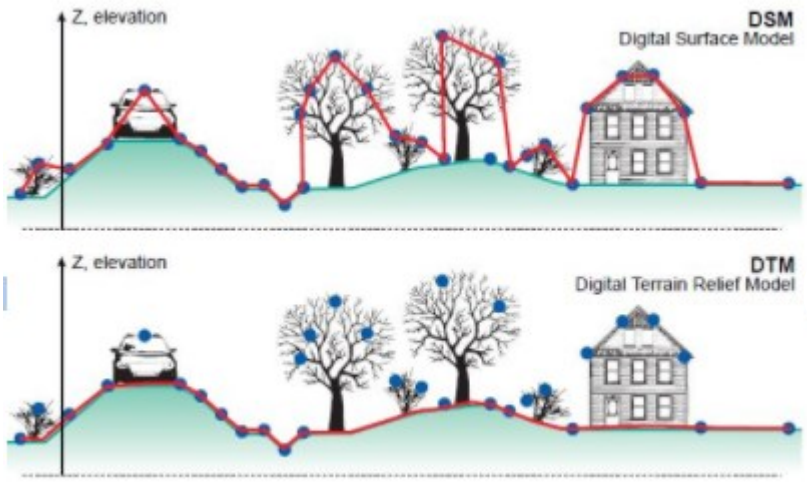

Figure 9 Points used from a LiDAR scanning to create a DSM and DTM. The blue dots represent the points, and the red line the continuous raster (From: CHARIM, 2021).

representation. A DEM can present two primary data models, DSM and DTM, as illustrated in Figure 9. DSM is usually derived from LiDAR-scannings (see Chapter 3.1.2) or aerial photography and contains everything found on the Earth's surface, including buildings and infrastructure. DTM represents the naked Earth, with no buildings, infrastructure or vegetation (Figure 9). Obtaining such models may require tedious processing in GIS – both interactive and passive, to ensure the quality of the DTM. The DTM's are used in topographic mapping, slope analysis, elevation and cross-sections, which in turn is used in remote sensing (Aronoff & Petrie, 2005, pp. 214-215). In his book, Jan Ketil Rød points out that a triangulated irregular network model (TIN-model) is best for visualising while the DEM models are best suited for analysis (Rød, 2015, p. 191).

Chapter 3.1.4 Interpolating

As briefly mentioned in Chapter 3.1.2, interpolation is a process where a GIS makes estimates of non-existing or non-terrain postings based on already measured postings. When creating DEM's, this is done by estimating or adjusting the height values of non-existing or non-terrain points (Liu, 2008; Longley et al., 2015, pp. 313-317). All methods for interpolation view proximity as one of the main factors in calculating new values. It is believed that areas with no sample points or false sample points have more similar values to nearby areas than distant areas – as Tobler's law suggests (Longley et al., 2015, pp. 313-317). Longley et al. (2015, p. 313) present three main interpolation methods; Thiessen polygons, Inverse-Distance Weighing (IDW) and Kringing. The dataset used in this thesis is, as briefly mentioned, a DTM derived from hoydedata.no. Kartverket has already processed and interpolated the raw data presented in a point cloud to create DTM's and DSM's, and in this study, interpolation has not been necessary to attain a DTM from the raw LiDAR data. Nevertheless, a short presentation of the three methods is in order to understand the process of interpolation.

Thiessen Polygons is a method initially developed to measure rainfall at locations where there were no measuring points. It draws a polygon surrounding a measuring gauge, and all points

within this polygon will read the same value (Figure 10). In the transition from one measuring gauge polygon to another, a distinct change will appear, as there is no calculation present to ensure a gradual change. It is most commonly used for rainfall and other areas where one can see a distinct separation (Longley et al., 2015, pp. 313-314; Rød, 2015, pp.194-195). GIS also use it in the internal process *nearest neighbour* (Longley et al., 2015, pp. 313-314) – a process where a GIS calculate distance "[…]between each feature centroid and its neighbour's centroid location. It then averages all these nearest neighbour distances" (Esri, 2020).

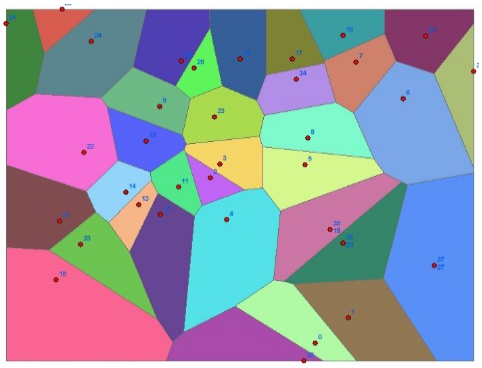

Figure 10 Thiessen Polygon – The polygon's point determines the values for all points within the polygon leading to a sharp/distinct transition between areas. (From: Geowizzard, 2021)

IDW is the most used spatial interpolation method in GIS analysis (Longley et al., 2015, pp. 313-317). It uses the known measurements to determine the most likely value for unknown points. Points closer to the location of interest has the highest impact on values assigned, while the impact of points further away drops by a factor of four. Most interpolation algorithms give the user the option of discounting points too far away or limiting the range of interpolated values, and so does IDW (Liu, 2008; Longley et al., 2015, pp. 313-317). If IDW interpolates a point that already has a value, the original value will be assigned and is therefore called the most exact interpolation method (Longley et al., 2015, pp. 313-317). As the interpolation is based upon a weighted average of surrounding points, the interpolated value can not be less than or exceed the maximum and minimum value of the original dataset (Liu, 2008; Longley et al., 2015, pp. 313-317; Rød, 2015, pp. 204-206). Consequently, IDW is not suited to interpolate terrain models such as DTM's or DSM's in areas where there is a substantial distance between points, as the interpolation can not provide values less than those that already exist. However, it is one of the interpolation methods least dependent on an involved user as the calculations are relatively simple (Liu, 2008; Longley et al., 2015, pp. 313-317).

Kriging is the last interpolation methods presented in this thesis. Kriging is, in contradistinction to IDW, highly dependent on input parameters as there are many different Kriging methods (Liu, 2008; Longley et al., 2015, pp. 315-317). Kriging is based upon the

idea that distance and direction between points can explain surface variations due to its spatial correlation (Liu, 2008). As with IDW, Kriging uses a weighted average, but instead of distance as its only input, the degree of variation between sampling points is also an essential factor (illustrated in Figure 11) (Liu, 2008; Longley et al., 2015, pp. 315-317). Multiple interpolation methods have raised the question about which is best, and there is no definitive answer. Kriging is the best alternative for a terrain model if the data points are sparse (Rød, 2015, p. 207), but as with most LiDAR point clouds, there are usually large amounts of points. In these circumstances, there is no real difference between IDW and Kriging (Liu, 2008).

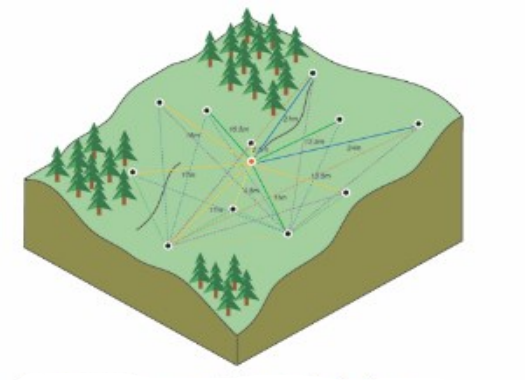

Figure 11 Kriging – Each of the adjacent points (Blue) are weighted according to proximity and degree of variation between the different points to create a value for the point missing value (red)(From: Esri, 2016)

There is little to no information provided by Kartverket about the processing of the LiDAR-data downloaded from their service. In an e-mail correspondence, Kartverket disclosed that the point cloud was collected with a varying degree of postings collected. The Interpolation process was rendered using triangulating with natural neighbour and bin with average value.

Chapter 3.1.5 Data processing and analysis in GIS

When remote sensing and mapping in GIS, processing the data using various techniques can be beneficial. When reworking DTM's and DSM's, several processes are available, including *Hillshading*, *Cut and fill*, and *Slope.* The different processing techniques can impact identification and analyses when mapping landforms (Chandler et al., 2018).

Chapter 3.1.5.1 Hillshading

Spatial data collected through LiDAR needs to be processed and altered to be suited for spatial analysis, as mentioned in Chapter 3.1.2. Significant surface features such as mountains and valleys can, to some degree, be distinguished, but the naked eye can not interpret most surface characteristics, as illustrated in Figure 12 (Chandler et al., 2018; Mangerud et al., 2018). Through *hillshading*, GIS software illuminates each individual cell in the raster with a hypothetical light (Esri, 2021g). Placement of the hypothetical sun is needed to create a *hillshade*. The sun can be adjusted with two parameters, azimuth and altitude. Azimuth determines the sun's angle, clockwise from 0° to 360 ° - north to south. Altitude determines the sun's illumination angle above the horizon from 0° to 90 ° (Chandler et al., 2018; Esri, 2021g). ArcGIS Pro's default setting for illumination of cells is altitude at 45° and azimuth at 315° NW (Chandler et al., 2018; Esri, 2021g), and it can be used when analysing hillshade produced for topographic purposes. However, to ensure the visibility of subtle features, sun elevation at 40° degrees is preferable, and azimuth depends on the trending orientation of landforms. Multiple hillshades with different altitude and azimuth values are preferable when conducting a spatial analysis looking for landforms. However, the azimuth bias is mainly an issue if the features in question are very subtle and linear, as the illumination might hide the landforms. Scars after landsliding are usually not subtle or straight lines. Therefore, azimuth bias is not a significant factor in most landslide analysis (Smith & Clark, 2005; Hughes et al., 2010; Mangerud et al., 2018; Chandler et al., 2018)

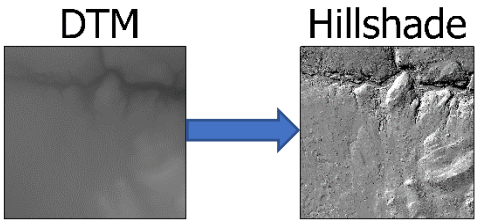

Figure 12 Illustration of DTM to Hillshade for visual analysis. Hillshade created with Azimuth 315° and Altitude 45°. The same extent and location used in both DTM and Hillshade.

Chapter 3.1.5.2 Cut and fill

In a *cut and fill*, the volume of two rasters is compared and the process's output estimates how much volume gain/loss the area has experienced (Verbovšek et al., 2017; Esri, 2021f). Esri (2021f) explains the process through a valley example. Suppose a valley is under surveillance to determine the sedimentary loss over ten years - researchers can then use the data collected from different years to determine how much mass is lost and gained in this period. The GIS process calculates the difference between two raster cells simultaneously, and the output is data containing positive or negative values. The negative values represent mass loss, while the positive values represent mass gain. Values of zero represent areas that have experienced mass equilibrium. In Figure 13, it is shown how this might look. In this thesis, a raster before the sliding incidents occurred does not exist. Therefore a synthetic raster was produced by assuming a continuous landscape surface to compare the surface before and after the landsliding occurred; see Chapter 4.1 for the methods used to create the synthetic raster.

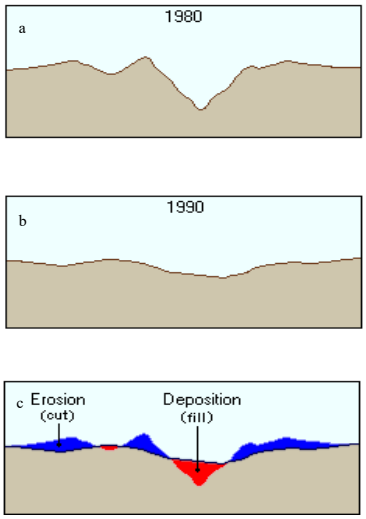

Figure 13 Illustration of how cut and fill works. a) is the cross section of the valley before, b) is a cross section of the valley after, and c) after the two profiles are run in cut fill in ArcGIS Pro. Red illustrates where mass gain has occurred, and blue where mass is lost. (From: Esri, 2021f)

Chapter 3.1.5.3 Slope map

As will be discussed in Chapter 3.3.4, most slopes are considered stable under "normal" conditions if the slope inclination is less than 25-30° (Norges vassdrags- og energidirektorat, 2011). The slope's steepness is not apparent when looking at a hillshade or DTM in ArcGIS Pro. However, the *slope* function helps visualise and calculate slope steepness in either percentage (%) or degrees (°) (Esri, 2021i). ArcGIS Pro calculates the gradient between neighbouring cells in a raster and produces a slope map raster (Esri, 2011; Longley et al., 2015, pp 324-326; Esri, 2021i). When calculating the point steepness in a grid, the points can be located on a sharp break such as a peak or a gully; in those instances, the calculation will not be a good representation of the steepness of the slopes. Therefore, most GIS applies fractal theory, a mathematical approach where the calculations are based on the point's relation to neighbouring points (Longley et al., 2015 pp. 324-326). The most common slope calculation, which is also used by ArcGIS Pro, is to calculate the degree of elevation change

in relation to eight surrounding points (Esri, 2011; Longley et al., 2015, pp 324-326; Esri, 2021i). *Slope* is usually made with an elevation model as the input, and the spatial resolution determines the accuracy of the product

Chapter 3.2 Sediment Sampling

Sediment sampling is the process in which researchers collect samples of sediments as a means to say something about the property of the soil or sediment. The so-called "grain size distribution" is an important measure of soil properties, describing the relative abundance of different grain size fractions (clay, silt, sand, gravel and sometimes cobbles/blocks). It can be used for many different sediments, but the procedures vary greatly, depending on the research questions. After defining the research question and means of sediment sampling, the question of *where* to sample arises. *Where* is a multifaceted question, which is dependent on the research question, but also considers what kind of sampling is planned. The sampling area is further dependent on the sediment composition (Evans & Benn, 2004, pp. 59 - 66). "Most deposits are […] heterogeneous both spatially and vertically" (Evans & Benn, 2004, p. 59), and the question of *where* to sample is, therefore, the most critical question (Evans & Benn, 2004, pp. 59 - 66).

Chapter 3.2.1 Size of sediment sample

The size of the sediment sample varies greatly, depending on what kind of sediments are sampled. It is suggested to collect larger samples when sampling in glacifluvial sediments or till than when sampling from, for instance, beach deposits. This is due to the glacifluvial sediments and tills heterogeneous nature, usually containing particles between 2-30 mm (Evans & Benn, 2004, pp. 59 - 66). Furthermore, it is suggested by Evans & Benn that multiple samples from such deposits are required to make up for sampling errors. However, this should be done for most sediment sampling, but the question of numbers of localities and sample size arise. When taking increasingly more samples, the number of replicas also increases, leading to a long process. Moreover, if the samples contain larger particles, the sample size increases further. This is especially true for samples with particles of >4mm (Evans & Benn, 2004, pp. 59 - 66).

When sampling in till Evans & Benn (2004, pp. 59 - 66) suggest a sample size in relation to the sample's biggest particle. If the sample contains no bigger particles than 1 mm, a 1 kg sample is enough, <2 mm a 2 kg sample is enough, while <10mm a 25 kg sample is enough when bulk sampling. However, Evans & Benn acknowledge that this sample size is unrealistic in most instances and suggests four approaches to make up for the lack of sample volume.

> (1) stratify samples with respect to the sedimentary facies present; (2) sample each facies independently and consistently; (3) sample only one facies, but sample this consistently at any different sites that are being compared; or (4) sample in a way that is random with respect to the facies. (Evans & Benn, 2004, p. 61)

The depth at which a sediment sample is to be collected is another multifaceted question. The depth determines what material is collected and what characteristics they have. NGU has a formalised procedure for collecting sediment samples. Samples of between 2-3 kg are collected at a depth of about 60 cm (O. Fredin, personal communication, 2021). This depth is chosen because it is within realistic reach of comfortable manual digging while avoiding most surficial biological- (digging animals, major roots) and agriculture (ploughing depth) disturbances of the original soil. It is also important to avoid sampling areas where there are indications of human activities such as digging and filling.

Chapter 3.2.2 Analysing sediment samples

When analysing sediment samples, a variety of different methods can be applied. The most common is dry sieving, wet sieving, settling column, laser diffraction and remote methods, to mention a few. The most important factor when choosing a method is to beware of the purpose of the analysis and the fact that comparing analysis using different methods can be challenging (Konert & Vandenberghe, 1997; Evans & Benn, 2004, pp. 66 - 69; Das, 2005, pp. 17 - 18). The method used to analyse the samples can impact the sediment sample size. The sample must be representative no matter the size, but only 50-250 g is required to analyse samples with materials between 0,063 mm – 4 mm when dry sieving (Evans & Benn, 2004, pp 59 - 61; Das, 2005, p 23).

The dry sieving process is quite simple and can determine the distribution of grain size in the sample. It is a method where the particle size is defined by the length of the sides of a square and is dependent on the calibration of the sieves, shape of the particle, mechanical stability and uniformity (Konert & Vandenberghe, 1997). The sieving analysis gives individual values for the weight retained on each sieve (grain size fraction), and when these are processed, the results from the sieving give information on the grain size distribution (Evans & Benn, 2004, pp. 12, 52 – 58; Das, 2005, pp 22 – 23).

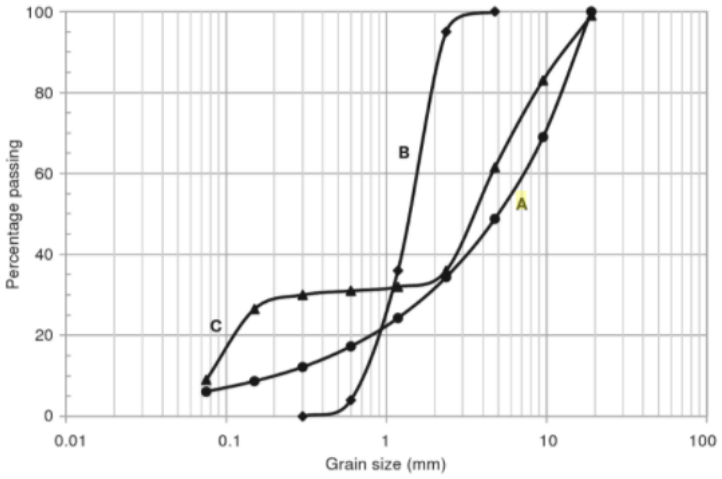

Figure 14 Examples of percentage passing plotted in a scatterplot where A) illustrates a well graded soil B) illustrates a uniformly graded soil distribution, C) illustrate a gap graded soil distribution (From: Sivakugan & Das, 2009)

The weight of each fraction, retained at each sieve, is often plotted as *percentage finer* over *grain size*. Figure 14 shows three different hypothetical sediment samples, where graph A) represents a soil with a more even distribution - well graded. A steep curve, such as curve b) represents a soil of few particle sizes – uniformly graded, while C) represent a soil lacking certain parts of the spectrum and is often referred to as gap-gated soils (Das, 2005, p 24; Sivakugan & Das, 2009).

The grading of soil and D^{50}-value of the soil (biggest particle size in the lowest 50% of the sample) significantly impacts the soil's susceptibility to soil liquefaction (see Chapter 3.3.3 on liquefaction) (Hakam, 2016; Chakrabortty et al., 2018). According to Chakrabortty et al. (2018), the average D^{50} value of liquefiable soils is 0.07 mm. It is further evident that particles with a

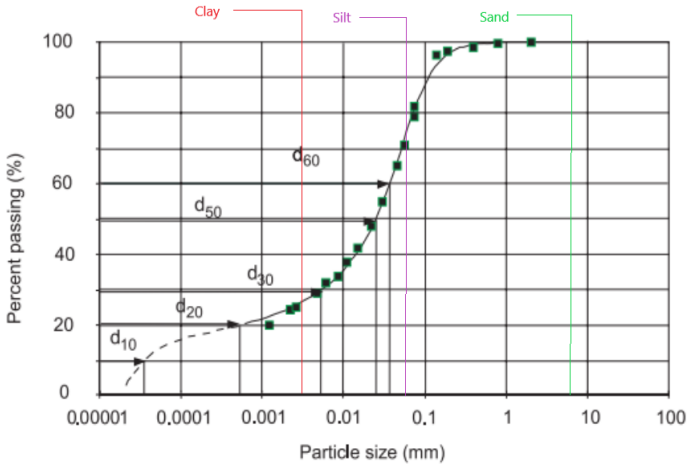

Figure 15 Illustration of a well-graded soil sample and how the size of different soil types can be distinguished from one another. Exemplifies the D10, D20, D30, D50 and D60 value for the soil sample (From: Fredlund et al., 2000). Clay, silt and sand approximations added to the figure.

size between 0.01 – 2 mm is within the liquefiable range (Chakrabortty et al., 2018). However, Hakam (2016) postulate a stricter boundary for D^{50} values of liquefiable soils with the interval of 0.1125 – 0.3375. A common observation for both of them is that with greater D^{50} values, soils are less likely to experience liquefaction (Figure 15 shows how D^{10}, D^{30}, D^{50}, and D^{60}). D^{60}, D^{30}, and D^{10} are values that are used to classify the soil sample, through calculating for instance coefficient of uniformity (C_u) and the coefficient of curvature (C_c) (Carrier, 2003). The $D_{10, 30}$, and $_{60}$ is based on the size of the 10%, 30%, and 60% passing the sieve (Carrier, 2003). Carrier (2003) suggests that "If Cu is >6 and 1<Cc<3, then it is classified as well graded. If Cu, <6 or Cc,1 or Cc.3, then it is classified as poorly graded" (Peck et al., 1974, P. 9; Carrier, 2003, P. 957; Das, 2005, p. 24)

Chapter 3.3 Literature Review of important Earth science concepts

Chapter 3.3.1 Glacial isostasy and rebound

The Earth is, simply speaking, divided into layers – crust, mantle (outer and inner) and core (outer and inner). The crust is two folded with the continental crust being the thickest but least dense and the oceanic crust being thinner and denser. Between the crust and the mantle, one can find the Mohorovičić discontinuity or, as it is more commonly referred to today, "the Moho", the boundary between the lithosphere and asthenosphere (Wolf, 1993; Krom, 2012, p. 30). The lithosphere consists of the crust and uppermost part of the mantle and rests on top of the asthenosphere or mantle (Krom, 2012, p. 30). Although the lithosphere is considered the mechanically robust outer shell of the Earth, it is essentially brittle; however, it is considered plastic in the isostatic process (Wolf, 1993). At this boundary, the Earth's surface is in a state of equilibrium – where all mass above this point weighs about the same (Sulebak, 2014, p. 15). As a first order approximation, this equilibrium determines where we have mountain ranges on the globe, with lighter continental crust and deep roots that provide

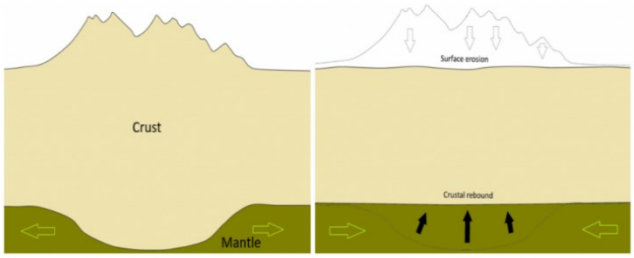

Figure 16 Illustration of the crust-mantle equilibrium and the effect of crustal loading/unloading on the mantle flow. When mass is added to the crust, the crust is pushed down to satisfy the equilibrium, and mantle flow (green arrows) is directed outward. When crustal unloading is happening, crustal rebound (black arrows) occurs, and slow mantle flow fill the void to satisfy the equilibrium (From: Earle & Vancouver Island university, 2019)

buoyancy for the mountains to protrude to several km high. A common analogy to explain this phenomenon is icebergs floating in water. High icebergs have a more significant body of ice than lower rising icebergs – due to the fact that they float in water, and the mass visual above the water is relative to the amount of ice submerged into the water. The same principle is found in the boundary between the lithosphere and the asthenosphere to satisfy the equilibrium. If a mountain is eroded, sediments from this will push on a low-rising surface. At this point, the mantle will be pushed down, resulting in an upwards stream of mantle at the eroded areas. Mass added to the eroded areas is heavier than that of the eroded material, and the mountain will only sink about ten per cent of the initially eroded mass. This process is identical to the process that happens during glaciation and deglaciation; the only differences are the mass affecting the equilibrium itself and the time scale (Wolf, 1993; Holden, 2012. p. 31; Sulebak, 2014. pp. 40-41).

Several ice models have been created, with varying results due to the varying data. However, during the Last Glacial Maximum (LGM), the ice's maximum thickness was around >3km over central Scandinavia (Holger & Wu, 2011). Stroeven et al. (2016) present a model, reaching back to around the LGM, divided into four regions – Western, central, eastern and southern. The western sector covered Norway, and in simple terms, the ice retreat can be described as slow and steady (Stroeven et al., 2016). As presented in the section above, is the sheer weight of an ice sheet of this size enough to offset the crustal equilibrium on the earth surface, as illustrated in Figure 16 and Figure 17. The surface area close to the ice sheet bulges up as the weight pushes the surface down, and the pressure on the lithosphere redistributes the mantle flow beneath it. In essence, it is the reverse process of eroding of mountains. When the ice sheet melt and pressure is lifted off, the Earth strives to attain equilibrium – a state of relaxation. This is attained by lowering the surrounding areas and lifting the ice-covered areas, again leading to a redistribution of the mantle (Holger & Wu, 2011).

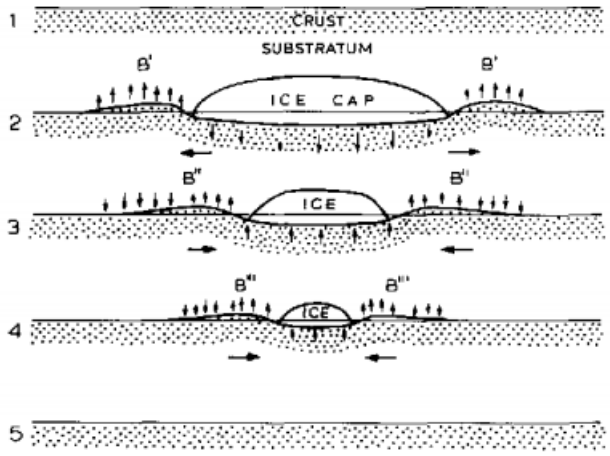

Figure 17 Illustration of ice sheets effect on the isostatic adjustment and crust-mantle equilibrium. Black arrows illustrate the direction in which the crust is forced (From: Wolf, 1993)

Since the LGM, about 22 000 years ago, the ice has steadily melted (Holger & Wu, 2011; Stroeven et al., 2016), and the last ice remnants in Scandinavia and North America disappeared about 10 and 6 ka ago, respectively (Dehls et al., 2000; Holger & Wu, 2011; Occhietti et al., 2011; Krom, 2012, p. 31; Stroeven et al., 2016). The vast volume of water locked up in ice at the LGM lowered the surface beneath it about 130 m and forced a marginally rise in the seafloor. During the LGM, about 5.5% of the worlds water mass was locked up in ice. In contrast, about 1.7% is locked up today (Holger & Wu, 2011). When the Fennoscandian ice sheet disappeared, most of this water was released back into the ocean, and the sea-level change, based on water mass alone, stabilised relatively quickly. Another process affecting the relative sea level is the gravitational pull. An ice sheet of the size of the Fennoscandian develops a gravitational field, and when it is close to the sea, it creates a gravitational pull on the water – resulting in a relatively higher sea level. Sea-level change due to both gravitational pull and the locked-up water perish relatively quickly (Holger & Wu, 2011; Mörner, 2015). The isostatic rebound process of the crust and mantle is a much slower process taking upwards of 10 000 years due to the mantle's high viscosity. (Holger & Wu, 2011; Simms et al., 2019)

Chapter 3.3.2 Post-glacial Earthquakes

There is some disagreement whether post-glacial uplift (PGU) is the main trigger for intraplate earthquakes or if tectonic movement is the dominating factor (Poutanen et al., 2009). Intraplate earthquakes are earthquakes that do not occur in close proximity to a tectonic plate boundary and are therefore especially hard to predict, leading to possible extensive damages to the surrounding areas (Talwani, 2014). Common areas for intraplate earthquakes include Eastern Canada, Northern Europe, Antarctica and Greenland (Holger & Wu, 2011) as well as India, China, USA and Switzerland (Talwani, 2014). Not only has the deglaciation and GIA (see Chapter 3.3.1) in Fennoscandia led to the area becoming important in the study of different phases of the glacial cycle (Holger & Wu, 2011). The Fennoscandia shield acts as a natural laboratory for GIA and the dynamic effects because it is a stable continental region fully representative of these factors (Bungum et al., 2010; Olesen et al., 2013).

In Norway, the most seismically active areas are believed to be Finnmark, Nordland, Møre og Romsdal, Hordaland and the area around Oslo (Figure 18) (Olesen et al., 2000; Olesen et al., 2003; Holger & Wu, 2011; Olesen et al., 2013; Keideng et al., 2018; Mangerud et al., 2018). However, It is debated how isostasy and seismicity are related. Today, the most probable cause for these earthquakes is considered to be mid-Atlantic ridge-push and/or GIA. However, the impact of uplift is considered trivial compared to that of ridge-push and the seismic activity in Fennoscandia by some researchers (Olesen et al., 2000; Olesen et al., 2003; Poutanen et al., 2009; Bungum et al., 2010; Holger & Wu, 2011; Olesen et al., 2013; Keideng et al., 2018; Mangerud et al., 2018). Multiple research papers count the remaining part of GIA as a viable explanation for the shallow and normal-faulting swarms, even today (Olesen et al., 2000; Olesen et al., 2003; Poutanen et al., 2009; Bungum et al., 2010; Holger & Wu, 2011; Olesen et al., 2013; Keideng et al., 2018; Mangerud et al., 2018). However, it does not rule out the possible effect of sedimentary loading and fluid intrusion (Gregersen, 2006; Bungum et al., 2010).

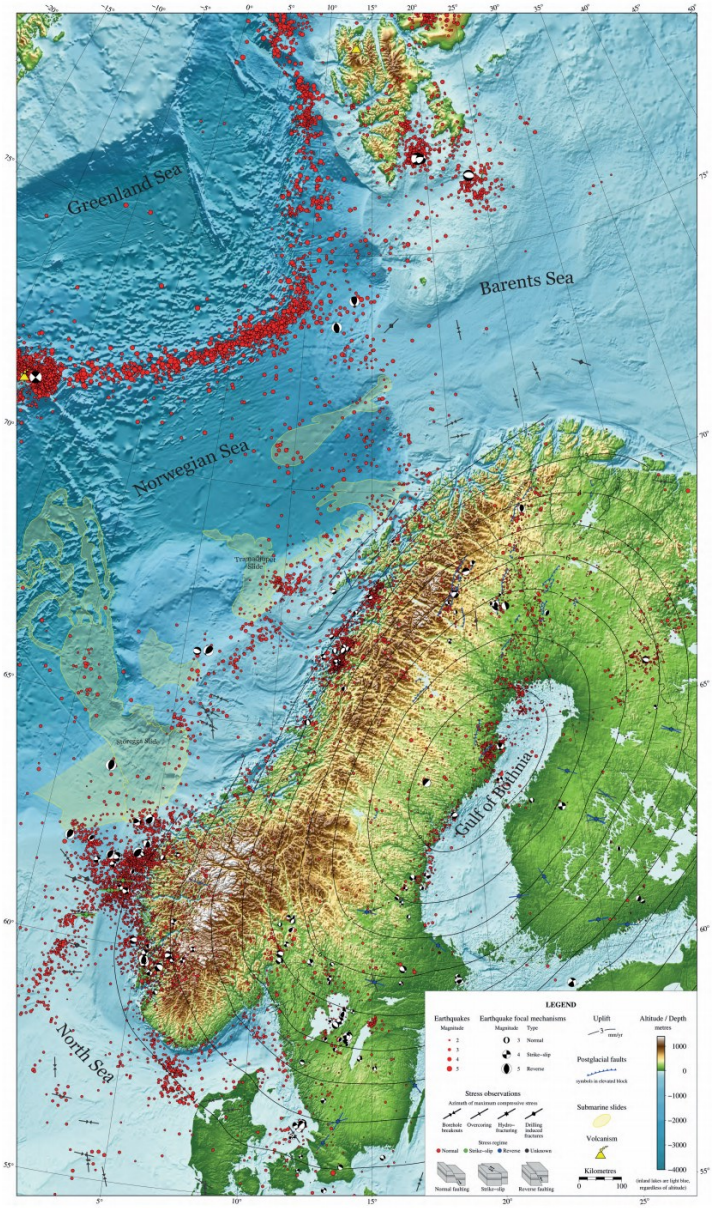

Figure 18 Seismic activity (Measured 1980-2012) in Fennoscandia (From: Keiding et al., 2018)

One explanation for the uncertainty of the origin of seismicity in Fennoscandia is the theory that the stress from GIA is reactivating tectonic faults and weakness zones (Poutanen et al., 2009). There is always evidence to support claims on both sides, seeing that multiple contradictory models have been made – with different variables from the same area

(Gregersen, 2006; Poutanen et al., 2009; Bungum et al., 2010). Since the 1880s, when the systematic studies of earthquakes and their geological settings to determine the seismic origin of landforms started, much attention has been given to Fennoscandian seismicity (Bungum et al., 2010). It has been concluded that Norway has intraplate seismicity at a low to intermediate rate (Figure 18). The concluding remarks of Bungum et al. (2010) is that plate tectonics and lithospheric structures are the dominating factors of intraplate earthquakes, faulting and landslides. However, they argue that GIA still contributes to the stress in Norway, especially for the northern parts. Furthermore, it is impossible to specify to which degree GIA and tectonic stress impact the intraplate earthquakes more precisely (Poutanen et al., 2009; Bungum et al., 2010).

Poutanen et al. (2009) also suggest that the observed seismicity in Fennoscandia results from various mechanisms building stress in the tectonic plates. However, studies of the origin of seismic activity in Fennoscandia are relatively rare, as the area has had few permanent seismic stations. Poutanen et al. (2009) state that "[t]he existing studies suggest that the sources are in areas of weakness in the crust which are favourably orientated with respect to the regional stress field and therefore can be reactivated" (Poutanen et al., 2009, p. 356). The general trend of NW-SE direction of the horizontal stress in the tectonic plates in Fennoscandia in general and, more specifically in Norway, suggest that the primary mechanism of stress build-up is ridge-push, rather than GIA, all though deviations from this pattern do occur (Poutanen et al., 2009). Although these findings suggest ridge push as the primary mechanism behind stress build-up in Fennoscandia, Poutanen et al. agree with Bungum et al. (2010) that it is challenging to determine GIAs impact because of the regional stress fields complexity and heterogeneity (Poutanen et al., 2009).

The process behind intraplate earthquakes is, as mentioned, suggested to be largely due to the ridge-push at the plate boundary, but GIA is also perceived to be a contributing factor. As the GIA builds stress in the lithospheric plates, inactive faults and weakness zones can be reactivated (Poutanen et al., 2009). When stress is high enough, the strength of lithospheric plates can no longer withstand it, and faulting can occur. The abrupt crustal movement releases stress from the plates as P-waves, S-waves, and L-waves propagate from the earthquake. This disruption may cause liquefaction of the soils, landslide and tsunamis (Mulargia et al., 2004).

As presented above, GIA can thus induce earthquakes, that in turn can trigger landslides. A way to determine if the area studied is affected by seismicity is to look at the landforms, processes and topography. If landslides have occurred in an area that is not prone to soil instability, such as quick clay dominated soil, or have an incline of less than 25^{o}, earthquakes are the most probable cause of sliding or faulting (Varnes, 1978; Olesen et al., 2000; Olesen et al., 2003; Lee & Jones, 2004, p. 47; Poutanen et al., 2009; Bungum et al., 2010; Holger & Wu, 2011; Norges vassdrags- og energidirektorat, 2011; Olesen et al., 2013; Keideng et al., 2018; Mangerud et al., 2018). Another way of determining the effect of PGS is through modelling of the area (Wu & Johnston, 2000; Poutanen et al., 2009). This can determine the likelihood that PGS has reactivated an old tectonically induced fault or weakness zone. The modelling approach is described in Wu & Johnston (2000) and will not be further investigated as faults have not been researched in this thesis.

Chapter 3.3.3 Liquefaction

Due to the shaking, or more precisely the seismic waves (S-, P- and L-waves), from earthquakes, soil can change its form from stable to "liquid" and unstable. This process is called liquefaction. All soil consists of small spaces and pores due to the irregular shape of the soil clasts and grains. Sand- and clay-rich soils have smaller pores than gravel and boulder rich soils. These pores are often filled with water so that groundwater constitute a large portion of the soil volume. In "normal" conditions, the soil remains stable as excess water is transported down the soil as percolation or out of the soil as runoff when the pores are filled. During an earthquake, the soils steady state can be overthrown by the shaking of the Earth. If the stress applied to the surface is greater than the soils steady-state undrained state, collapse and mass movement can occur (NRC, 1985, p. 4; Obermeier, 1996). During this process, the sand is shaken and compresses, pressing the pore-water up towards the surface. Compressed sand becomes more stable, while sand closer to the surface becomes oversaturated with water. The over-saturated soil becomes fluid, and objects resting on the surface will sink into the soil, or the shear strength of the soils drops. When shaking stops, water runs off, and the soil becomes stable again, locking grains and clasts to each other through friction. If the liquefaction process occurs in a slope, even a gentle slope, the liquified sand flows down, resulting in landslides as illustrated in Figure 19 (NRC, 1985, p. 1; Obermeier, 1996).

Liquefaction happens more readily in soil that does not have cohesive fines. This as a result of the lack of structure in the soil. Liquefaction is therefore dependent on the characteristics of sand – the gradation, particle size and shape, relative density, confining pressure and initial stress state (Obermeier, 1996; Mitchell, & Soga, 2005, p. 223). Loose sand with bigger pores is less stable and more prone to be affected by shear stress than denser sands. Therefore, the soil composition is an essential factor in determining whether the slope can experience liquefaction or not (NRC, 1985, p. 2; Obermeier, 1996; Lee & Jones, 2004, p. 47). Sandy soils and geological deposits, with silts, sands, and gravels, have shown to be most susceptible to liquefaction as a result of the particles' form. The soils plasticity is partially defined by the amount of clay and other fine sediments present, and the likeliness of liquefaction decreases with higher amounts of clay (NRC, 1985, p. 2). Also, pore pressure rise is less rapid in very densely packed sediments, and in turn, it loses less strength. Therefore densely packed sediments, with large portions of fines (clay), are less susceptible to liquefaction (Obermeier, 1996).

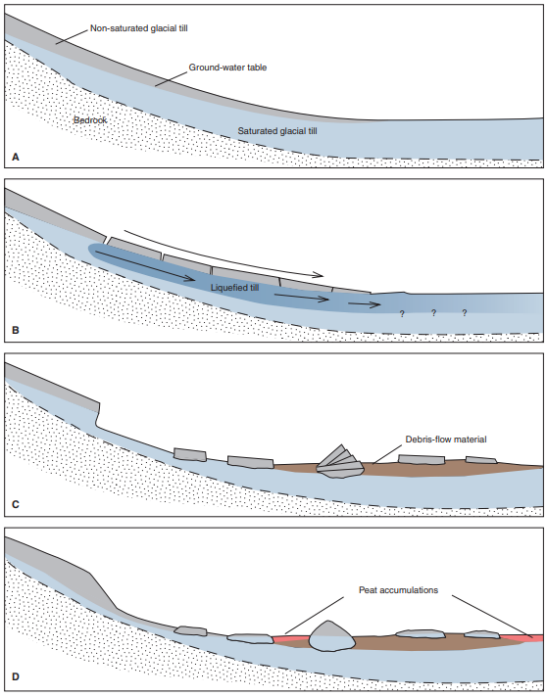

Figure 19 Flow failure diagram. When liquefaction occurs beneath the topmost layer of the surface, soil loses strength and flows down as a slope as a viscous mass. Soil stabilises when the pore water escapes and becomes stable once again. A) Prior to sliding. B) Earthquake shakes the ground and triggers liquefaction. C) Liquefied material relaxes. D) Present day situation (From: Lagerbäck & Sundt, 2008)

Although some soil compositions are more susceptible to liquefaction than others, it is evident that most granular soils with increased pore pressure can experience liquefaction during an earthquake when shaking intensity and duration is great enough (NRC, 1985, p. 4; Obermeier, 1996). Historical data of earthquake occurrences worldwide shows that liquefaction can occur at magnitudes (M) as low as 5 on the Richters scale, but it is not generally expected until the earthquakes reach M 5.5-6 (Obermeier, 1996). Soil especially susceptible to liquefaction can liquefy at M 5, but less susceptible soils do not until M 5.5-6 or higher (Obermeier, 1996). However, the notion that soil has been liquified due to seismic activity to create a landslide is tentative, as all sliding potentially can be induced by "normal" gravitational processes (Jibson, 2009)

Chapter 3.3.4 Landslides and "normal" slope processes

Landslides comprise most movement of earth materials such as rock, debris, sediments or soil due to gravitational pull. The latter is an essential aspect of defining a landslide, as it distinguishes the landslide from processes such as subsidence (Lee & Johnson, 2004; Ojala et al., 2019). Lee & Jones (2004) points out five main mechanisms that can be described as landslides – falling, toppling, spreading, flowing and sliding. Through a combination of topography, geological structure, hydrology climate and vegetation and the five mechanisms, landslides due to "normal" conditions can occur (Lee & Jones, 2004, pp. 41-44). Throughout this thesis, "normal" slope processes will refer to these pure gravitational mechanisms without a seismic trigger. The seismic trigger is considered an external factor, affecting the soils shear strength abruptly instead of building over time.

Falling, usually rockfall and soil falling freely through the air, and toppling, the forward rotation of mass out of a slope such as domino pieces, are less likely in gentle slopes (Varnes, 1958; Lee & Jones, 2004, pp. 41-44). Norges Vassdrags- og Energidirektorat (NVE) suggests that these landslide processes usually happen in slopes steeper than 40-45° (Norges vassdrags- og energidirektorat, 2011). Sliding is possible in gentle slopes but not very common. The sliding of soil is activated when the shear stress affecting the soil exceeds the shear strength. Shear strength decreases in steeper slopes, and less shear stress is needed to initiate sliding (Varnes, 1978). Sliding usually occurs in slopes of approximately 25°-30° inclination or more (Norges vassdrags- og energidirektorat, 2011; Bråthen et al., 2020). Flowing and spreading is the landslide motion most common in gently sloped terrain. It is usually induced by increased pore water or air pressure resulting in liquefaction of the soil (Chapter 3.3.3) (Varnes, 1958; Lee & Jones, 2004, pp. 41-44). However, understanding the landslide processes is not as simple as researching these few components, in addition to the inclination of the topography, it is influenced by hydrology, vegetation, climate, geological structures and lithology.

Although much information about the sliding incident can be retrieved by looking at a landslide, it must not deflect from the landslides' underlying processes. Lee and Jones (2004) present four stages of landslide movement: pre-failure movement, failure, post-failure movement, and reactivation (Lee & Jones, 2004, pp. 45-51). Pre-failure describes all processes leading up to the failure of the surface. Most soils behave as a viscous mass and creep as a result of shear stress. The creeping leads to increased shear stress further down or

out in the slope, eventually triggering the failure of the surface (Varnes, 1958; Lee & Jones, 2004, pp. 45-51). The failure occurs as a result of the constant creep in the mass. Non-brittle mass creeps and builds shear stress until it reaches magnitudes that surpass the soil shear strength. At that point, rapid and sudden sliding or falling occurs, relieving the shear stress by displacing large amounts of mass (Lee & Jones, 2004, pp. 45-51). In brittle soil types, such as clay, shear strength increases to a maximum capacity before lowering again. This results in mass expanding to relieve the strain of creeping mass. As a result, slow deep seated sliding usually occurs until the mass balance is restored (Lee & Jones, 2004, pp. 45-51).

Post-failure movement is the movement of mass from right after failing up until it stops. It displaces the residual kinetic energy after the initial failure. The essential mechanisms described as post-failure are mass liquefaction, sliding surface liquefaction, remoulded quick clay, impact collapse flow slides and sturzstrom (Lee & Jones, 2004, pp. 45-51). In this thesis, mass liquefaction and sliding surface liquefaction are the most interesting, and these processes will be the focal point of this paragraph. The liquefaction process is presented in Chapter 3.3.3, and the central concept is the same for all liquefied soils, although the triggers can vary. Mass liquefaction, for instance, "[…] occurs when the soil structure suddenly fails without exerting its frictional shear resistance, for example, as a result of rapid seismic loading" (Lee & Jones, 2004, p. 47) see Chapter 3.3.3 for a more in-depth explanation. Sliding surface liquefaction is also a common result of earthquakes. It follows when sandy soils develop shear surface and "[…] the grains are crushed or comminuted in the shear zone" (Lee & Jones, 2004, p. 48) until the volume reduction reach a level in which no further grain crushing occurs (Varnes, 1978; Lee & Jones, 2004, p. 48).

Chapter 4 Methods and materials

The following chapter presents the methods used to collect and analyse data in this thesis. Three main methods were used in four different steps, but each method consists of several individual tools or processes for the intended purpose. The four main steps used in the research are – 1. Spatial analysis in ArcGIS Pro, 2. Fieldwork in Brumunddalen to collect sediment samples, 3. Dry sieving analysis, and 4. further spatial analysis in ArcGIS Pro (Figure 20). The course of the methods was determined through communication with the supervisor and researching similar projects to determine the best possible course of action.

Figure 20 simplified overview of the overall workflow.

Chapter 4.1 Tools and processes in ArcGIS Pro – Before fieldwork

The processes and methods used in GIS are presented in Figure 21. The first course of action was finding and downloading data. As a DTM is necessary for terrain analysis, this data was downloaded for Innlandet, the county where Ringsaker and Brumundalen are located. Using an already processed DTM, instead of the raw point cloud from the LiDAR scanning, was based purely on convenience and access. Interpolating and processing the point cloud is a time-consuming and tedious process, and since Kartverket specialises in processing and distributing geospatial data, it was assessed that their interpolation was sufficient. Kartverket specifies that the DEM, DTM and DSM are distributed with a spatial resolution of 1x1 m and with coordinate system *WGS-1984-UTM-Zone-32N*. The base layers were used to map the Brumunddalen area for landslide scars, check slope angles to see if the terrain supports gravitational landslides or not, and calculate the volumes missing in landslide scars and test if it matches the landslide deposits, although some processing was conducted before this point. The DTM downloaded from kartverket is distributed as smaller "tiles", as seen to the left in Figure 22, to facilitate data transfer. The data covered a larger area than initially required, and the data was therefore clipped to the extent of a polygon surrounding the study area using the ArcGIS Pro tool *Clip raster* (Esri, 2021a; Esri, 2021b). The clipped DTM still consisted of smaller "tiles" and was therefore run through the ArcGIS

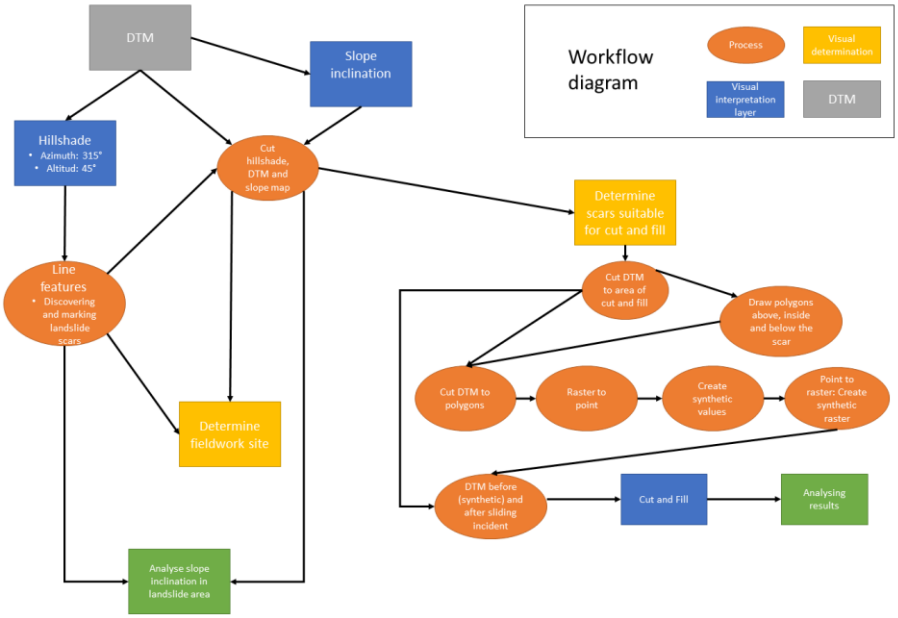

Figure 21 ArcGIS Pro workflow - most processes included.

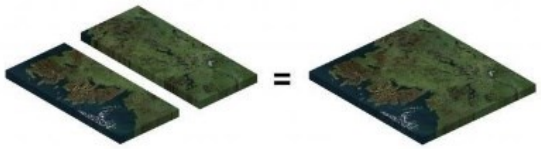

Figure 22 Mosaic raster data to new cohesive raster (From: Gisgeography, 2020)

Pro tool *mosaic to raster* (Figure 22), splicing two or more individual rasters to get one coherent and seamless DTM (Esri 2021h).

When the base map's initial processing was finished, the DTM was run through *Hillshade* in ArcGIS Pro to enhance the smaller surface features, such as landslide scaring (Figure 12). The default settings in azimuth and altitude were used, seeing as landslide scars are not prone to "hide" at certain illumination angles (O. Fredin, personal communication, 2021; Mangerud et al., 2018). Therefore, a hillshade was created with ArcGIS Pro default settings using the DTM downloaded from Kartverket with sun altitude set to 45° and azimuth to 315°.

After the hillshade was created, manual mapping of the study area was conducted. The mapping systematically looked at and interpreted the hillshade to determine if scars after landsliding were present (Lukas and Weibel 1995; Smith & Clark, 2005). As presented in Chapter 3.1.5.1, it is crucial to be aware of the possible biases created from hillshading when conducting the manual mapping of features. When aware of the possibility of biases, the likelihood of them being realised is reduced. The scars present themselves as lines in the terrain, and the most obvious vector representation is therefore ArcGIS Pro shapefile line features. The GIS operator creates the feature class directly into the geodatabase (Esri, 2021c; Esri, 2021d). When creating it, the GIS operator defines the type of feature, name, fields in the attribute table, the geometry values (m/z-values), a coordinate system (usually the same as the base layers) and tolerance. Tolerance defines how close multiple features can be and still be perceived as individual features (Esri, 2021c; Esri, 2021d). When creating line features to represent landslide scars the m-values should be turned on as they allow linear referencing. However, z-values are not too important, as these lines are digitized in 2D and do not contain elevation information. They do not yield much valuable information in terms of data but were rather tools used to visualise and navigate the mapped area. The manual mapping of features is time-consuming and prone to human error as the user's assessments define it.

This project was, as mentioned, started by Ola Fredin (NGU/NTNU) and Marie Keiding (NGU/GEUS), and some mapping had already been conducted. This mapping was provided by Ola Fredin and imported to ArcGIS Pro. The mapping of landslides performed in this thesis was then cross-validated with the mapping conducted by Fredin and Keiding. The vast majority of landslide scars were overlapping between the two mapping exercises. When features were not overlapping, they were merged to ensure that most, if not all, landslide

landforms in the area have been mapped. Before the initial mapping was considered finished and fieldwork sites could be determined, the final step was to produce a slope map. This ensured that the landslide scars sampled and measured were not at an incline that "normal" slope processes could induce a landslide (see Chapter 3.3.4). The DTM derived from Hoydedata.no was used to calculate the degree of rise through the process *slope* in ArcGIS Pro.

Chapter 4.2 Fieldwork

After the first round of analysis, it was time to conduct the fieldwork to measure slope inclination, collect sediment samples, observe, and take pictures. The fieldwork was conducted as part of a ten-day-long field trip, where the first five days were spent in Aurdal municipality in Innlandet, accompanying Vibeke Uthaug (Master degree student in Geography, NTNU) during her fieldwork on *signs of glacial movement*. Afterwards, we went to Brumunddalen to carry out the fieldwork relevant to this thesis. The methods used during the fieldwork were established together with supervisor Ola Fredin. The fieldwork was carried out according to NGUs general fieldwork methods. Therefore little technical literature was studied regarding fieldwork design, and all methods were conveyed in personal communication with Ola Fredin. The fieldwork was initially planned in May 2020 with Ola Fredin (NGU/NTNU) and Marie Keiding (NGU/GEUS), but as Covid-19 was roaming Norway, mixing cohorts was not ideal. Therefore, this thesis's fieldwork was postponed until the autumn and was performed by me, with the assistance of Vibeke Uthaug.

Chapter 4.2.1 Preparation

The first task was to locate the locations where the sediment sampling was going to take place. Eight different localities were chosen, some of which were supposed to be visited with Fredin and Keding the previous spring. Criteria for the locations chosen were that the landslides could not be located in a slope that could have experienced "normal" slope processes. In addition, the locations were chosen based upon sediment-, bedrock-, and terrain maps. It was also important that the deposition area did not show signs of fluvial processes as this could disrupt the sediment samples and give false values of sediment fractions, as the fluvial processes would have washed out the smallest sediments first. It was also important that the location was not dominated by thick peat, as it makes it hard to collect samples manually below the peat cover. That the locations were easy to access was also weighted, as

multiple samples needed to be collected in one day. When navigating and logging sampling points in the field, it is helpful to look at the mapping done in ArcGIS Pro. It is not ideal to bring a regular computer, as they can not withstand rough and damp conditions. Therefore, NGU provided a rugged fieldwork adapted laptop, Thoughpad, running Arcmap (an older Esri product). The data then had to be converted from ArcGIS Pro 2.7.1 to Arcmap as ArcGIS Pro data is not supported by Arcmap (Esri, 2021e). A survey123 (an Esri product for easy and intuitive data collection) was also created to collect the sampling point data. The survey123 collected data, such as date, location, direction, sampling-id, slope inclination, description of the area, description of the sample itself and pictures of the area, as a backup to the mapping on the thoughpad and in a notebook. To collect samples, the equipment needed were shovels and gardening spades to dig at the sampling point, a folding wooden ruler to ensure the same x-, y- and z-dimensions of the pit, clear plastic bags to store the sediment samples, and a tarpaulin to cover belongings when it rained and to collect the soil to be able to place it back into the pit easily. The equipment used to systemise the samples was masking tape and a permanent marker. Sturdy plastic boxes were used to transport and store the samples. The extra equipment used was a phone to conduct the Survey123, a camera to document the area and sampling procedure, a compass to navigate and determine the direction of the landslide scars, an inclinometer to determine the inclination of the slope, and a map to navigate the area.

Chapter 4.2.2 Fieldwork and sampling

As mentioned, the fieldwork was conducted according to NGUs standard procedure for sediment sampling, as conveyed by Ola Fredin. It was done by navigating the area around Brumunddalen and finding the predefined sampling localities. When the localities were reached, a visual assessment was done to determine if the site was suitable for sediment sampling. Due to the equipment available and surface cover, some localities were not suited for sampling as a thick layer of peat covered them (see Figure 23).

Figure 23 Picture from sampling point were not suitable for sampling or sieving analysis

As a result, sampling in some localities was conducted in both the unworked glacial till (host material) and the reworked landslide deposit (the host glacial till being reworked into a landslide deposit), whereas in other localities, samples were only collected from either host material or sediment deposition. Figure 30 shows the location in which sampling was conducted. At the first location, sampling was conducted at three points, including both host material and landslide deposits. At location 2, only the third sampling point was suited; hence only landslide deposit was sampled. At location 3, both host material and landslide deposit was sampled, while at the fourth locality, only host material was sampled (see Figure 30 and Figure 38 for sample locations).

When localities suitable for sampling were reached, a pit between 50 – 60 cm deep was dug. A folding wooden ruler was used to sketch out a rectangle in which the pit was dug. The same wooden ruler was used to ensure the depth of the sampling pit. According to NGUs standardised procedure, samples at between 50 cm and 60 depth, below most current biogenic processes, are suitable to say something about the grain size distribution (see Chapter 3.2). A sample of at least 2-3 kg was collected using shovels and gardening spades. As the sample was manually collected, it was essential to try not to collect a particular selection of material but to collect as neutral of a sample as possible, containing all parts of the soil at sample

Figure 24 Overview of the sampling procedure in field.Green circle: bigger rocks manually sorted out. Blue circle: intact surface cover to cover up after digging. Red circle: plastic bags to store samples and field notebook. Purple circle: Sampling hole. Orange circle: shovels to dig the hole. Pink circle: Gardening shovel to collect the sample. Yellow circle: tarpaulin to collect sediments.

depth. However, some manual sorting was done to eliminate the biggest rocks in the sampling materials (see Figure 24). The samples were collected in two separate clear plastic bags and marked with masking tape and permanent marker before they were placed into two sets of

two clear plastic bags to ensure no leakage occurred. The samples were marked with three numbers, where the first number represented the sampling day, the second number the sampling point and the third number the sampling location. The sampling location was the area in which the landslide scar was present. The sampling points were the definite point where the sampling was conducted – above, in, or below the landslide scar. Hence, one to three sampling points were located at one sampling location, and one to two sampling locations were visited each day.

During the collection process, pictures and notes were taken to capture all potentially important details from the sampling location, using a *Rite in the Rain* all-weather journal and the *survey123* mobile app. The sampling points were also recorded in Arcmap to be transferable to ArcGIS Pro. In addition, an inclinometer was used to record the steepness of the terrain above, in and below the landslide scar. A compass was used to determine the direction of the scar. When all notes, recordings and pictures were taken, the soil removed from the pit was placed back in the pit, and land coverage (grass, peat, etc.) was arranged on top to cover the traces in the best way possible.

Chapter 4.3 Grain size distribution

As mentioned in Chapter 3.2, Grain size distribution is a way to analyse the soil's properties. In this instance, it is used to retrieve information about the soil's likelihood to liquefy during an earthquake. The two most common ways to do a grain size analysis are the dry sieving and hydrometer method. Dry sieving is commonly used to analyse granular soil and sand and to distinguish particles greater than 75µ/65µ, and less than 100 mm. Particles greater than 100mm are usually distinguishable visually (Geoengineer, 2014; Department of transportation: New York, 2015). For fines, finer than 75µ/65µ, the hydrometer method is suggested (Geoengineer, 2014; Department of transportation: New York, 2015). The grain size distribution methodology was outlined in collaboration with Ola Fredin, in line with the literature.

Chapter 4.3.1 Procedure

When conducting dry sieving, the equipment needed is a drying oven, a set of standard sieves, sample splitter, mechanic sieve shaker, pans, scale (readable down to 5g), balance (accurate down to 0.01g), containers, wooden mallet and an assortment of brushes, although the

literature varies (Geoengineer, 2014; Department of transportation: New York, 2015). As the lab at NTNU Dragvoll was used to conduct the sieving, not all equipment needed was available. The equipment available was a drying oven, standard sieves, sieve shaker, mallet and brushes. The scales available was either not able to weigh samples of the size needed or not operative. Therefore, a kitchen scale (accurate down to 1 g) was brought from home. In addition, a tablespoon, pencil, paper and camera were used.

The procedure starts by separating the 2-4 kg samples into samples of around 500g (Geoengineer, 2014; Department of transportation: New York, 2015). The proper way to do this is to use a sample splitter, where the sample is divided into portions of the desired size. The laboratory at NTNU Dragvoll does not have a sample splitter, and the samples had to be manually separated. Therefore, extra caution was exercised when splitting to ensure neutral and representative samples (Sollid et al., 1973; Geoengineer, 2014; Department of transportation: New York, 2015). The samples were put into metal containers and placed in a drying oven at 110° ±5° C for 60 hours (Geoengineer, 2014; Department of transportation: New York, 2015). When samples were dry, they were transferred to airtight containers to stop moisture from building up. The samples were then weighed, and notes were recorded into a spreadsheet and on the outside of the container. The samples that were dried and ready were stored in a dark cupboard until the lab was available.

Figure 25 Stacked sieves, mallet, brush, weight, spoon, brush, spreadsheet and samples used in sieving analysis

The sieving procedure was carried out by retrieving the samples and one by one spooning the sample into a mallet where the soil was partially split by hand before tipping them on top of

the sieves (stacked from 16mm on top and progressively smaller down to 65µ, with a pan on the bottom) (Geoengineer, 2014; Department of transportation: New York, 2015). The sieve sizes were as follow (from biggest to smallest): 16mm, 8mm, 4mm, 2mm, 1mm, 500µ, 250µ,125µ and 65µ. A pan was placed at the bottom to collect everything finer than 65µ. The lid was then placed on top, the stack placed onto the shaker and secured into place by tightening the locking mechanism. The minimum time requirement for shaking varies in the literature, from 3 to 10 min in a mechanical shaker. In this instance, the sieves were shaken in two intervals of 10 min, with some manual interaction in between. Particles retained on each sieve were then weighed, recorded into a spreadsheet and placed back into the airtight container (see Figure 25, Figure 26, and Figure 27 for the equipment used). It was hard to retrieve the whole sample in some of the finer sieves. As much as possible was emptied before the sieves were cleaned and stacked, ready for the next sample.

Figure 26 Mechanic shaker used in the sieving analysis

The sieving results were then plotted into an excel document to calculate the cumulative percentage of grain size and plotting. The sediment sample's total weight is represented by *W,* and the portion of the sample retained on each sieve is represented by *SW*. Then different equations were calculated to determine the percentage not retained on the sieve (*Nx*), percentage retained on the sieve (*Px*), cumulative percentage retained on the sieve

Figure 27 Samples before (to the left) and after (to the right) sieving

(*Cx*) and percentage finer than the sieve (*Fx*). $Nx = \left(1 - \frac{SW}{W}\right) * 100$, $Px = \frac{SW}{W} * 100$, $Cx = Px + Px + Px$ (Px value of the sieve and every sieve above it) and $Fx = W - Cx$ (Cx of the sieve calculating). The Fx's or Cx's final values are then plotted into a scatter plot where the X-axis is the sieves opening size, and the Y-axis is the Fx or Cx values as illustrated in Figure 14 and Figure 15 (Geoengineer, 2014; Department of transportation: New York, 2015).

Chapter 4.4 Tools and Processes in ArcGIS Pro – after fieldwork

Chapter 4.4.1 Cut and fill

To estimate some representative volumes of the landslides in the Brumunddalen area, *cut and fill* calculations were made in some representative landslides (See Chapter 3.1.5.2). The process works best if two datasets from two different years are available. In this thesis, the DTM represents the terrain only after the landsliding had occurred, as described in Chapter 1. The landslides possibly happened several thousand years ago, and a DTM representing the terrain before the landslide does not exist. Therefore, a synthetic representation of the terrain (DTM) before the landslide was produced using several GIS processes.

First, the landslide scars that we were going to analyse were chosen. Second, a *polygon* was drawn around the area. Third, the DEM was *clipped* and converted into points using *raster to point*. The height values of the points were then altered by adding or subtracting using *calculate,* and the values were stored in a new attribute called "before". This was done for the raster data in the scar and below the scar. The raster data from above the scar was calculated into the new field with no alterations, as the alterations from the landslide probably have been negligible. The process *point to raster* was then used to create three separate raster datasets with the new elevation values. These three rasters were then stitched together using *mosaic to new raster* before the new synthetic raster, and the original raster was used in a *cut and fill* operation (Figure 13).

Chapter 5 Results

The results from the research conducted throughout the process will be presented in three main chapters. First, the field observations will be presented through maps and tables to give a general overview of the study area. The following section will present the results produced in GIS, including the visual interpretation of the hillshade, slope inclination map, height profiles of key landslide scars and cut fill from the same scars. The last section will present the grain size analysis presented through tables and graphs.

Table 1 Lists the inclination of the area around where sediment samples were collected and the area around landslide scars where only inclination was measured. The inclination values are presented in °. Some additional information on the quality of the sample is also provided.

	Location 1		
Sampling-ID (Day.point.location)	1.1.1	1.2.1	1.3.1
Slope incline	*25°*	*15°*	*3°*
Description of the sample	Suitable for sampling and analysis - *Host material*	Suitable for sampling and analysis - *Host and depositional material*	Suitable for sampling and analysis - *Deposition material*
	Location 2		
Sampling-ID (Day.point.location)	2.1.2	2.2.2	2.3.2
Slope incline	*3°*	*3°*	*4°*
Description of the sample	Not suitable for sampling - *Host material*	Suitable for sampling. Not sutable for analysis - *Host and deposition material*	Suitable for sampling and analysis - *Deposition material*
	Location 3		**Location 4**
Sampling-ID (Day.point.location)	2.1.3	2.2.3	4.1.4
Slope incline	*9°*	-	*9°*
Description of the sample	Suitable for sampling and analysis. - *Deposition material*	Suitable for sampling and analysis. - *Host material*	Suitable for sampling and analysis. - *Host material*
	Day 3 Only inclination was measured		
Sampling-ID (Day.point.location)	3.1.1	3.1.2	3.1.3
Slope inclination	*11°*	*3°*	*25°*
Sampling-ID (Day.point.location)	3.1.4	3.2.1	3.2.2
Slope inclination	*2°*	*13°*	*15°*
Sampling-ID (Day.point.location)	3.3.1	3.3.2	3.3.1
Slope inclination	*15°*	*14°*	*15°*

Chapter 5.1 Fieldwork observations

The most general, and most prone to be affected by bias, is the field observations, as observation errors usually follow human observations (Sollid et al., 1973). As mentioned in Chapter 4.2, the field observations were done by recording % and ° rising in the area using an inclinometer for all sampling points. In addition, inclination values were collected for slopes surrounding the area and in a separate area northwest of the sampling locations (see Table 1). The general slope around the sampling points was around 9°. The general slope inclination in the area where only slope inclination was measured was 12°. All the planned sampling points are marked in Figure 30.

Figure 28 Picture from fieldwork. Illustrates the inclination in the area as well as the overall vegetation

Even though, as shown in Figure 28, human modifications were made to the area, such as forestry, visible distinctions between the surface in the landslide scars and the plateau above were observed but hard to document due to the area's dense forest. However, the general trend was trees appearing younger in the scar than in the area in general. There were also fewer trees in general in the scars than in the rest of the area. The surface coverage of the scarred area also differed to some degree. From the pits dug (Figure 29)t was evident that the plateau above and below the scar had a thicker layer of peat, vegetation, and moss. In the landslide scar, the ground consisted of thinner surface coverage of peat, moss, and till, and the soil appeared denser than the area in general.

Figure 29 Pit dug for sediment sampling

Two basic tests were conducted during the fieldwork to see if the soils fines mainly consisted of clay or silt. The test was carried out simultaneously with sampling. The first test was to take a piece of soil and roll it into a “snake”. Then the “snake” was connected to make a circle. If the soil were mainly silt, cracks

would form when the snake was bent to create a circle, while if the soil were mainly clay, the circle would not crack. The circle cracked at all locations, indicating sandy or silty soil. Furthermore, a piece of soil was placed into the mouth and chewed. If the soil crunches between the teeth, it is fair to assume that the soil consists of mostly micerogenic sand/silt and not dominated by organic debris (Wold & Sandven, 2016).

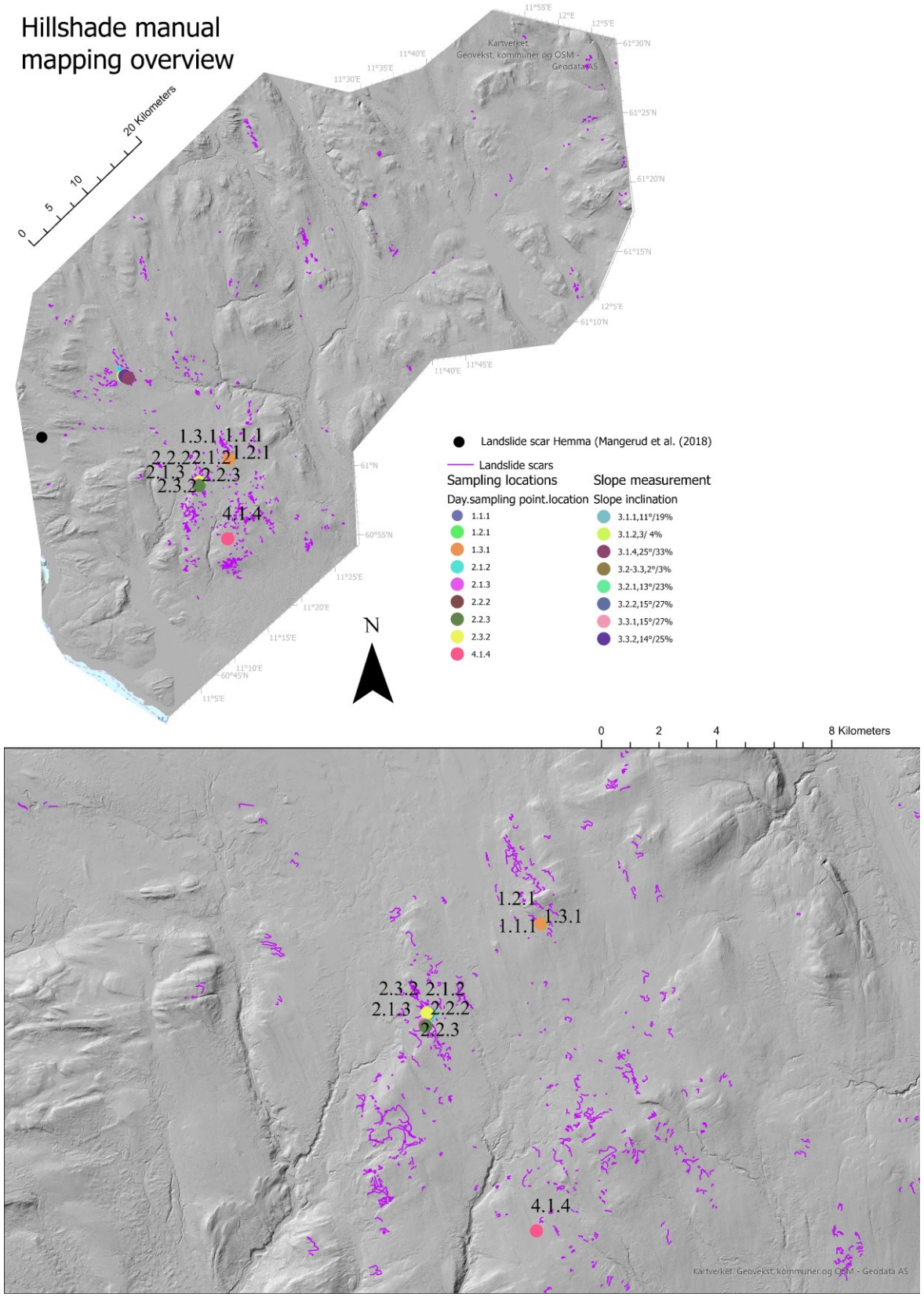

Figure 30 Hillshade landslide mapping and sampling points

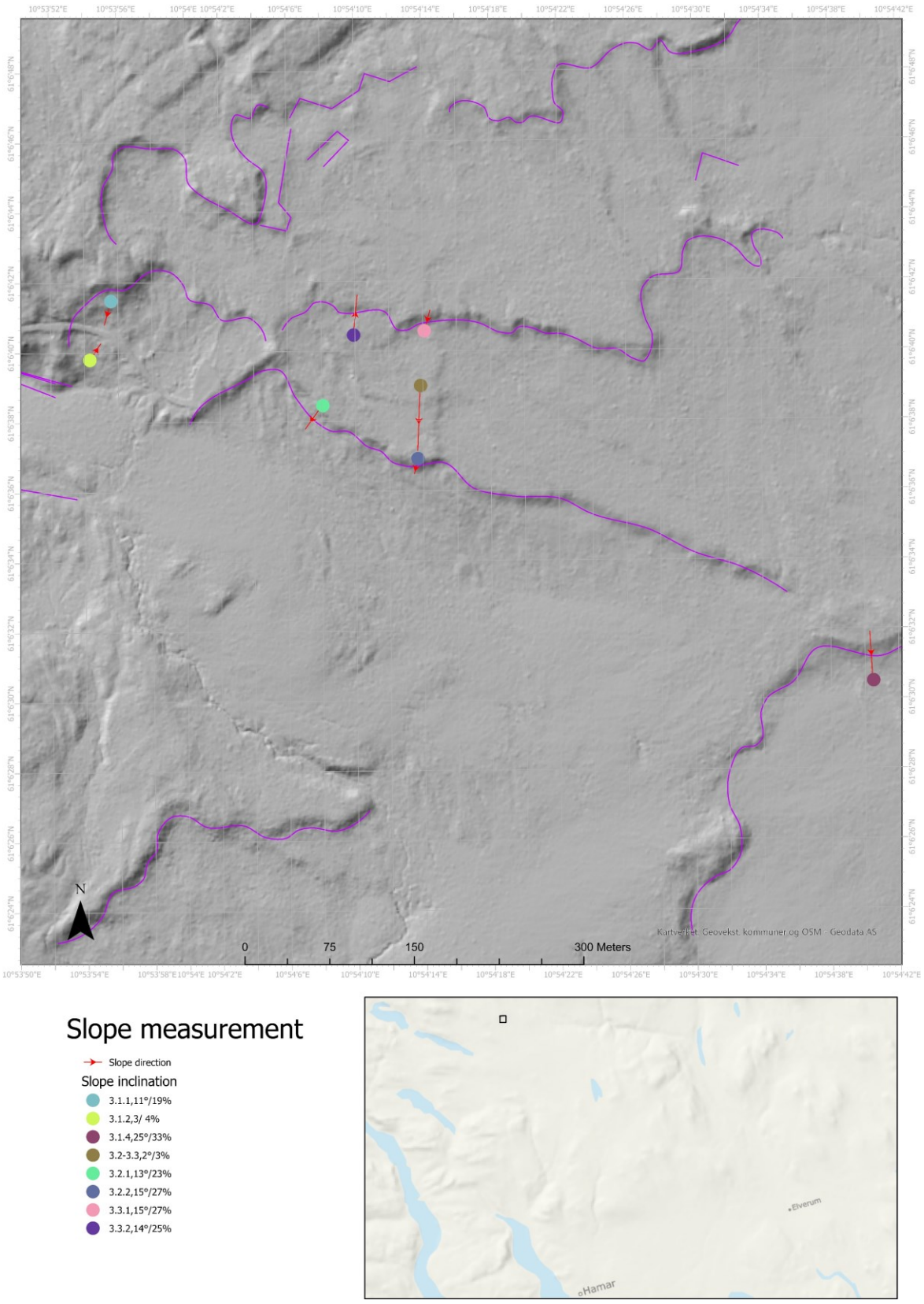

Figure 31 Map showing the area where only slope measurement was conducted and not sediment sampling

Chapter 5.2 GIS analysis

Chapter 5.2.1 Hillshade and manual mapping

The GIS analysis is, as mentioned, based upon *hillshading*, *line features*, *slope* and *cut fill*. The results from the processes conducted will be presented below in the form of maps, tables and pictures. The first results retrieved from the GIS analysis are a visual interpretation of the surface characteristics using the hillshade. It unveiled that the surface has been affected by landsliding as an abundance of landslide scars have been mapped. Many prominent scars have been mapped in the soil (till), but none has been found in bedrock. As seen in Figure 30, the purple line features enclosing the surface represent the visible landslide scars. There could be more landslides in the area that is not visible due to human interaction or other processes such as eroding or deposition. There could also be more landslides that have not been discovered during the mapping process or hidden by the illumination choices. Moreover, some of the mapped landslides could be something other than a landslide. However, since the mapping in this thesis has been cross validated with mapping done by Fredin and Keiding with very similar results, the dataset is judged as robust and representative.

The area has some steeper slopes, although most of the surface has a gentle inclination, well below 25°. In areas with steeper slopes, it seems like fluvial processes have cut into the sediments and bedrock, for example, along the major river valleys (Figure 30, Figure 31, Figure 32 and Figure 33). There are mapped landslide scars in the steepest areas, but they are probably due to the steeper riversides. Although seismicity could be a triggering factor, these landslides are not included in the mapping because “normal” slope processes could have occurred, making it difficult to determine the likelihood of seismicity.

Chapter 5.2.2 Slope inclination

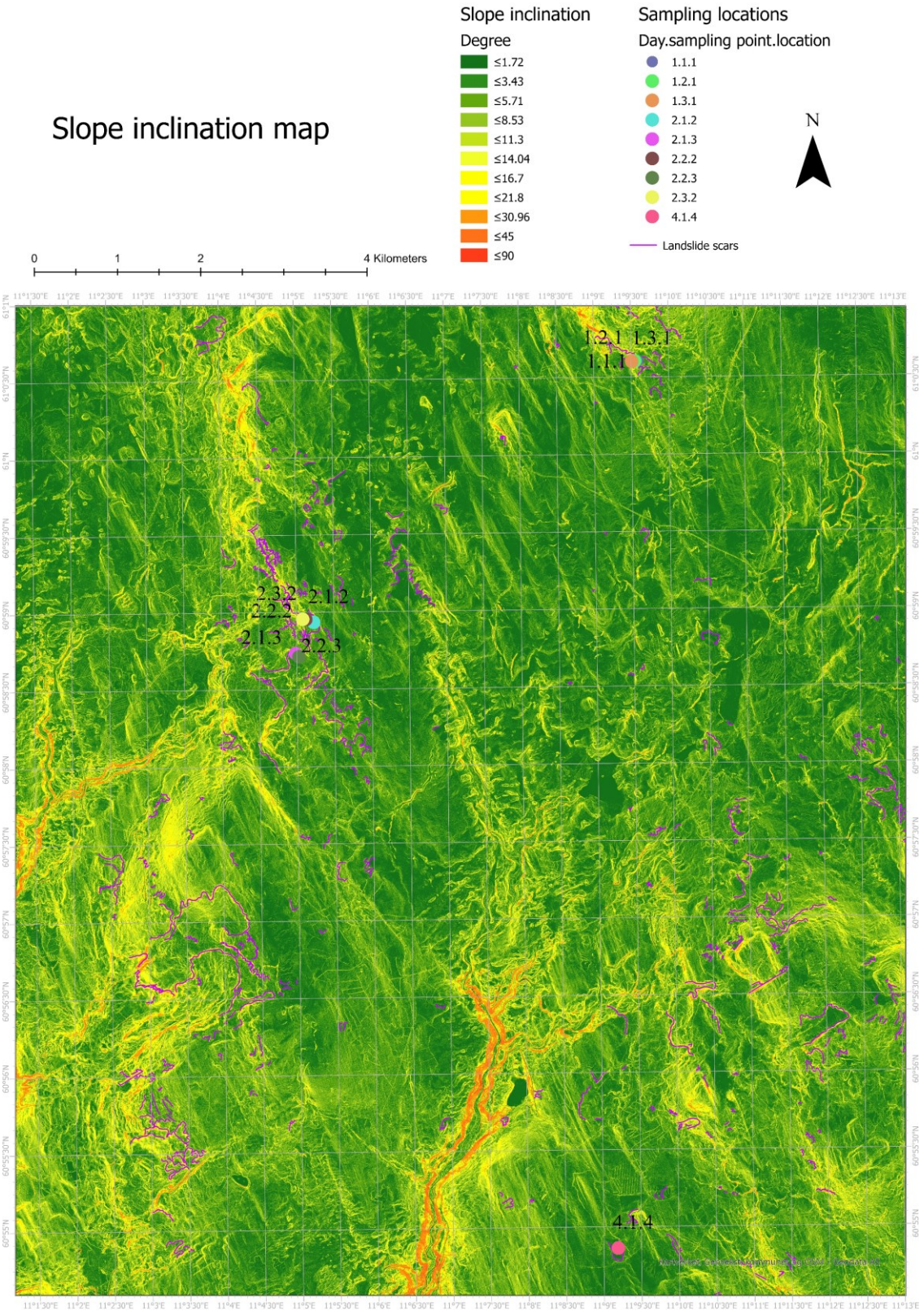

Figure 32 Slope inclination in ° over the sampled area.

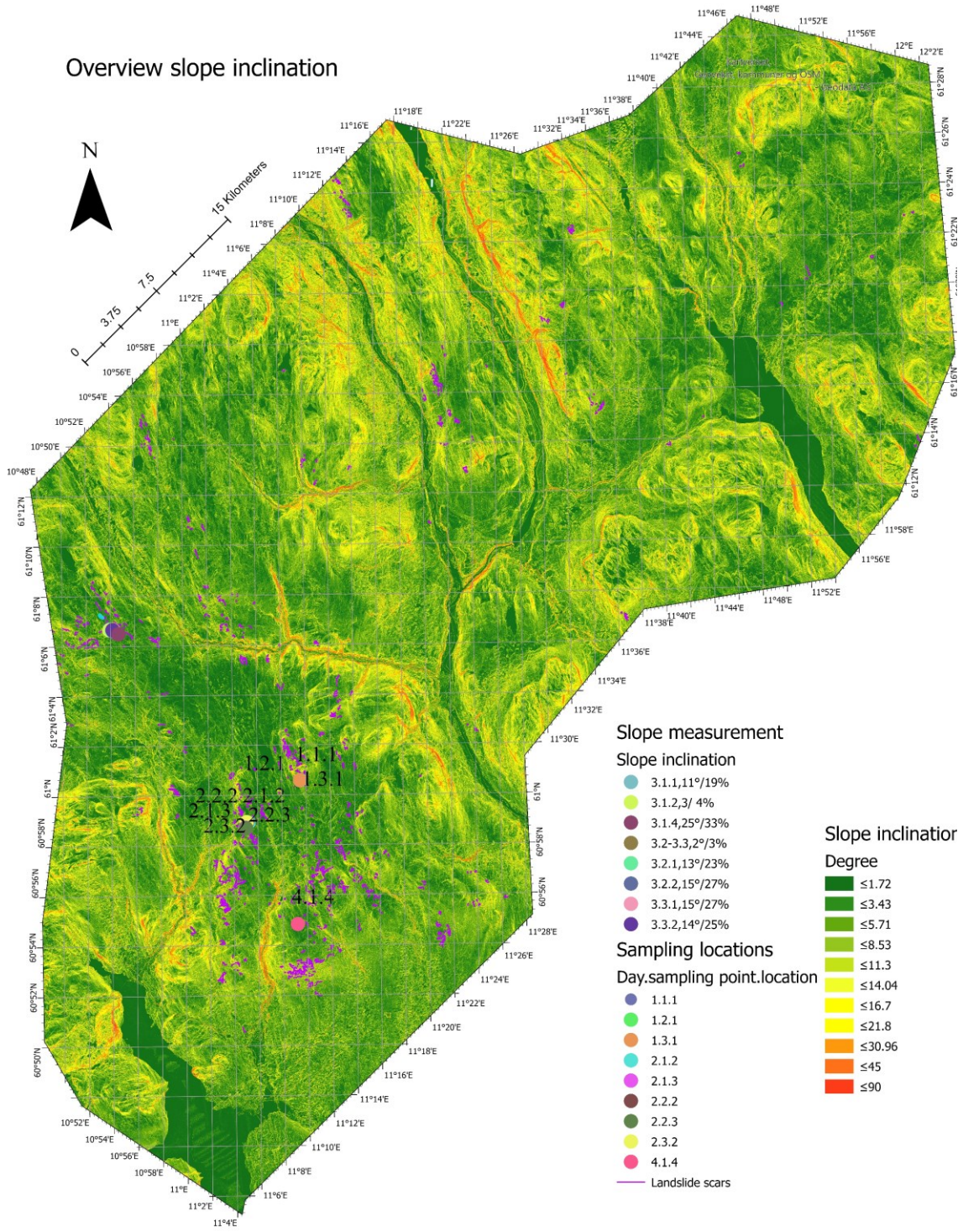

Figure 33 Slope map overview.

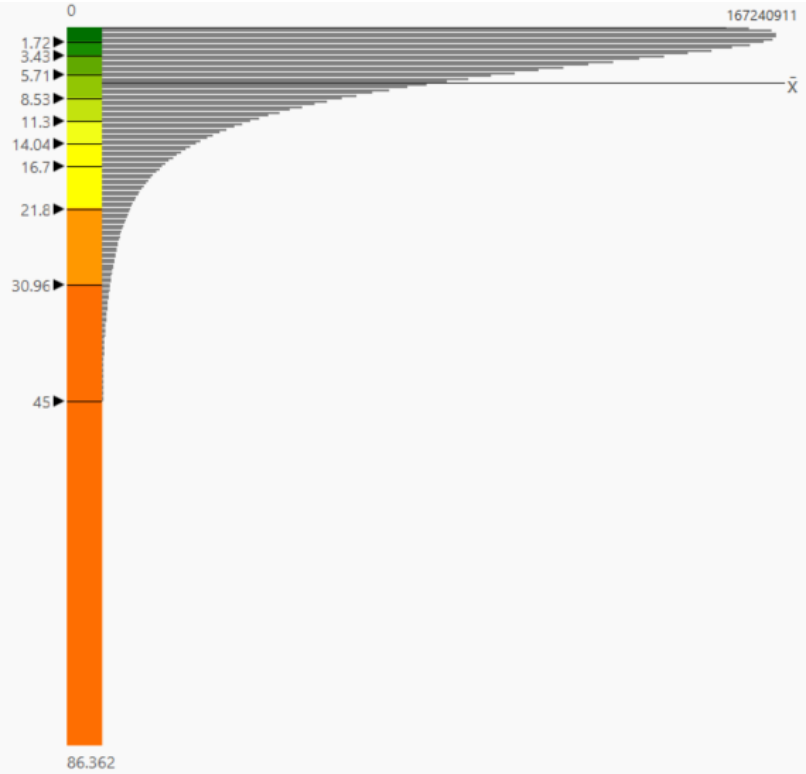

Figure 34 Histogram of the slope inclination values in °. The normal distribution is marked by a black line and x

As shown in Figure 34, the normal distribution of slope inclination values is about 6° for the whole investigated area. This coincides with the general impression from the slope map produced (Figure 32 and Figure 33) and inclination measured during the fieldwork. The only areas steeper than ≈ 20° are in relation to fluvial processes, as suggested in Chapter 5.2.1. Therefore, the slopes are, in general, far too gentle for gravitational slope processes to trigger landslides by themselves.

Chapter 5.2.3 Cut Fill

The cut and fill created in this thesis is, as mentioned in Chapter 4.4.1, based on a LiDAR scanning collected in 2020 (Chapter 1) and a synthetic raster created to mimic the terrain before the landslides (Chapter 4.4.1). This results in hypothetical results from the cut and fill process. As it is hard to map the landslides' deposition materials precisely, the approximations of mass movement are likely inaccurate. The delimitation of the deposition area is further challenging due to the possibility of widespread fluvial erosion. Liquefied mass might travel far away from its host material due to the viscose nature. Another factor challenging the delimitation of the deposition area is the land cover. Since the seismicity and landsliding occurred, peat and vegetation have grown on top of the surface, making it difficult to distinguish the deposited sediments. On the other hand, the scar left after a landslide is easier to distinguish, leading to a more accurate approximation of mass loss.

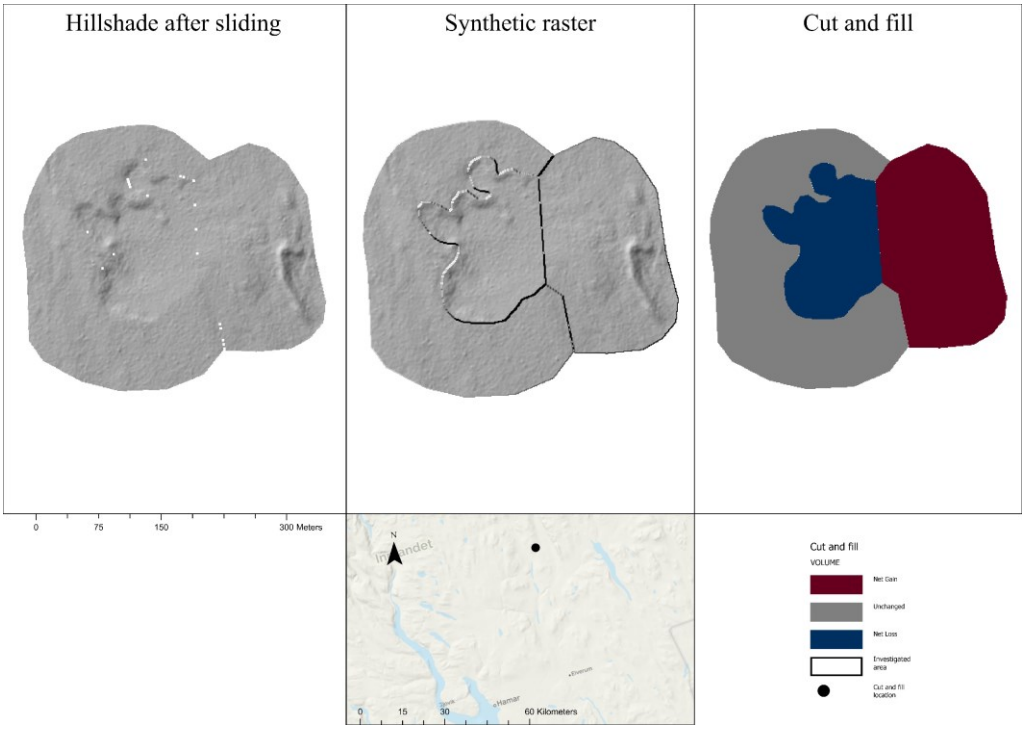

Figure 35 Cut fill landslide 1

Table 2 Cut and fill values landslide 1

Cut and fill 1

OBJECTID	Value	Count	AREA	VOLUME
1.00	1.00	43709.00	43708.07	0.00
2.00	2.00	30952.00	30951.34	-154756.71
3.00	3.00	18597.00	18596.60	92983.02

The cut and fill presented in Figure 35 is the graphic illustration of values presented in Table 2. About 60% of the lost material is found in the deposition area. This may result from poor delimitation, flawed calculations in the alteration of attribute values, or parts of the deposition material that might be transported with fluvial processes. A reason for estimating that this landslide occurred after the LGM and deglaciation is that it looks like the landslide materials cover parts of an esker.

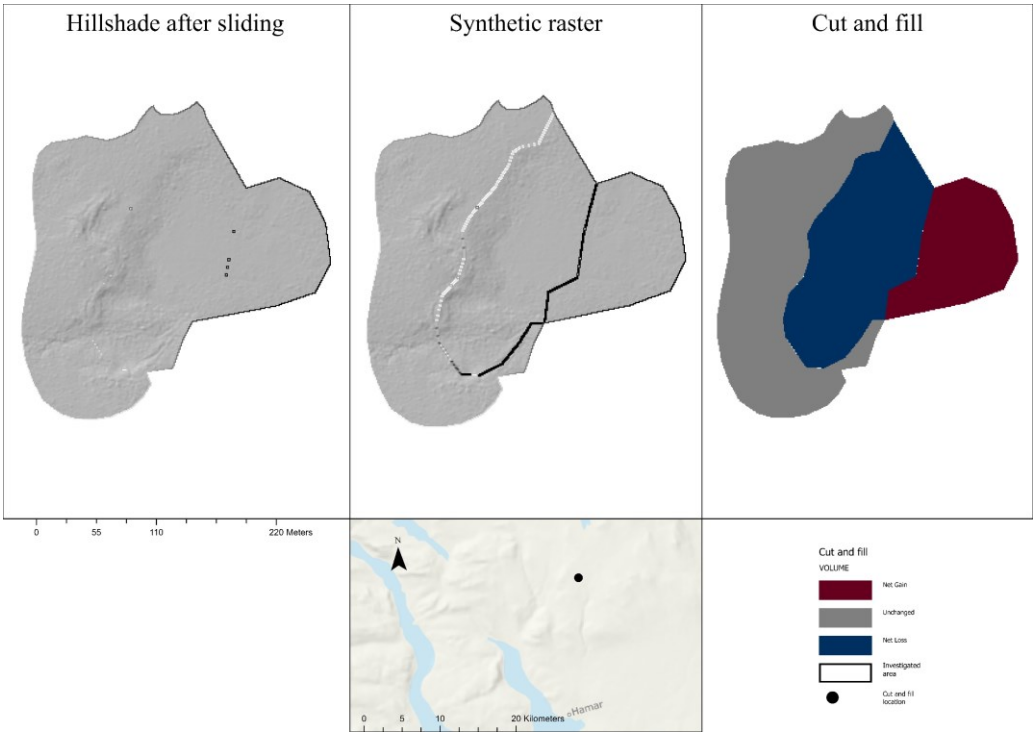

Figure 36 Cut fill landslide 2

Table 3 Cut and fill values landslide 2

Cut and fill 2

OBJECTID	Value	Count	AREA	VOLUME
1.00	1.00	24396.00	24395.48	0.00
2.00	2.00	17832.00	17831.62	89158.10
3.00	3.00	10075.00	10074.79	-50373.93

The cut and fill presented in Figure 36 is the graphic illustration of values presented in Table 3. About 56% of the lost material is found in the deposition area. This may result from poor delimitation, flawed calculations in the alteration of attribute values, or parts of the deposition material that might be transported with fluvial processes.

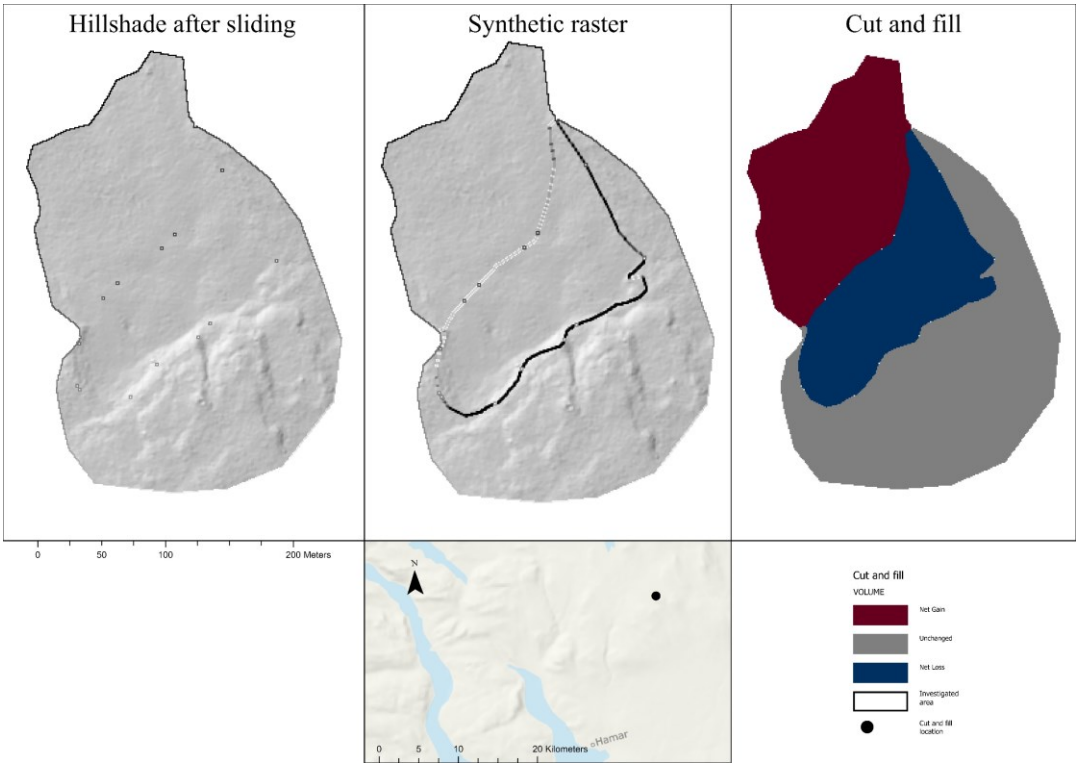

Figure 37 Cut fill landslide 3

Table 4 Cut and fill values landslide 3

Cut and fill 3

OBJECTID	Value	Count	AREA	VOLUME
1.00	1.00	17445.00	17444.63	-87223.14
2.00	2.00	26875.00	26874.43	0.00
3.00	3.00	14176.00	14175.70	70878.49

The cut and fill presented in Figure 37 is the graphic illustration of values presented in Table 4. About 81% of the lost material is found in the deposition area. This may result from poor delimitation, flawed calculations in the alteration of attribute values, or parts of the deposition material that might be transported with fluvial processes.

Chapter 5.3 Grain size analysis

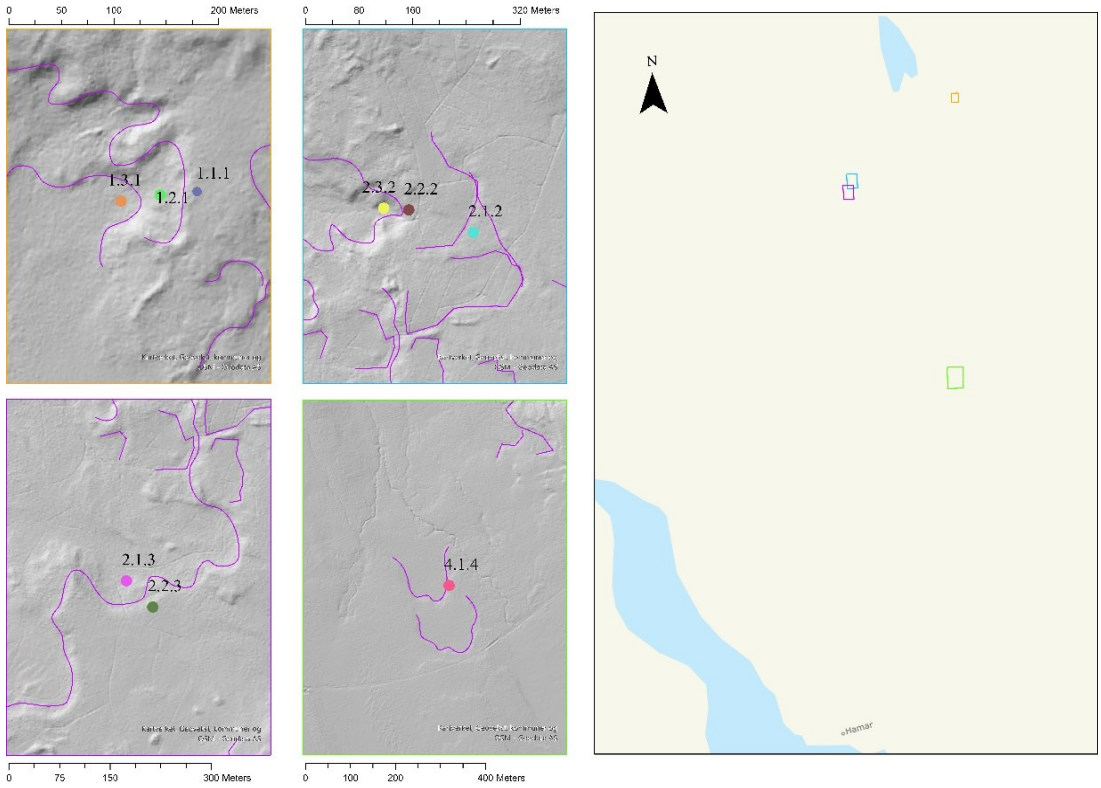

Figure 38 Overview of the sampling points. The colour of the border on each of the hillshades coincides with that of the extent indicator in the navigation map.

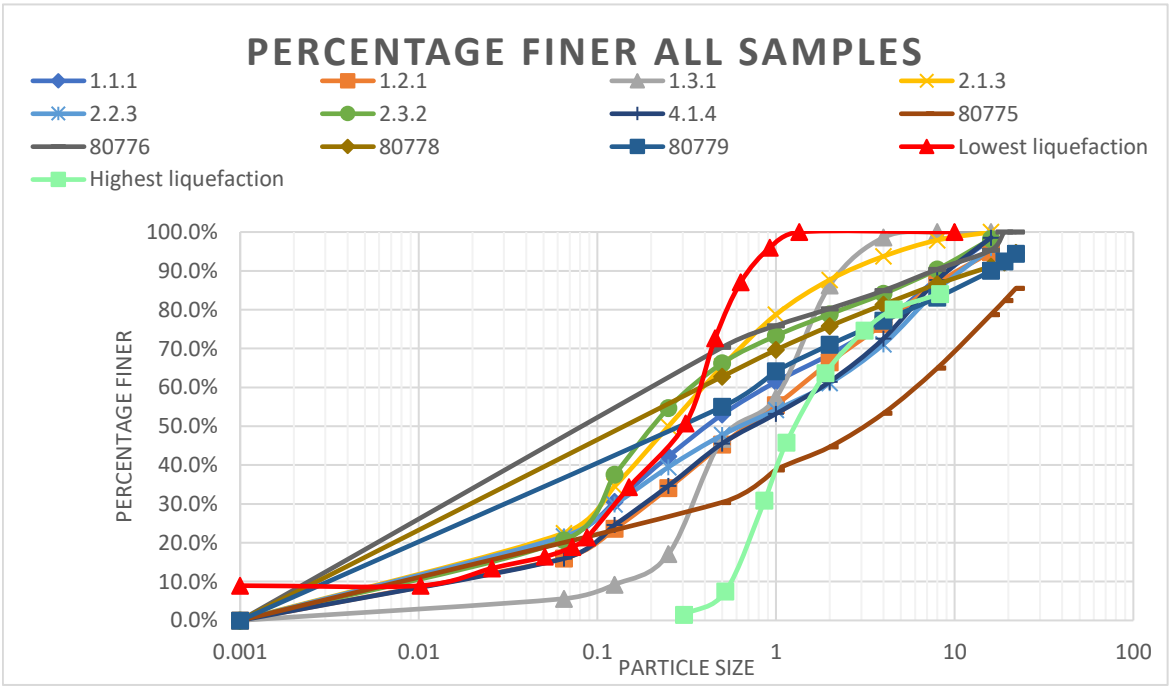

Figure 39 Logarithmic grain size distribution chart - all samples.

As seen in Figure 39, All samples collected, both specifically for this thesis and by NGU, coincide with one another. There are variations between them, but the general trend is similar. The samples retrieved through the fieldwork conducted and the samples provided by NGU have not been processed in the same way. The processing of the samples retrieved through fieldwork is described in Chapter 4.2 and Chapter 4.3. However, the samples provided by NGU were wet sieved, meaning that the sediments were not dried in advance. In addition, the plotted NGU values were sieved in sieves from 22mm down to 500µ. This means that the graphic illustration of the grain size distribution will vary to some degree. However, the analytic value will somewhat be the same, as the graphs still show some of the same characteristics. All the presented graphs (Figure 39, Figure 41, Figure 42, Figure 43, Figure 45, Figure 47, Figure 48, Figure 50, Figure 51, Figure 52, Figure 53, and Figure 54) contain a red and a green graph. The red graph (Lowest) and green graph (highest) are values described in Hermanns & Niedermann (2011) as the most liquefiable sands based on laboratory tests presented in Lee & Fitton (1969). The area in between the two lines is sands and silts, most likely to liquefy. In between the two lines, Hermanns & Niedermann (2011) placed 19 curves of sands liquefied during earthquakes in Japan, based on Kishida (1970). Red is considered the lowest boundary where sands and fines are most liquefiable, and light green is the boundary in which sand and fines are most liquefiable.

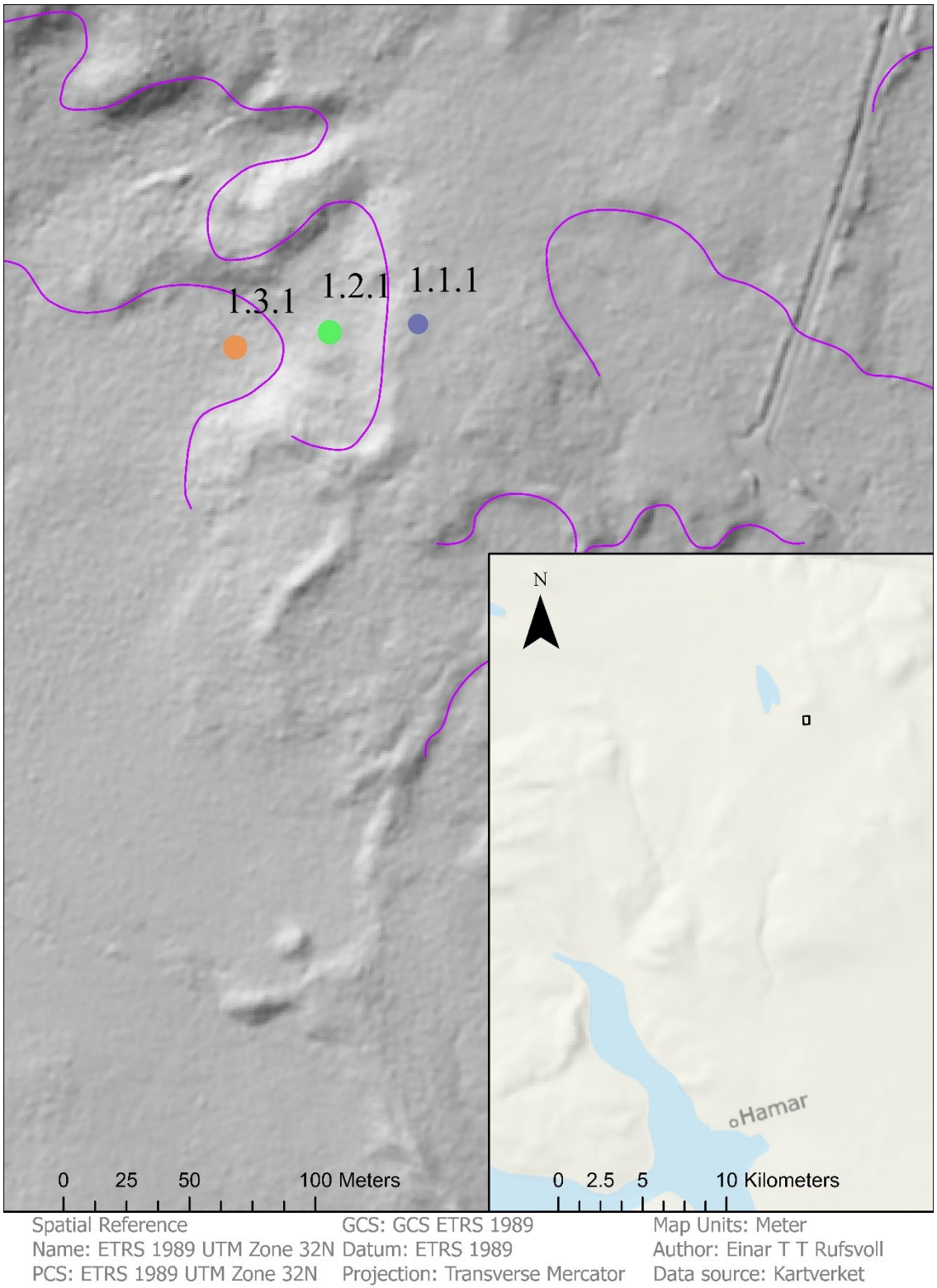

Figure 40 Location of sampling point 1.1.1, 1.2.1 and 1.3.1. Black square is the extent indicator showing where the sample is collected.

The first sampling location (Figure 40) yielded three samples suitable for a grain size distribution analysis, and the results are presented in the tables in the appendix and figures

below: Figure 41 Tabell 2 and Tabell 3, Figure 42, Tabell 4 and Tabell 5, Figure 43, Tabell 6 and Tabell 7.

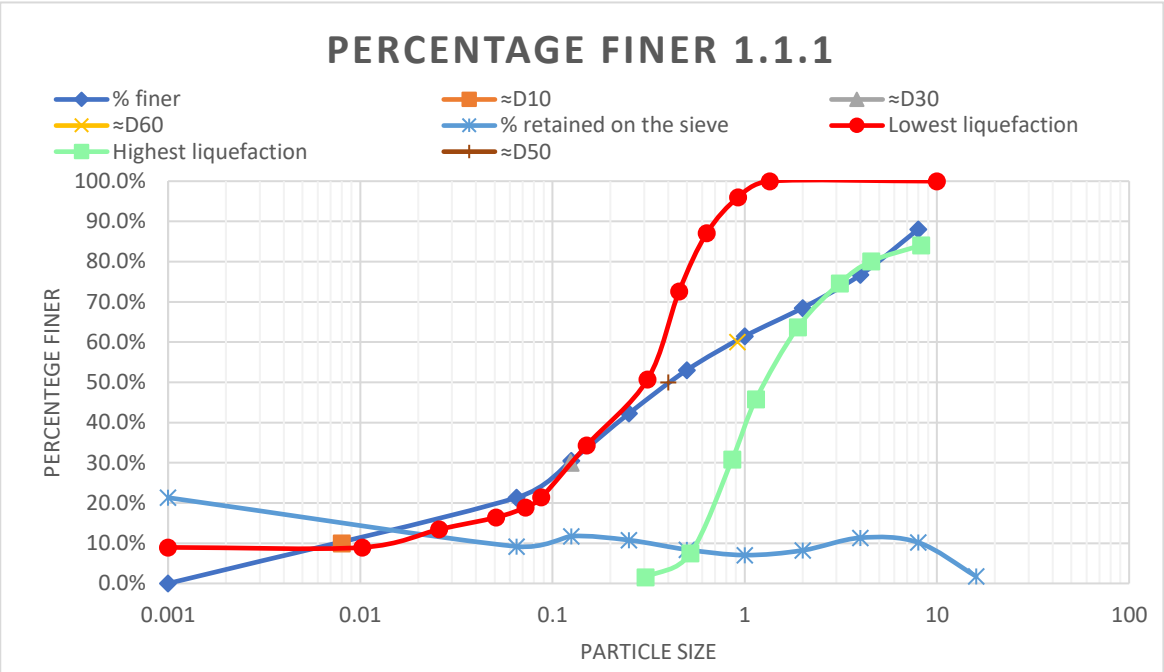

Figure 41 Percentage finer plotted in a logarithmic scatterplot graph with D10-, D30-, D50-, and D60-values.

The plotting of percentage finer for the first sample (Figure 41) shows a relatively well-graded soil. <21.33% fines (silt and clay). A bit of a "hump" between 125µ(30.53%) and 1mm (61.45%). Subtle S-shape. The C_c and C_u value of Tabell 2 is, indicating a poorly graded soil. As C_c is <3 and C_u is >6 indicates that the soil is, to some degree, well graded but has some qualities of poorly graded soil.

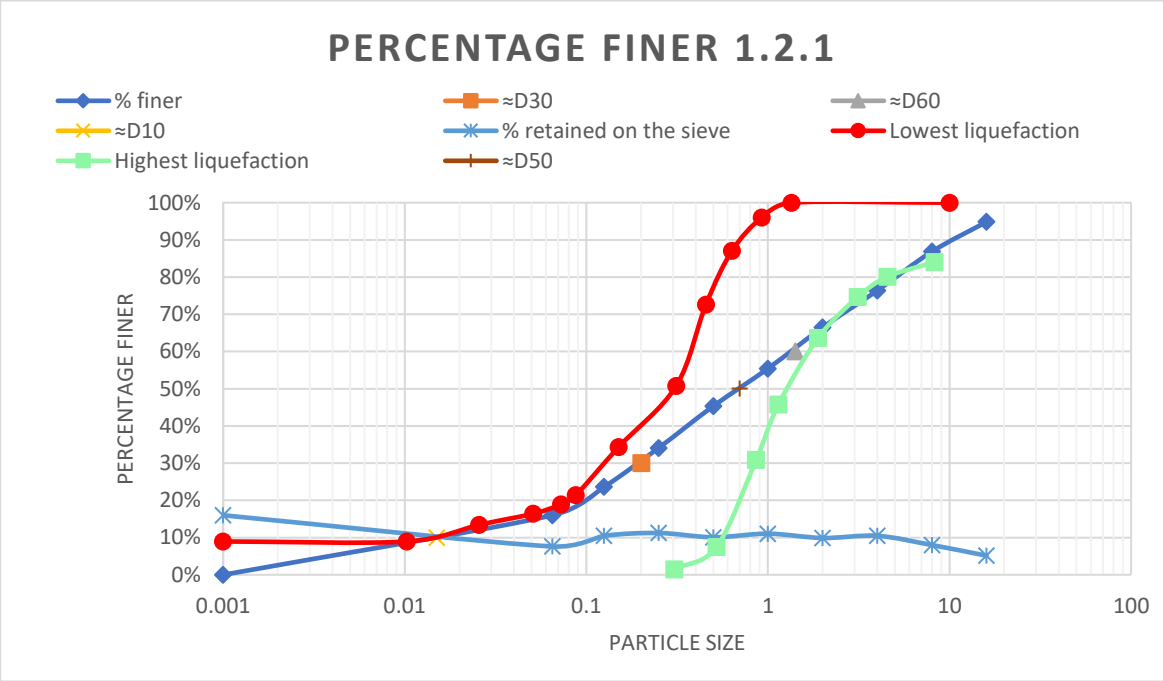

Figure 42 Percentage finer plotted in a logarithmic scatterplot graph with D10-, D30-, D50-, and D60-values.

The plotting of percentage finer for the second sample (Figure 42) indicates a well graded soil. <16% fines (silt and clay). The Cc in Tabell 5 reinforces this notion. However, the Cu indicates a poorly graded soil with values well over 3.

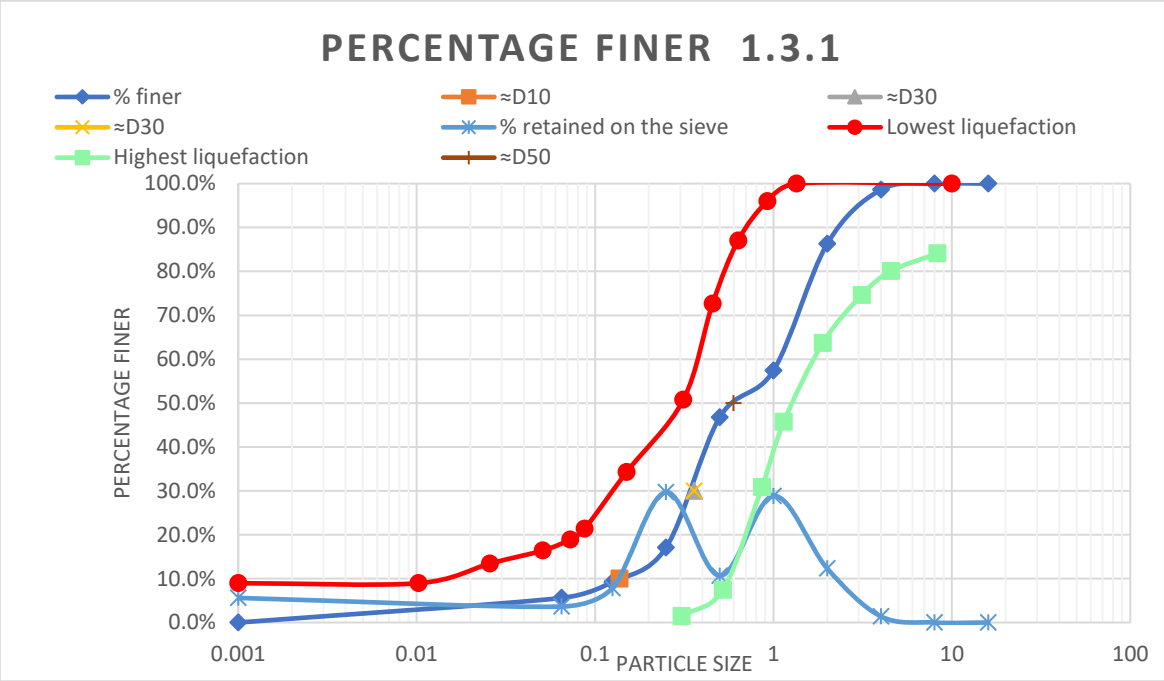

Figure 43 Percentage finer plotted in a logarithmic scatterplot graph with D10-, D30-, D50-, and D60-values.

The plotting of percentage finer is somewhat gap- and well graded soil. Little fine material <65µ and little 500µ-1mm and almost no particles bigger than 4mm. <5.6% fines (silt and clay). Reinforced by C_u but not by the C_c values in Tabell 7.

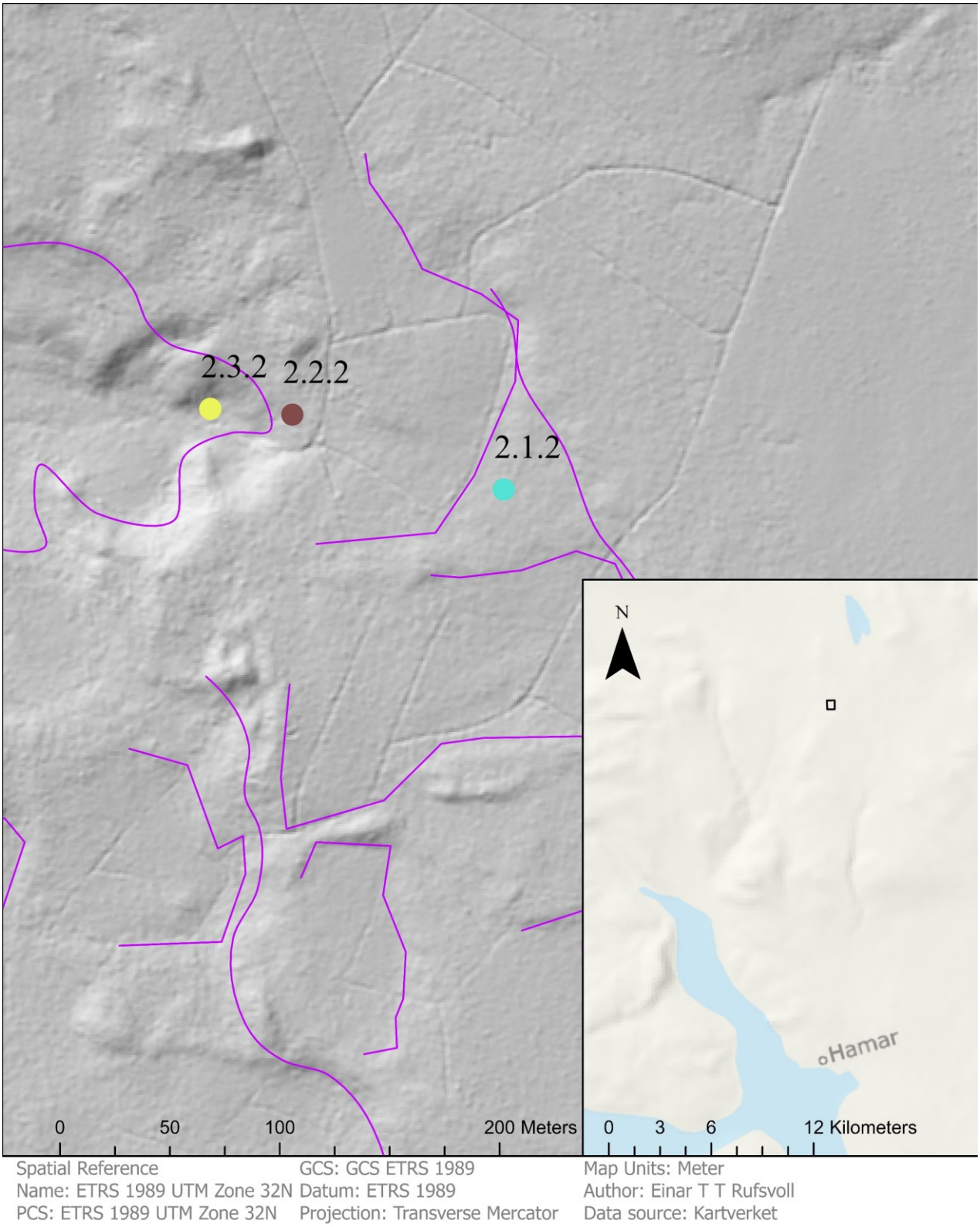

Figure 44 Location of sampling point 2.1.2, 2.2.2 and 2.3.2. Black square is the extent indicator showing where the sample is collected.

Figure 44 shows the sampling points at location 2.

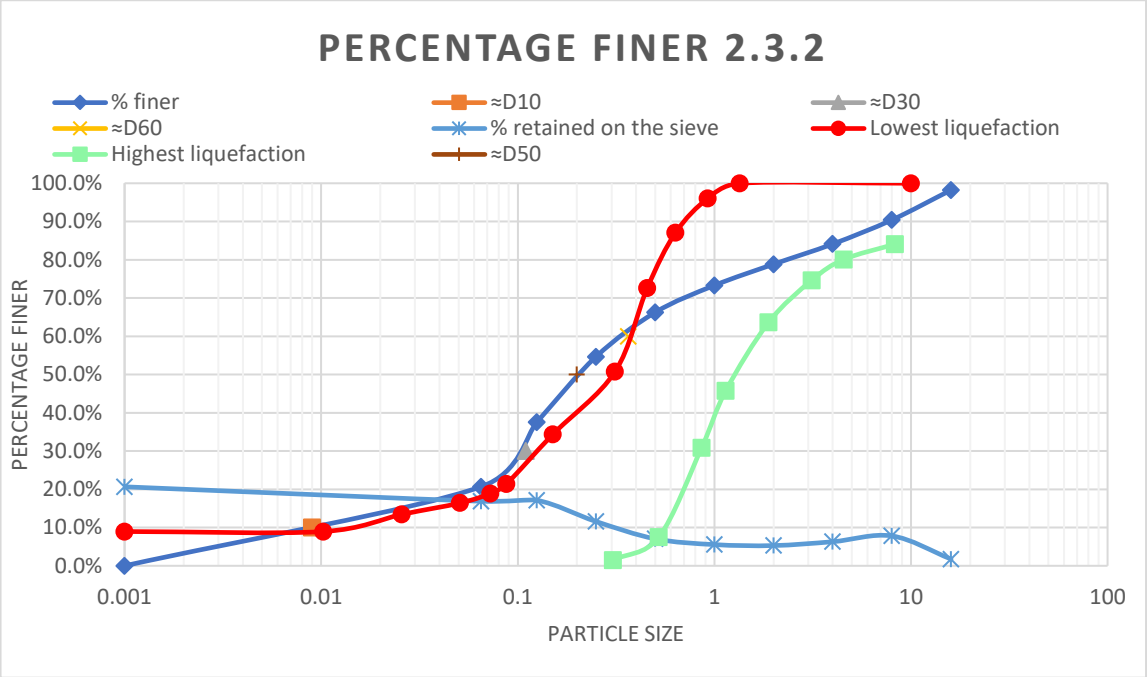

Figure 45 Percentage finer plotted in a logarithmic scatterplot graph with D10-, D30-, D50-, and D60-values.

The plotting of percentage finer is somewhat well graded soil. A “hump” between 125µ and 1mm. <20.56% fines (silt and clay). Reinforced by Cu but not by the Cc values in Tabell 9.

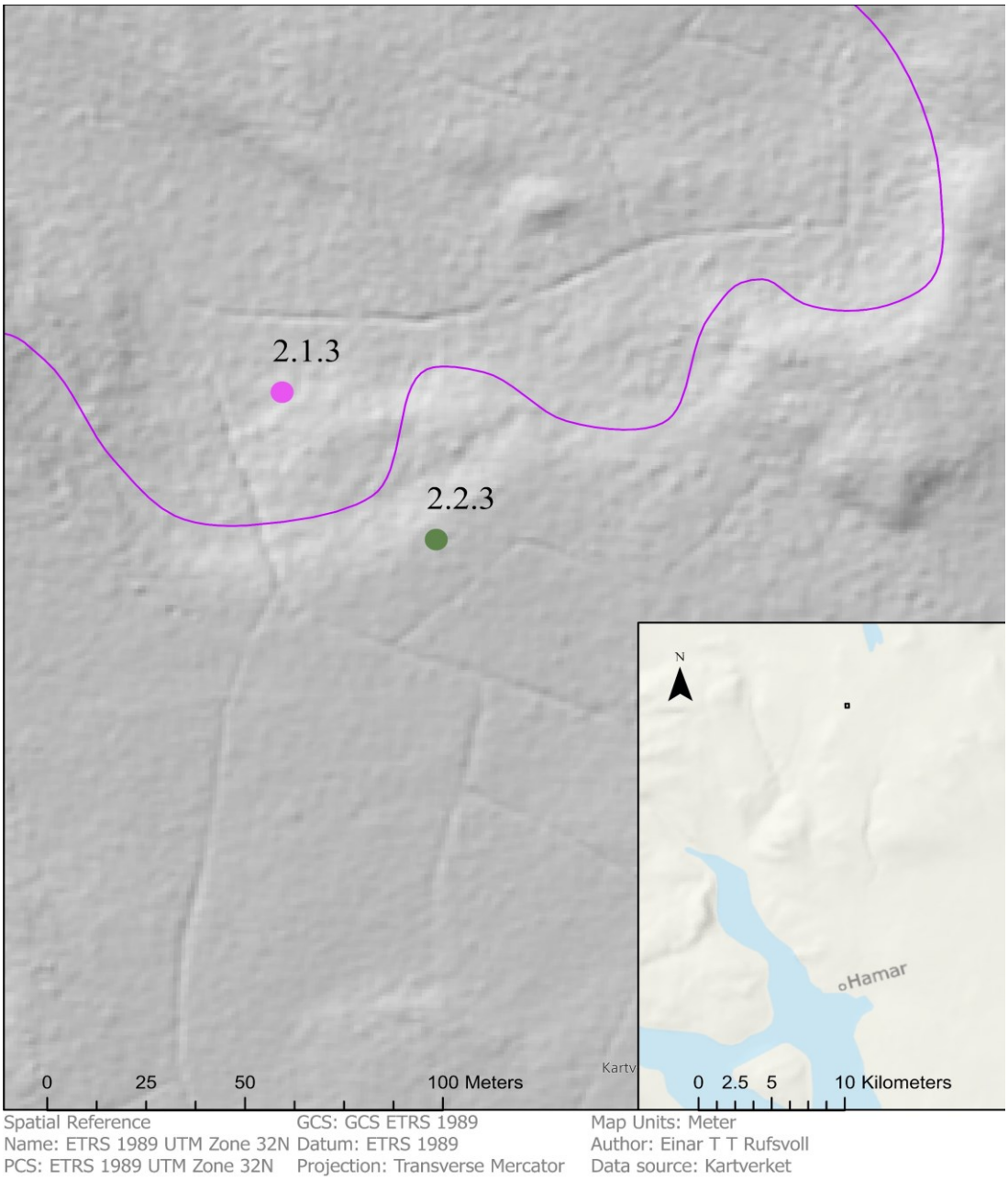

Figure 46 Location of sampling point 2.2.3 and 2.1.3. Black square is the extent indicator showing where the sample is collected.

Figure 46 shows sampling points at location 3.

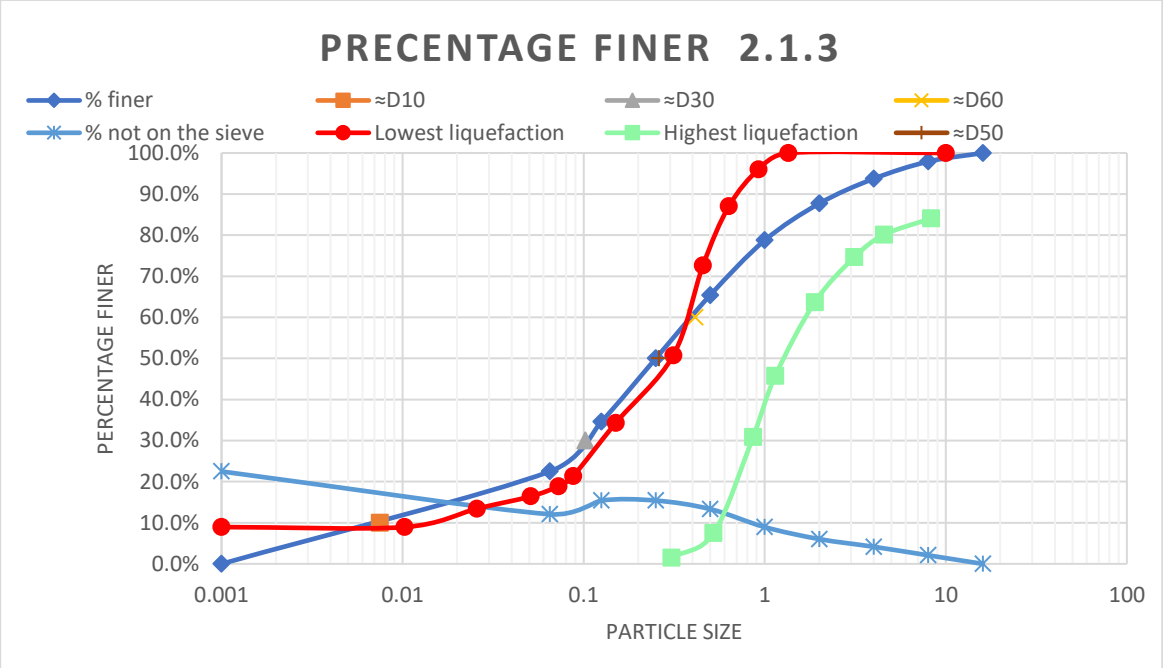

Figure 47 Percentage finer plotted in a logarithmic scatterplot graph with D10-, D30-, D50-, and D60-values.

The plotting of percentage finer is yo some degree well graded soil. The sample consists of <22.5% fines (silt and clay), and <6.25% of the sample is over 4mm. Reinforced by Cu but not by the Cc values in Tabell 11. A “hump” present in coarse sand.

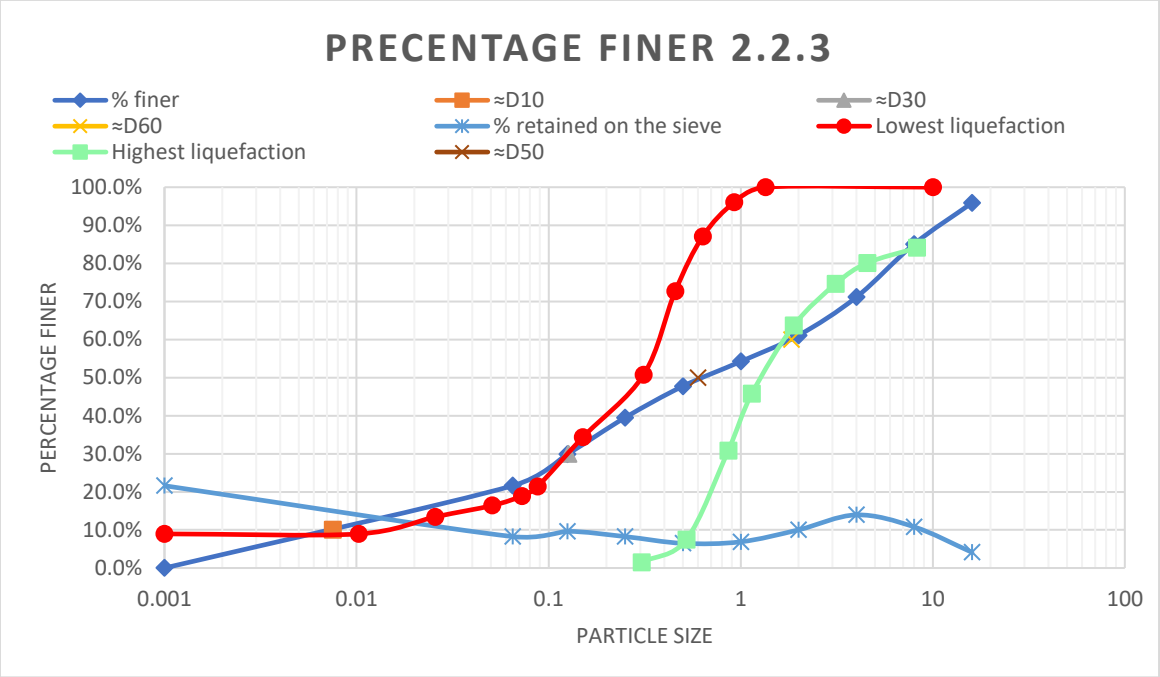

Figure 48 Percentage finer plotted in a logarithmic scatterplot graph with D10-, D30-, D50-, and D60-values.

The plotting of percentage finer is well graded, slightly S-shaped curve. “Hump” in fine to medium sand - between 125µ (29.86%) and 1mm (54.22%). The sample consists of <21.61% fines (Silt and Clay). C_c and C_u values in Tabell 12 reinforce the notion of well graded distribution.

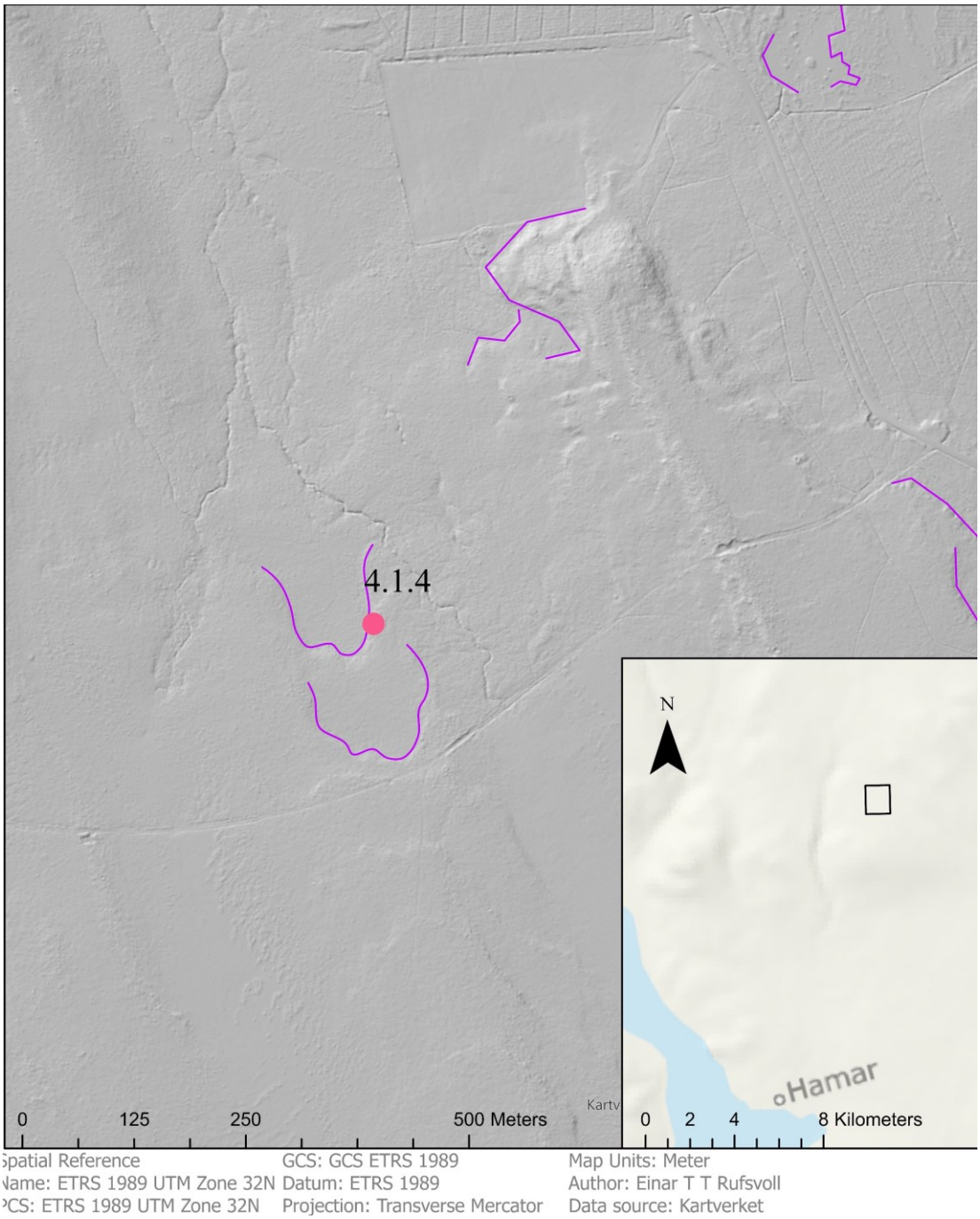

Figure 49 Location of sampling point 4.1.4. Black square is the extent indicator showing where the sample is collected.

Figure 49 shows sampling points at location 4.

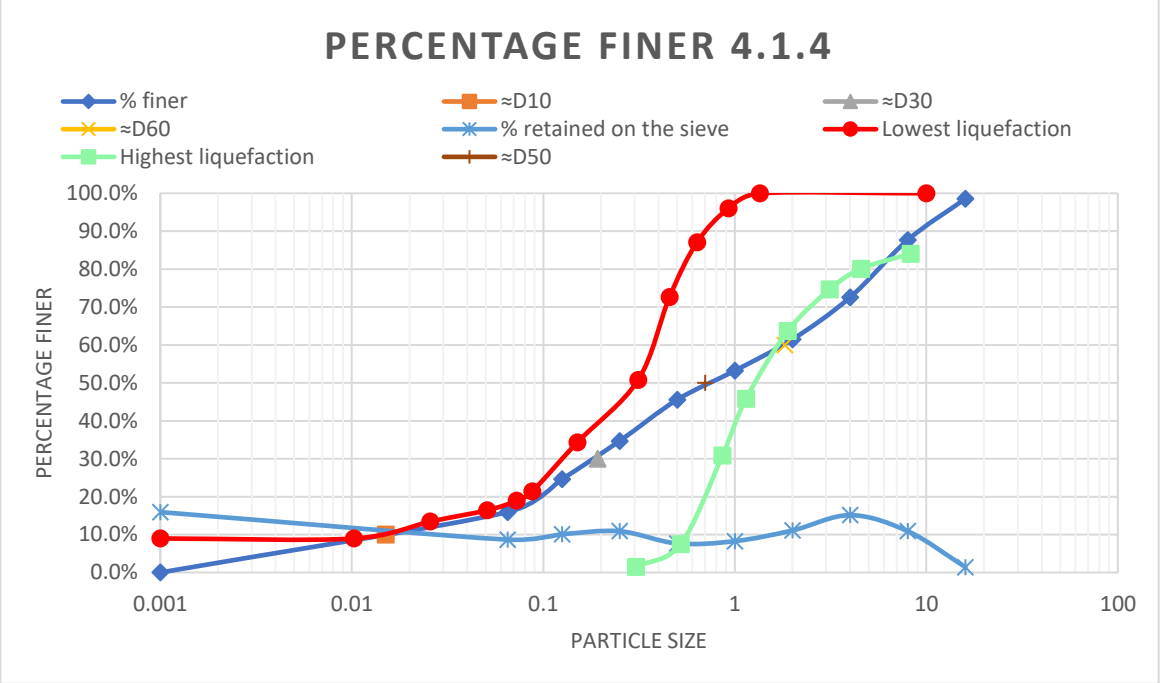

Figure 50 Percentage finer plotted in a logarithmic scatterplot graph with D10-, D30-, D50-, and D60-values.

The plotting of percentage finer is well graded soil. A "hump" between 65µ (15,97%) and 1mm (52.23%) – fine to medium sand. Depression between 1mm (53.23%) and 4mm (72.58%) – medium to coarse sand. The sample consists of <15.93% fines (silt and clay). The C_c and C_u value in Tabell 15 reinforces this notion.

Chapter 5.3.1 NGUs sediment samples and grain size distribution

The samples are analysed by Marit Sigrid Halle (Laboratory of NGU) and have been wet sieved, meaning that they were not dried in advance, rather saturated with water. The wet sieving procedure results were presented in an excel document provided by Ola Fredin (NGU/NTNU). The results were presented in multiple sheets to describe the process and with different data. The data most relevant in this thesis was presented on the last page of the document. Other than wet sieving rather than dry sieving, the results presented in the document were mainly cumulative percentages rather than grams. The results presented as grams, as done in the samples presented above, were data for sieves of 500µ, 1mm, 2mm, 4mm, 8mm, 16mm, 19mm and 22mm. This results in some dissociation between the presented results.

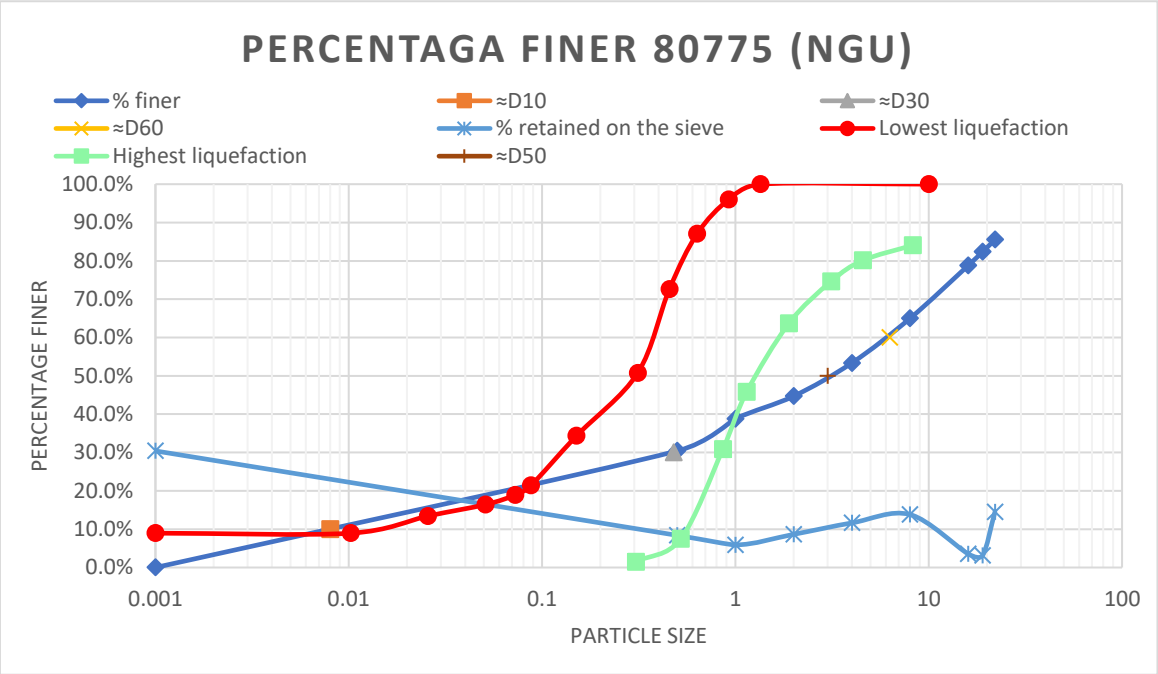

Figure 51 Percentage finer plotted in a logarithmic scatterplot graph with D10-, D30-, D50-, and D60-values.

The fractions of the sample distinguishable from one another are well graded. However, this is not reinforced by the C_u nor by the C_c presented in Tabell 17. A reason for this might be the uncertainty within the lowes fraction of the sample. It could be that if all fractions from 65µ up to 500µ were presented, the graph would present a poorly graded soil.

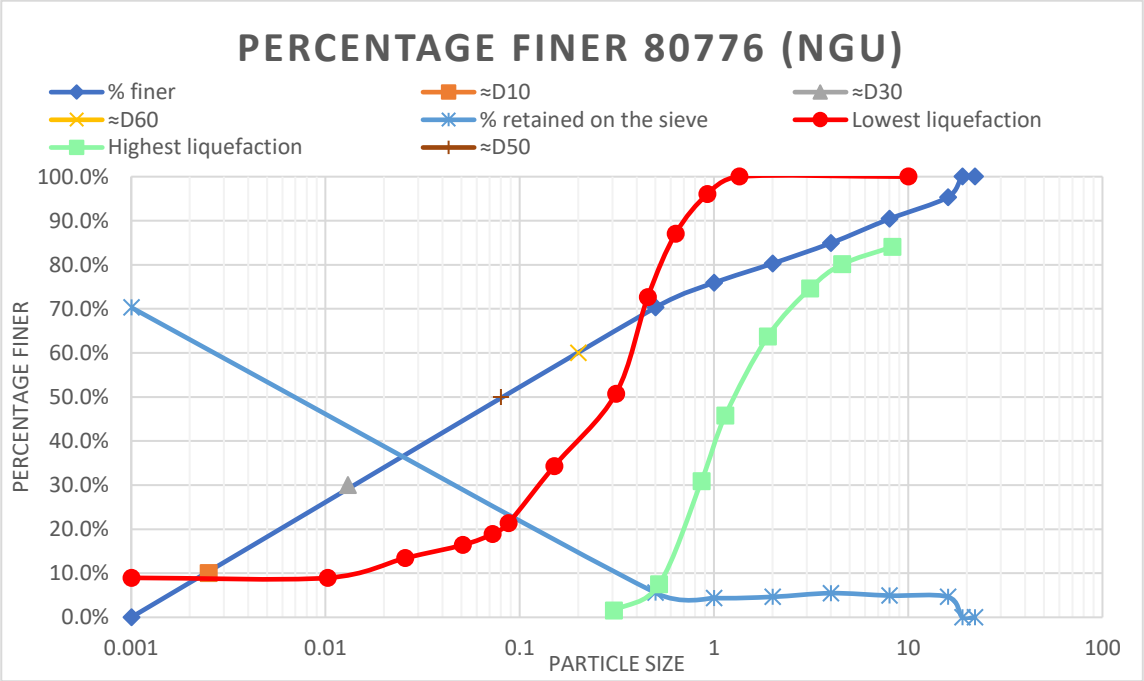

Figure 52 Percentage finer plotted in a logarithmic scatterplot graph with D10-, D30-, D50-, and D60-values.

The fractions of the sample distinguishable from one another are well graded, with a large portion of fines. However, this is not reinforced by the C_u nor by the C_c presented in Tabell 19. A reason for this might be the uncertainty within the <500µ fraction of the sample. It is possible that if all fractions from 65µ up to 500µ were presented, the graph would present a poorly graded soil.

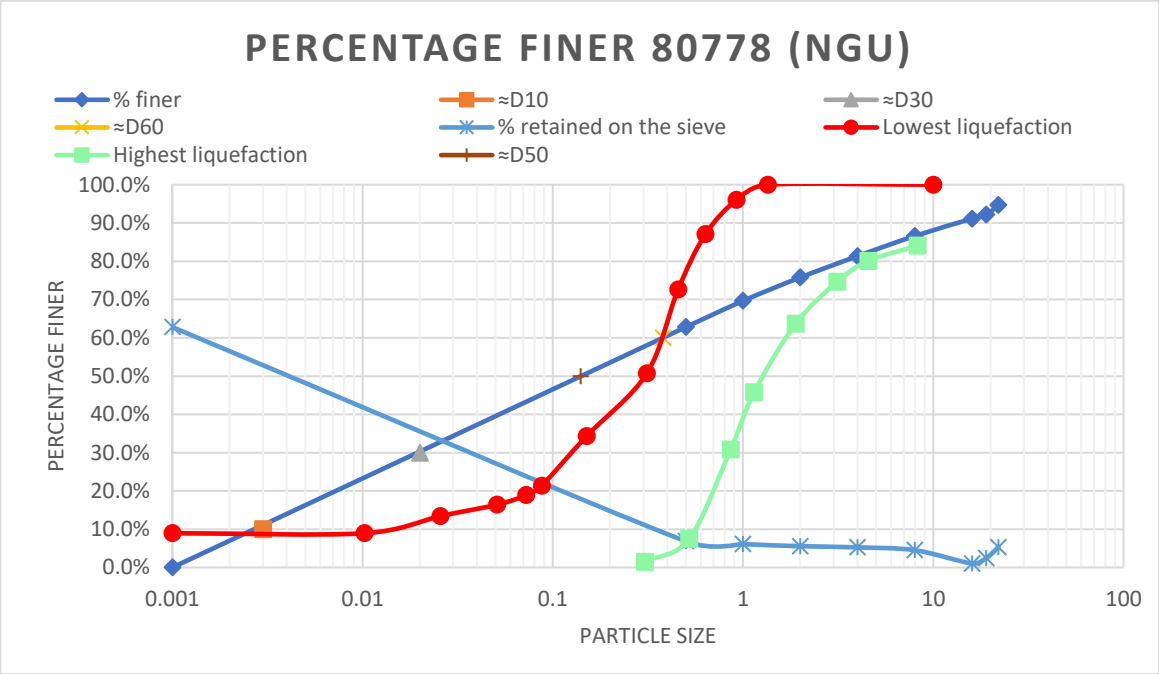

Figure 53 Percentage finer plotted in a logarithmic scatterplot graph with D10-, D30-, D50-, and D60-values.

The fractions of the sample distinguishable from one another are well graded. However, this is not reinforced by the C_u nor by the C_c presented in Tabell 21. A reason for this might be the uncertainty within the lowes fraction of the sample. The sample might have presented as poorly graded if all fractions between 65µ up to 500µ were presented.

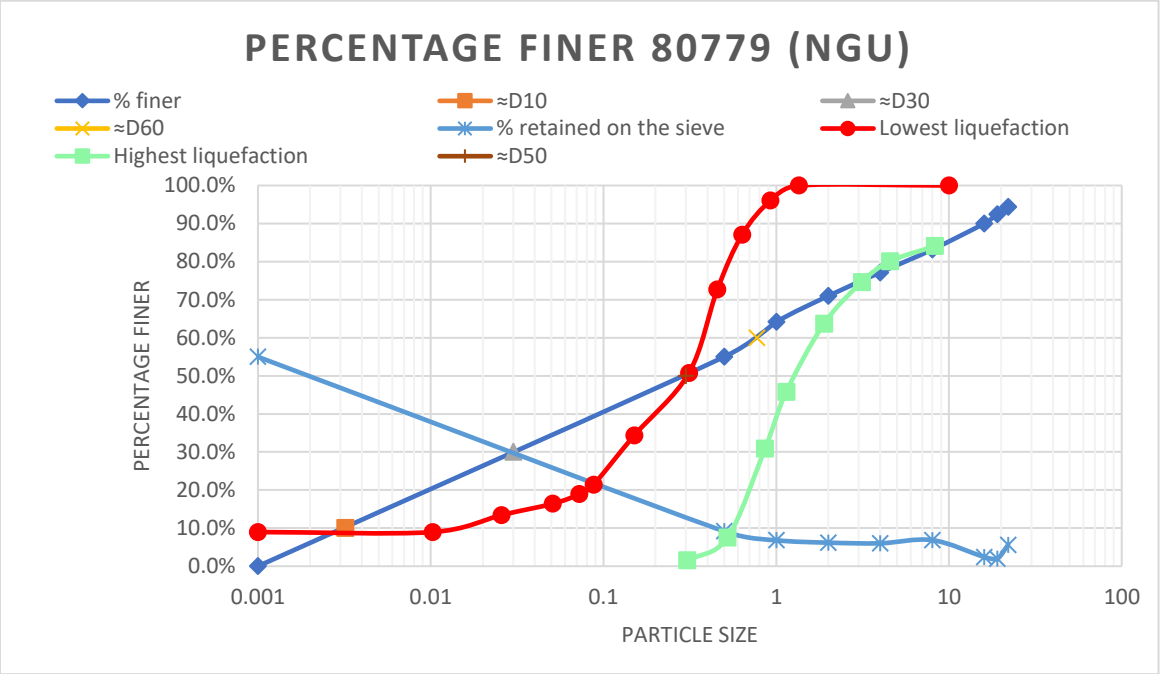

Figure 54 Percentage finer plotted in a logarithmic scatterplot graph with D10-, D30-, D50-, and D60-values.

The fractions of the sample distinguishable from one another are well graded. However, this is not reinforced by the C_u nor by the C_c presented in Tabell 23. A reason for this might be the uncertainty within the lowes fraction of the sample. It is reasonable to assume that if all fractions from 65µ up to 500µ were presented, the graph would present a poorly graded soil.

Chapter 6 Discussion

The results of this thesis, in addition to the theory, aims, as mentioned in Chapter 1.1 and Chapter 1.1.1, to test the following hypothesis: *Most or all of these landslide scars were derived through post-glacial seismicity (earthquakes)*. This chapter will see the results and theory presented in light of other studies within the same topic in the hopes of finding an answer to the hypothesis. Even though the study of PGS and landslide induced by earthquakes is relatively sparse in Norway and focuses mainly on the northern regions, the phenomena are well documented in other regions. As mentioned in Chapter 1, Chapter 3.3.1, and Chapter 3.3.2, some landslide scars and faults found in Sweden and Finland have been linked to PGS and GIA. In addition, landslides resulting from earthquakes and liquefaction are generally comparable to PGS induced as the primary mechanisms are the same (Jibson, 2009). Jibson points out three main steps involved in analysing paleoseismic landslides: "(1) identify a feature as a landslide, (2) date the landslide, and (3) show that the landslide was triggered by earthquake shaking" (Jibson, 2009, p. 565). Therefore, the discussion aims to get closer to a definite answer if the landslide in the area surrounding Brumunddalen can be explained by seismic activity.

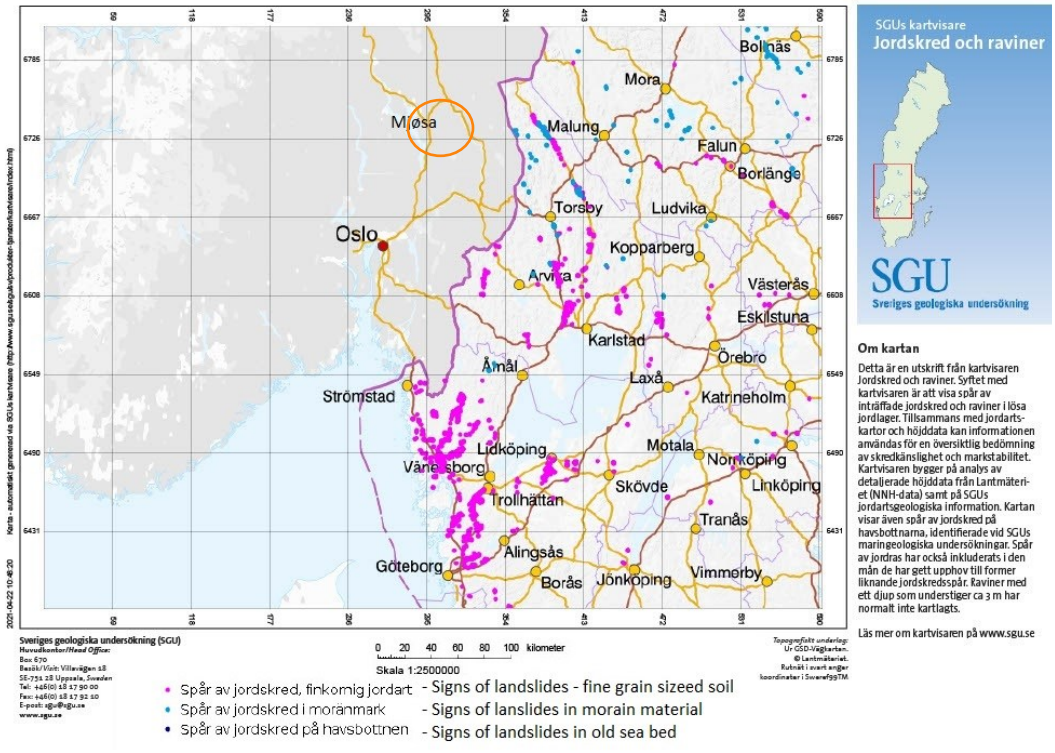

Figure 55 Landslides mapped in Sweden (SGU, 2016). Orange circle is the mapped and studied area around Brumunddalen. Blue dots (spår av jordskred I moränmark/traces of slides in morain surface) is the most interesting in regards to the results presented in thiis thesis

The clustering of mapped landslides (Figure 55) in south-western Sweden is among the areas where the Fennoscandian ice-sheet was thickest during the LGM (Figure 56). It is expected that the area covered by the thickest ice becomes most GIA depressed during the glaciation. As a result, the same area has the most GIA (Olesen et al., 2013). The area shown in Figure 55 is among the areas that in Figure 56 is covered by the thickest ice. This means that this area is expected to experience the most uplift and is most likely to faulting or experience seismicity.

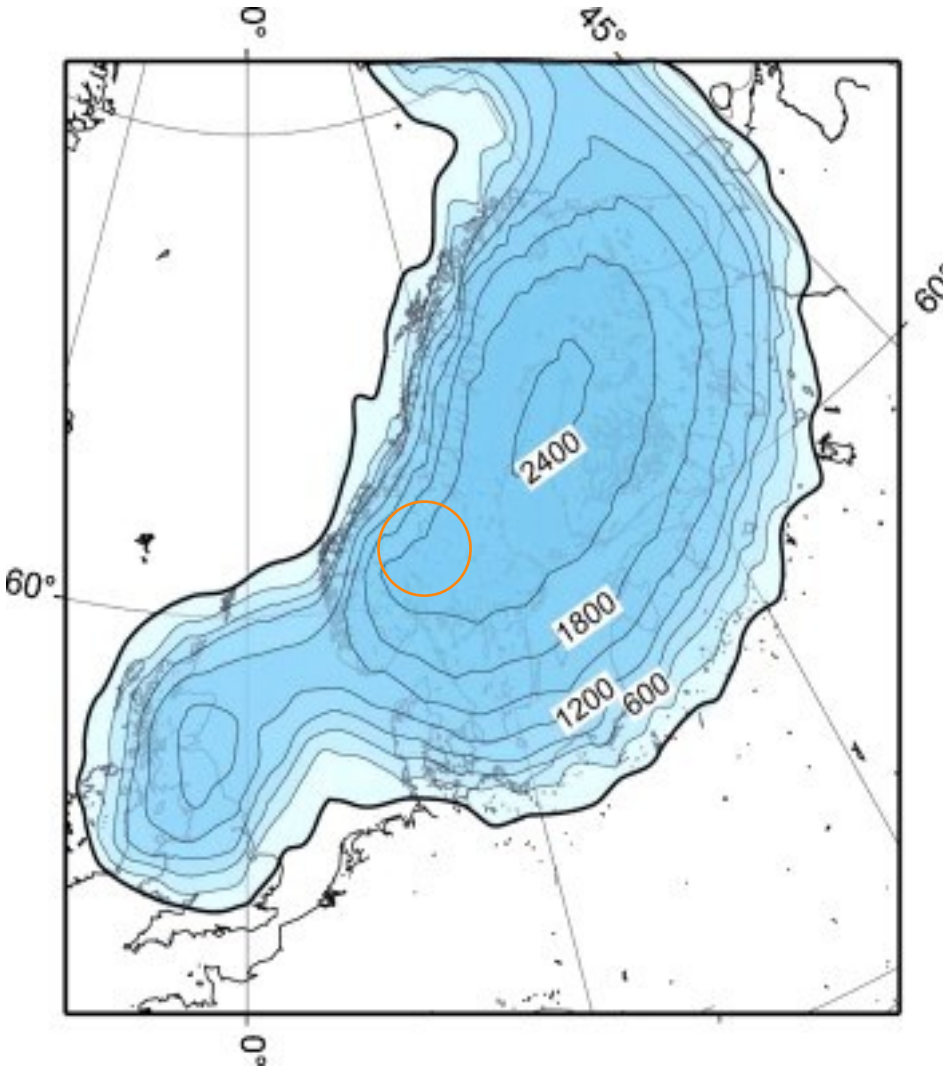

Figure 56 Fennoscandian ice thickness (in m) and extent during the LGM (From Holger & Wu, 2011). Orange circle contains the studied area around Brumunddalen, and some of the area shown in Figure 55.

Olesen et al. (2003) postulate that a significant seismic puls most likely followed each of the multiple deglaciations in mainland Fennoscandia and Scotland during the last 600 000 years (Olesen et al., 2003; Olesen et al., 2013). The seismic activity and GIA following the deglaciations could trigger rock avalanches and lansliding. If deposition from these hit lakes or fjords, tsunamis could form – generating the most significant seismic risks in Norwegian society (Olesen et al., 2013). Olesen et al. (2013) point out that the abundance of liquefaction

structures in the Rana area and cluster of rock avalanches in western Norway can be interpreted as a sign of large prehistoric earthquakes.

Faults often occur in old weakness zones and can be triggered by earthquakes, isostatic adjustment or tectonic stress (Olesen et al., 2013). The faulting sends out seismic waves when stress is released, and if not triggered by an earthquake, the faulting in and of itself can trigger landsliding. Therefore, areas where faulting has occurred, sliding due to seismic waves have also been mapped. In large parts of Norway, Sweden, and Finland, these faults are quite apparent and have been mapped (Olesen et al., 2003; Jibson, 2009; Olesen et al., 2013; Smith et al., 2014; Sutinen et al., 2014; Palmu et al., 2015; Mangerud et al., 2018; Ojala et al., 2019). In the Brumunddalen area, no faults have been mapped throughout this thesis or in advance by Ola Fredin and Marie Keding (Mangerud et al., 2018), probably because the faults are old and appear as crustal weakness zones in valleys or rivers, and potential fault throws are not visible in today's terrain (O. Fredin, personal communication, 2021). The faulting process will, therefore, not be emphasized in this thesis.

A rule of thumb to identify landslide scars is that they usually present themselves through "anomalous topography, including arcuate or linear scraps, backwards-rotated masses, benched or hummocky topography, bulging toes, and ponded or deranged drainage. Abnormal vegetation type or age is also common" (Jibson, 2009, p. 567), although this is most common for landslide scars where the vegetation has not yet bounced back. Jibson (2009) further points out that disruptive landslides are more common in regards to earthquakes than coherent types. When looking at the field observations, it becomes clear that there is a distinct difference between the surface coverage in the landslide scar and the surrounding areas, as disclosed in Chapter 5.1. The scar has denser soil and less vegetation covering the surface, while the surrounding areas have a thicker layer of vegetation, and the soil is easier to dig. Furthermore, when manually mapping and marking the proposed landslides, it becomes evident that the surface has experienced processes other than erosion.

A common way to analyse paleoseismic landslide events is to analyse them on a regional level, as landslides induced by earthquakes usually encompasses the whole area affected by the shakings (Jibson, 2009). This method is best suited if a historical record of earthquakes in the area is available, as large storms can trigger similar landsliding. However, the placement of landslide scars can indicate whether earthquakes or storms have caused the sliding.

Landslides located at the base of slopes are more commonly caused by storms, while sliding due to seismic activity is more widespread over an entire area. As seen in Figure 30, the landslide distribution does not follow a distinct pattern at the base of the slopes but is rather distributed throughout the entire area (Jibson, 2009).

Jibson (2009) presents Crozier's six criteria to support seismically induced landslides in New Zealand, also used by Smith et al. (2014) and Ojala et al. (2019). In regards to the findings in this research, three of the six criteria are to some degree present, while the other three are clearly present. Jibson (2009, p. 572) specifies that "the more of these criteria that are satisfied, the stronger the case for seismic origin" is. The six criteria are as follows:

> (1) ongoing seismicity in the region, which has triggered landslides; (2) coincidence of landslide distribution with an active fault or seismic zone; (3) geotechnical slope-stability analyses showing that earthquake shaking would have been required to induce slope failure; (4) large size of landslides; (5) presence of liquefaction features associated with the landslides; and (6) landslide distribution that cannot be explained solely on the basis of geological or geomorphic conditions. (Jibson, 2009, p. 567)

The first of these six criteria that relate to the research conducted is (3). In general, it relates to the grain size distribution and, more specifically, for this area, the slope inclination measured during the fieldwork and in GIS. A slope is considered stable if the incline is below ≈ 25° (Norges vassdrags- og energidirektorat, 2011; Bråthen et al., 2020), meaning that the slope is not prone to failure due to "normal" slope processes below ≈25-30° (Norges vassdrags- og energidirektorat, 2011; Bråthen et al., 2020). Both measurements from the field and the DEM slope calculations gave results that most of the investigated area generally exhibits slope inclination well below the threshold in which "normal" gravitational slope processes could occur (Olesen et al., 2000; Jibson, 2009; Norges vassdrags- og energidirektorat, 2011; Olesen et al., 2013; Mangerud et al., 2018).

In Chapter 5.3 – grain size analysis, the sieving values are presented in semi-logarithmic graphs. In addition, the D10, 30 and 60 values are marked, and two outer boundaries are plotted. These boundaries are based upon Hermanns & Niedermann (2011) plotting of grain size composition of soils likely to liquefy. They have condensed the results from the laboratory tests conducted by Lee & Fitton (1969) and 19 curves of sand that liquefied during earthquakes in Japan from Kishida (1970). This indicates the area in which sands and fines are most liquefiable. As mentioned in Chapter 3.3.3 and discussed in Hermanns & Niedermann (2011), sediment samples with large amounts of clay will not liquefy as easily as

samples with small amounts of clay. In sample 1.3.1 (Figure 43), all values were between the outer boundaries, making the soil likely to liquefy. In sample 1.1.1 (Figure 42), 1.2.1 (Figure 42), 2.3.2 (Figure 45), 2,1,3 (Figure 47), 2.2.3 (Figure 48), and 4.1.4 (Figure 50), most of the values were inside the outer boundaries of most likely values to liquefy. The samples provided by NGU are, as mentioned, hard to compare to both samples collected explicitly for this thesis and to the Hermanns & Niedermann boundaries due to the different sieving techniques and grain size fractions available. In sample 80775 (Figure 51), most of the values are outside the liquefaction boundary. This does not mean that the soil could not have liquefied but makes it less likely. The three other samples, 80776 (Figure 52), 80778 (Figure 53), and 80779 (Figure 54), most of the values are inside the boundaries, except the <500µ. A reason for this might be the lack of distinct fractions available. However, Hermanns & Niedermann (2011) use percentage by weight instead of percentage finer as done in this thesis. They do not specify what percentage by weight is based on, but from the literature on the sieving analysis and plotting (Chapter 3.2), the common weights to illustrate grain size distribution are either cumulative weight or percentage finer, both based upon the weight of the sample retained or passed. Therefore, it is fair to assume that percentage by weight is based upon one of these values. The two values present pretty much the same values but in reverse order and is, to some degree, interchangeable.

In Tabell 1, the total percentage of each sediment category is added together for each sample, making it easy to distinguish and compare the fractions of different sediment sizes. At the first location, 1.x.1, there is considerably more silt and clay in the host sample (1.1.1) and host and deposition sample (1.2.1) than it is in the deposition sample (1.3.1). It is also more in sample 1.1.1 than in 1.2.1. It is more gravel in 1.1.1 and 1.2.1 than in 1.3.1, while 1.3.1 has more sand (fine, medium, and coarse) than 1.1.1 and 1.2.1. This can result from liquefaction not being able to transport the biggest sediments, while the smallest sediments (clay and silt) are transported further and washed out more quickly than the sands. At location 2.x.3, the deposition material (2.1.3) has evidently more fine and medium sand than 2.2.3. It also has more clay and silt, but it is by under one percent. This can be a result of the sample not being representative or not being adequately split in preparation for the sieving process. The host material (2.2.3), on the other hand, has more coarse sand and gravel. These are the coarsest grained sediments measured in the samples. Subsequently, these sediments will be transported last, as they need more energy in the movement to be transported. The rest of the samples are hard to analyse, as only the host or deposition area was sampled. However, 2.3.2 (deposition

material) resembles that of 1.3.1 and 2.2.3 (deposition material) with high percentages of silt/clay and fine sand, medium percentages of medium sand, and low percentages of coarse sand and gravel. Sample 1.4.1 (host material) resembles that of 2.2.3 and 1.1.1 (host material). The only difference is a relatively low percentage of silt/clay. Again, this might be a result of the sample not being representative or not being adequately split during the sieving process.

The bedrock map (Figure 3) and soil composition map (Figure 4) also support the notion that the sediments sampled consist of large sand fractions. The bedrock mainly consists of sandstone, and the soil consists mostly of till material (glacial till deposition). As a result, it is evident that the sediment samples have significant fractions of sand. The ice sheet erodes the bedrock, picking up the bedrock material, transporting it is deposited as till or glacifluvial material. This is also supported by the simple test conducted during the fieldwork (see Chapter 4.2 and Chapter 5.1).

As a whole, most of the values of almost all samples are in between the two boundaries, and as Lee & Fitton writes,

> The strength of very fine sands was found to be less than half of the strength of the gravel. […] [A]t grain sizes within the silt and clay size range, the strength again increased, with the compacted clay being about three times stronger than the fine sand. (Lee & Fitton, 1969, p. 79)

The samples collected through the fieldwork did not go through the hydrometer process (a process where, in short, fines <75µ are suspended in water, and settling time is recorded (Geoengineer, 2014)). The distinction between silt and clay is thus not available in this study, but as mentioned in Chapter 5.1, simple silt/clay tests indicate large amounts of silt in the soil as the soil crunched between the teeth and cracked when rolled into a “snake” and bent. This indicates minor/limited amounts of clay. This means that criterion 5 in Jibson to some degree is met, as the landslides most certainly come due to liquefaction; however, no other liquefaction structures have been mapped or observed. There might have been sand volcanoes in the area that has been covered by vegetation or eroded by fluvial processes.

As presented in Chapter 3.2.2, Hakam (2016) and Chacrabortty et al. (2018) present at what D_{50} the soil is most likely to liquefy. The approximated D_{50} values of all samples analysed in this thesis are presented in the graphs in Chapter 5.3 and the tables in Chapter 9, Appendix 1. Hakam (2016) suggests D_{50} between 0.1125 – 0.3375 mm, and Chacrabortty et al. (2018)

suggest between 0.01 and 2 mm. All soils with a D_{50} value considered likely to liquefy by Hakam (2016) are within the range of soils considered liquefiable by Chacrabortty et al. (2018). Of the samples, only sample 80775 did not fall into either D_{50} intervals. All other samples fell into the interval presented by Chacrabortty et al. (2018), but only two samples (2.3.2 and 2.1.3) fell between the interval presented by Hakam (2016). Only sample 80776 were close to the average particle diameter likely to liquefy (Chacrabortty et al., 2018)

The results presented above also meets the sixth criterion Jibson presents, that the landslide distribution cannot be explained solely based on "normal" slope processes. The slope inclination is too gentle for glacial till material, rich in sand and silt, to slide due to gravitational processes (Palmu et al., 2015; Ojala et al., 2019). Criterion (4) was a large number of landslides, evident from the mapping in GIS (Olesen et al., 2000; Jibson, 2009; Norges vassdrags- og energidirektorat, 2011; Olesen et al., 2013; Smith et al., 2014). A large number of landslide scars encompass the surface of the area. As illustrated in Figure 57(a), the landslide scars are also distributed throughout the slope, not only at the base, as most storm-induced landslides are.

The last two criteria presented are "(1) ongoing seismicity in the region, which has triggered landslides; (2) coincidence of landslide distribution with an active fault or seismic zone" (Jibson, 2009, p.

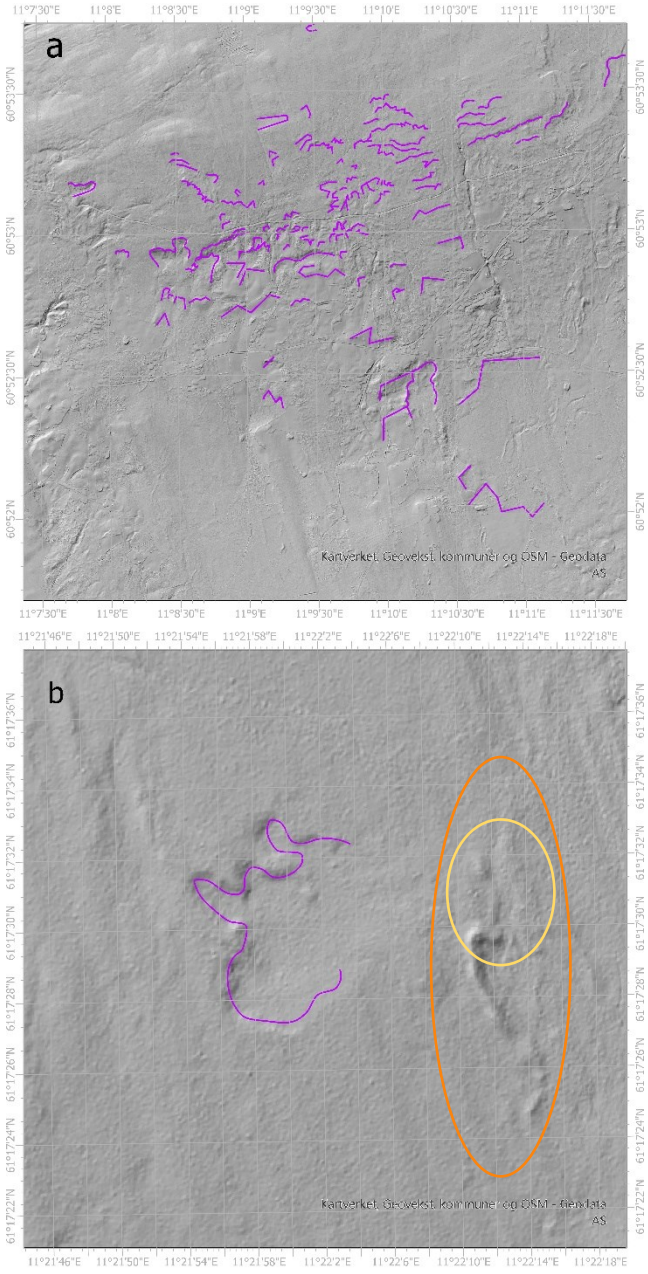

Figure 57 Illustration of where sliding has cut off landforms and cluster of sliding incidences. a) illustrates an area where sliding incidences are especially clustered together and not only at the base of the slope as per criterion (4) in Jibson (2009) and Jibson (2009) in general. At closer inspection it appears as if the landslide scars cuts drumlins, implying that landslide activity happened after the deglaciation b) shows where the landslide deposit partly overlays what looks like an esker meaning the sliding has happened after the ice cover melted away (Orange circle esker as a whole. Yellow circle where the esker is cut of)

567). On the website https://www.jordskjelv.no/finn-jordskjelv/ and in Figure 18, the seismic activity in Norway is recorded. In the area surrounding Brumunddalen there are two seismic events in the last three years recorded at jordskjelv.no, but not strong enough to trigger sliding. Criteria 1 and 2 in Jibson are partly met but not evident enough to be evidence of PGS induced landsliding in the area. It can however be strengthened by the other criteria.

Jibson (2009) has found that the morphology of some landslides strongly suggests seismically triggered landsliding. An example presented in Jibson (2009) is that landslide incidents in low-angle shear surfaces appear much more frequently as a result of seismic shaking than due to other influences. It becomes evident that the area investigated meets this criterion from the measurements conducted during the fieldwork and the slope inclination analysis conducted in GIS, as mentioned in Chapter 5.1 and Chapter 5.2.2. However, he points out that the landslides induced by earthquakes usually present a relatively limited and blocky deposition area compared to precipitation induced sliding. Rain-induced sliding often presents a more widespread deposition area that can be hard to define. As with most visual indicators of a phenomenon, this criterion is not definite but can back up claims of seismically induced landslides. The deposition areas of the slides mapped are not particularly limited or blocky. However, as the landsliding occurred many thousand years ago, the deposition area might have been eroded or covered by vegetation.

Mangerud et al. (2018) found, as previously mentioned, a suggested PGs induced landslide in Hemma, near the investigated area in this thesis (Figure 30). They contacted several experienced geologists in regards to the proposed landslide. The landslide had happened in till, in a slope that was approximately 4°, only 2° less than the general slope inclination measured in this research. The deposition area of the landslide was around 2.6°. The geologists involved in their research had never seen landslides of till material on such gentle slopes.

Additionally, through radiocarbon dating, they placed the sliding incident to about 4000 years after the area became ice-free (6500 BP) and a pine forest was established. These factors made them rule out the possibility of sliding due to unstable soil conditions after the last deglaciation (Mangerud et al., 2018). The landslide mapped and investigated in this article was mapped by Ola Fredin (NGU/NTNU) and Marie Keding (NGU/GEUS) as part of the initial mapping of the study area investigated in this thesis. Mangerud et al. (2018) suggest

that the soil had to be water-saturated for sliding to occur in such gentle sloping, and a triggering mechanism must have activated the process. Mangerud et al. (2018) present earthquake activity leading to liquefaction as the only feasible mechanism. Ola Fredin and Marie Keding suggest that seismic activity, as a result of PGU, as presented in studies from Finland and Sweden, is the cause for the rest of the landslides in the area as well (Olesen et al., 2000; Olesen et al., 2003; Lagerbäck & Sundh, 2008; Olesen et al., 2013; Smith et al., 2014; Sutinen et al., 2014; Mikko et al., 2015; Palmu et al., 2015; Mangerud et al., 2018). Due to the close proximity of the Hemma landslide and the Brumunddalen area, the slides have likely happened around the same time. In Figure 57 (b), it looks as a landslide deposit partly overlays what looks like an esker, and in Figure 57 (a), it looks as though the landslide scars cuts of drumlines, meaning the sliding happened after the ice cover melted away. This, in addition to the dating conducted by Mangerud et al. (2018), would act as an argument for placing the sliding incidents after the Fennoscandian deglaciation and further strengthen the case that PGS was a triggering factor. Therefore, the study area would, as the Hemma site, have been inhabited by the pine forest observed during the fieldwork, and sliding due to the "normal" gravitational slope process becomes even less likely. This also strengthens the third criterion presented by Jibson (2009), as the slopes become more stable when roots from vegetation penetrate the ground, as the roots act as an armoury in the soil.

Mangerud et al. (2018) conclude that the landslide was triggered by an earthquake with a maximum age of 6400 cal years BP. If an earthquake was the cause of the landslide in Hemma, chances are that the same earthquake has influenced the study area due to the two localities' proximity. Smith et al. (2014) investigated four landslides in proximity to faults in the Bollnäs area in Sweden. The topography is pretty similar to the Brumunddalen area with a gentle inclination and till as the dominating soil type. Smith et al. (2014), similarly to Mangerud et al. (2018), consider sliding in slopes with gentle inclination to be proof of earthquakes as the triggering mechanism (Smith et al., 2014). However, they dated the incidents to around 10180 - 9500 cal years BP, placing the incidents to a time right after the deglaciation and before the Hemma sliding in Mangerud et al. (2018). Sutinen et al. (2014) dated many landslides and faults in northern Finland. Through the dating, they concluded that the seismicity as a result of GIA and uplift continued after the initial major seismic event. The slides dated by Sutinen et al. (2014) have been dated to between 9730 cal yr BP and 5055 cal yr BP, clustering in 2-3 groups a couple of thousand years apart. One interpretation of the dataset of Sutinen et al. (2014) is that there were several episodes of enhanced seismic activity

following the last deglaciation. The proposed dates of the sliding incidents' in Norway, Sweden, and Finland are all in and around the same time, suggesting that isostatic adjustment could have had something to do with the sliding.

Palmu et al. (2015) are among the researchers that have mapped large parts of Finland to look at PG faults and landslides induced by seismicity. They mapped the landforms by using a LiDAR-derived DEM to screen the area for landforms. The landslide presented in Figure 58 is from Palmu et al.'s article. The landslide scars in the article resemble those mapped and presented in Figure 30 and Figure 38, indicating that similar processes have played a role in triggering the sliding. Several researchers have continued mapping faults and landslides in Finland since the mapping initially started. Ojala et al. (2019) have recently published an article investigating the distribution and morphology of paleoseismic landslides. Both Ojala et al. (2019) and Palmu et al. (2015) investigate landslides in relation to PG faults, but they are nevertheless interesting to look at as seismically induced landslides behave more or less the same. Ojala et al. (2019) have found that the paleoseismic landslides usually "cluster in groups of 3-10 landslides that sometimes occur in linear groups" (Ojala et al., 2019). This has to some degree also happened in Brumunddalen, evident from the mapping presented in Chapter 5.2.1.

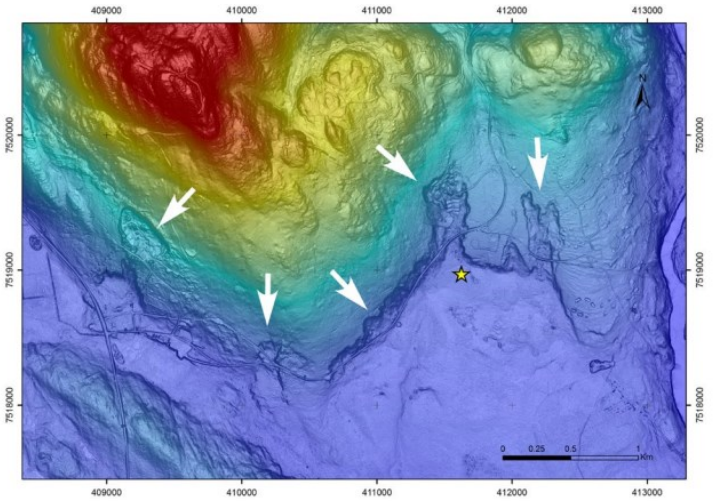

Figure 58 Landslides mapped by Palmu et al. (2015). The white arrows point at the landslide scars, and the yellow star indicates the drilling location. The blue area is the lowest rising surface at 181 masl. while the red is highest rising 531 masl. (From Palmu et al., 2015)

Ojala et al. (2019), in line with the other studies presented in this chapter, found that the general slope inclination in the area where landslides were mapped was far lower than that calculated for "normal" gravitational slope processes, with an average of 4.4°. They have also found that sand dominated tills do not experience mass movement in gentle sloping under "normal" slope conditions and point out that earthquakes, triggering liquefaction, typically are related to these landslides (Ojala et al., 2019).

Lagerbäck & Sundh (2008) has investigated faulting and landsliding in large parts of Sweden. They have found a causal relationship between the last deglaciation and the faulting mapped in northern Sweden. They have also found that the landslide scars present in the area around the fault most probably have been triggered by the seismicity caused by the GIA and faulting. This shaking has caused the soil to liquefy, and large amounts of mass have been moved. They postulate earthquakes at around M 7-8 in the north but far more gentle in the south and central Sweden. The areas investigated by Lagerbäck & Sundh are dominated by sandy glacial till which is considered to be stable in gently sloping terrain. Landslides, due to "normal" gravitational slope processes, would not be expected in these conditions, in line with the arguments presented by Olesen et al. (2000), Jibson (2009), Olesen et al. (2013), Smith et al. (2014), Sutinen et al. (2014), Palmu et al. (2015), Mangerud et al. (2018), and Ojala et al. (2019). The most probable mechanism creating these landslide scars is therefore believed to be seismically induced liquefaction. The area investigated in this research is, as seen from Chapter 5.2.2, Chapter 5.3, Chapter 2.1, and Chapter 2.2, similar to those investigated in Lagerbäck & Sundh (2008) in that the terrain slope is quite gentle, the sediment samples have a significant fraction of fine to coarse sand, and the surface material is mostly glacial till or glacifluvial material.

The area around Brumunddalen, in contrast to Lagerbäck & Sundh (2008), does not show signs of faulting, although crustal movement (faulting) might have occurred along what today is rivers or valleys (Brumunddalselva) (Personal communication O.Fredin, 2021). However, Lagerbäck & Sundh (2008) use the large number and proximity of earthquakes in the regions to indicate PGS in Sweden. It is also used as an argument for PGS in Smith et al. (2014) and Mikko et al. (2015). This coincides with the mapped features in Chapter 5.2.1 and can pose as an argument for PGS triggered landsliding in the Brumunddalen area.

Smith et al. (2014) and Mikko et al. (2015) continued mapping PG faults and landslides in Sweden. They have mapped landslides and faults in Sweden using LiDAR data instead of aerial photography with great success. The previous work has mostly focused on the northern parts of Sweden, but through LiDAR data, they have found signs of paleoseismic landforms in southern and central Sweden as well. Smith et al. (2014) point out that most of the slides, if present before deglaciation, would be buried by deposition. A 5 m high scarp would be buried entirely within eight years. With these calculations, most, if not all, landslide scars in Brumunddalen would not be visible if present before the deglaciation. In line with most other

researchers, Smith et al. (2014) and Mikko et al. (2015) conclude that the factor of safety (stability of the surface), number of landslide scars, and radiocarbon dating is sufficient evidence that strongly indicates paleoseismic processes.

Uzuoka et al. (2005) mapped and investigated several liquefaction-, rockfall- and landslide incidences, including small slope failures triggered by earthquakes in the Tohoku area in Honshu Island, Japan - 2003. In some places, sand broils (Small sand "volcanoes") were observed in relation to the liquefaction events. This has not been observed or mapped in Brumunddalen. However, some sand broil like features (Figure 59) was observed in the LiDAR dataset, but through conversation with supervisor Ola Fredin, it became clear that these probably were signs of archaeological earth ovens.

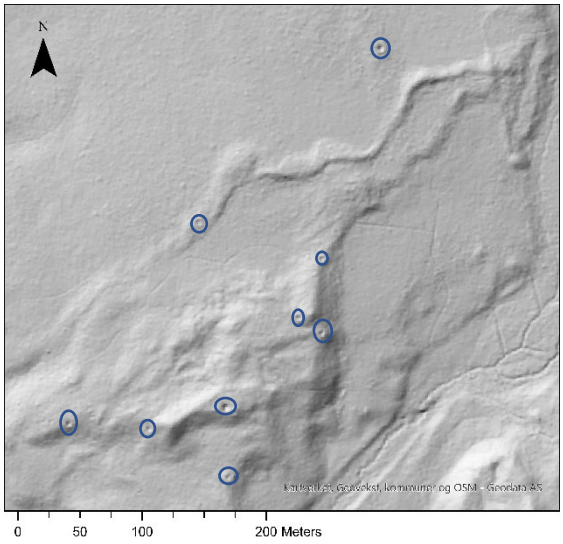

Figure 59 Suspected earth ovens in the Brumunddalen area. Circles mark where earth ovens are present

Two landslides were analysed in the Uzuoka et al. (2005) article, here mentioned as U1 (Dateshita) and U2 (Nishisaruta). The slope inclination at U2 was around 7°, and even though the slope was steeper at U1, it was still less than 30°. The inclination of the slope at the two events coincides with the previously mentioned slides in Scandinavia and the general slope inclination needed for "normal" slope processes (Chapter 3.3.4). Therefore, the only viable explanation for slope failure in the two locations was liquefaction.

In Tabell 1, the values retrieved from each sieve are presented in relation to the Wentworth sediment classification. The general trend for the samples in this thesis is that they consist of 17.66% silt and clay, 64.24% sand, and 18.10% gravel. At U1, the general distribution from the ten sampling locations was: clay 10%, silt 20%, sand 50%, and gravel 20%. At U2, the general distribution from ten samples was: clay 20%, silt 15%, sand 55%, and gravel 10%. Subsequently, the grain size distribution of the samples analysed in this thesis and the grain size observed in Uzuoka et al. (2005) is, to some degree, comparable. The composition of the clay and silt fraction is uncertain, but it is adjacent to think that it consists of relatively more silt than clay, as sandstone is the main component of the bedrock (Figure 3), and the surficial

deposits primarily consist of morain material and glacifluvial deposition. Therefore, the samples collected throughout this thesis are likely to liquefy if exposed to seismic shaking.

As previously mentioned, it is difficult to determine with certainty if seismic shaking is the pivotal factor in triggering a landslide, based on the criteria presented above. However, if enough criteria are met, earthquakes can be proposed as the most likely triggering mechanism (Jibson, 2009). Many of the criteria indicating seismically triggered landslide activity presented in Jibson (2009) are more or less met for the investigated area in south-central Norway. The landslide activity discussed in this paper can therefore be placed into the landslide categorisation presented by Wood (1993), Dehls et al. (2000), Olesen et al. (2003; 2013), and Palmu et al. (2015) as class B) *Probably neotectonics*. The classification grade landslide occurrences, suspected to be triggered by PGS, into five classes: "(A) almost certainly neotectonics, (B) probably neotectonics, (C) possibly neotectonics, (D) probably not neotectonics and (E) very unlikely to be neotectonics" (Wood, 1993; Dehls et al., 2000, p. 2; Olesen et al., 2003, p. 5; Olesen et al., 2013, p. 148; Palmu et al., 2015, p. 3). The classification system was developed to grade different neotectonic claimes based on the research and information available. Wood (1993) points out that grading claims into classes are based on the judgment of a set of predefined criteria. Palmu et al. (2015) further recognise that even though the grading is widely recognised as a tool to distinguish landforms triggered by PGS from other processes, it is fairly subjective. However, the landslides in this thesis are perceived to fit best into category B), as most of the research conducted indicates that "normal" gravitational slope processes would not have triggered landsliding in this terrain. The landslides can not be classified as grade A), as further research, for instance, more thorough laboratory testing, dating, and coring is advised.

Chapter 7 Limitations And Future Work

As disclosed throughout the thesis, several sides of determining landsliding triggered by PGS were beyond the scope, time, and budget of this master's thesis. Therefore, this chapter will propose some future work beneficial for determining the likelihood of PGS triggered landsliding.

In general, the research on isostatic adjustment as a driving force behind general stress-related failure in Fennoscandia is not conclusive. Some researchers claim tectonic activity, such as stress build-up from ridge-push, as the driving force of seismic activity in Scandinavia. Nonetheless, isostatic adjustment is considered to affect the seismicity through activating old tectonic faults, but the extent of its impact is discussed. Research to determine the driving force of seismic activity in Scandinavia would benefit the study of PGS triggered landsliding. More specifically, for this research, modelling of the GIA for the area, laboratory testing of the soil's mechanical properties, more extensive sediment sampling, modelling of liquefaction and failure, and dating of the incidents would be beneficial.

More extensive sediment sampling and cross-sections of the surface, such as presented in other PGS studies from Norway, Sweden, and Finland, would be beneficial. These samples should be tested for shear strength and other mechanical properties apart from grain size distribution. Moreover, sampling at depth, through core drilling or digging, would be valuable to see if there are soil layers with lower strength at a depth that could cause landsliding. Slope stability modelling would be beneficial to rule out the possibility of “normal” gravitational slope processes and to determine at what magnitude seismic activity could cause surface failure. Further, sampling and cross-sections can be used as an opportunity to date the landslide incidents, for instance, using radiocarbon analysis and characteristics of weathering profiles that develop in the sediment or become preserved by burial beneath younger sediments. The cross-section can also say something about how the sediments change from above the landslide down to the deposition. If the sediments, such as silt and clay, are divided into distinct layers above the landslide and are folded or mixed below, landsliding is most likely the cause.

Chapter 8 Conclusion

The goal of this research was to get closer to an answer to the hypothesis “most or all of the landslide scars in Brumunddalen were derived through landslides triggered by post-glacial seismicity (earthquakes). The hypothesis is broad and challenging to answer. Therefore, four subordinate questions were posed: 1. Is the terrain in the area surrounding Brumunddalen steep enough for “normal” gravitational landslide processes to occur, or is post-glacial seismicity a more likely mechanism? 2. Can the landslides be tied to the time after the last glacial maximum and deglaciation of the Fennoscandian ice sheet? 3. Is the grain size distribution of the sediment samples from Brumunddalen distributed in a way that liquefaction of the soil due to an earthquake could have occurred? 4. Does the area around Brumunddalen resemble other Scandinavian areas susceptible to post-glacially induced earthquakes?

In addition to a literature review, three main methods were used to get closer to a definite answer to the hypothesis and the subordinate research questions. GIS was used to map the area and analyse the slope inclination and mass movement. Fieldwork was conducted to collect sediment samples, measure slopes, and observe the area. Finally, the sediment samples were dry sieved, plotted, and analysed to get information on the composition of the soil. The theory was used to understand the prerequisite for PGS and liquefaction and the underlying processes. Finally, literature from similar studies in Norway, Sweden, Finland, and Japan has been used to strengthen arguments made for and results derived from this research. Based on the methods conducted throughout this thesis, the concluding remarks are as follows:

The mapping conducted was started by Ola Fredin and Maria Keiding and continued throughout this thesis. The suspected landslide scars mapped by Fredin and Keideng and specifically for this thesis were cross-validated and merged to create one single dataset showing landslide scars in the area. This mapping uncovered a large number of landslide scars in the Brumunddalen area.

The investigated area is mainly covered by glacial till and, to some degree, glaciofluvial material. The underlying bedrock is dominated by sandstone, resulting in a sandy-silty dominated overlying glacial till. The GIS analysis further shows a relatively gentle slope in the area, with an average slope angle of 6°. The gentle slopes and clustering of landslides in the investigated area resemble similar studies in Norway, Sweden, Finland, and Japan, where seismicity was shown to trigger landslides.

The grain size distribution analysis disclosed that most samples were well graded, and the D50 value of all samples, except one, were within the boundaries of likely to liquefy. Most of the samples, plotted in logarithmic graphs, were also within a proposed boundary for likely to liquefy. Similar areas studied in Norway, Sweden, and Finland have found that glacial till, with similar structure and origin, is likely to liquefy due to seismic shaking. Soils in Japan, with similar fractions of fines, sand, and gravel, together with a gentle slope incline, was also liquefied due to seismic activity.

Studies from Finland, Sweden, and Norway placed the mapped faults and landslides after the Fennoscandian deglaciation, and one study proposed several seismic pulses between approximately 10 ka – 5 ka BP. Dating the landslides in the study area is beyond the scope of this study. However, the Hemma study is particularly interesting due to the proximity to the study area. One study also found that if the sliding incidents did not happen after the last deglaciation, no signs of sliding would be present in the scenery, as glacial eroding and deposition would cover them. In this study, mapped landslides and deposition cuts drumlins and covers a glacial esker, proving sliding after the deglaciation.

Several of the studies look to Crozier's six criteria to determine the seismic triggering of landslides. Three of the six criteria are fulfilled through the research carried out in this research, and three of six are to varying degrees met. The more of these that are met, the more likely a soil is to liquefy due to PGS. However, non seismic processes can potentially trigger all landslides, and the results are therefore tentative.

Throughout the research conducted, the subordinate research questions have to some degree been answered. The studied area is not steep enough for “normal” gravitational slope processes to occur, although a slope stability model could be beneficial in further research. No dating has been done specifically for this research or for the landslides investigated. Going forward, this would be beneficial in determining the origin of the slides. However, studies of similar areas in Scandinavia, specifically the Hemma landslide, has dated the events to after the deglaciation of Fennoscandia. In addition, drumlins are cut, and an esker has been buried by landslide deposits, indicating sliding after deglaciation. As seen from the grain size distribution and composition of the soil, it can liquefy. Therefore, the assumption that ***most or all of the landslide scars in Brumunddalen were derived through landslides triggered by post-glacial seismicity (earthquakes)*** is strengthened, and the landslides are tentatively graded as *B) Probably neotectonics*, but further research is required.

References

Andersen, B. G., Mangerud, J., Sørensen, R., Reite, A., Sveian, H., Thoresen, M., & Bergström, B. (1995). Younger Dryas ice-marginal deposits in Norway. *Quaternary International*, *28*, 147–169. https://doi.org/10.1016/1040-6182(95)00037-j

Aronoff, S. (2005). *Remote sensing for GIS managers.* ESRI Press.

Aronoff, S. & Petrie, G. (2005). Active sensors: Radar and lidar. In the book: Aronoff, S (red.), *Remote sensing for GIS managers* (p.197 - 244). ESRI Press.

ASPRS. (2013). Las specification. Version 1.4-R13, *Open Geospatial consortium*. https://www.ogc.org/standards/LAS

Bayley, T. C., (2013). A review of statistical spatial analysis in geographical information system. In S. Fotheringham & P. Rogerson (Ed.), *Spatial analysis and GIS* (pp, 13-36). CRC press

Bråthen, M., Lyshaug, S., & Nashoug, O. (2020). *Skogkurs veileder Geologi og vegbygging*. https://www.skogkurs.no/userfiles/files/skogsveier/Veileder%20geologi%20og%20veibygging.pdf

Bungum, H., Olesen, O., Pascal, C., Gibbons, S., Lindholm, C., & VestOl, O. (2010). To what extent is the present seismicity of Norway driven by post-glacial rebound*? Journal of the Geological Society*, 167(2), 373–384. doi:10.1144/0016-76492009-009

Burrough, P. A. (1986). *Principles of geographical information systems for land resources assessment* (Vol. 12, pp. XIII, 194, pl.). Clarendon Press.

Carrier, W. D. (2003). Particle Size Distribution of Lunar Soil. *Journal of Geotechnical and Geoenvironmental Engineering*, *129*(10), 956–959. https://doi.org/10.1061/(asce)1090-0241(2003)129:10(956)

Chakrabortty, P., Das, A. & Anil. (2018, December 14). *Effect of Soil Grain Size on Liquefaction Strength of Sandy Soil*. ResearchGate. https://www.researchgate.net/publication/330514872_Effect_of_Soil_Grain_Size_on_Liquefaction_Strength_of_Sandy_Soil

Chandler, B. M. P., Lovell, H., Boston, C. M., Lukas, S., Barr, I. D., Benediktsson, Í. Ö., Benn, D. I., Clark, C. D., Darvill, C. M., Evans, D. J. A., Ewertowski, M. W., Loibl, D., Margold, M., Otto, J.-C., Roberts, D. H., Stokes, C. R., Storrar, R. D., & Stroeven, A. P. (2018). Glacial geomorphological mapping: A review of approaches and frameworks for best practice. *Earth-Science Reviews*, *185*, 806–846. https://doi.org/10.1016/j.earscirev.2018.07.015

CHARIM. (2021). *3.2 Digital Elevation Models | CHARIM*. Charim.net. http://charim.net/datamanagement/32

Christensen, A. (2016, July 1). *Ny nasjonal høydemodell*. Forskning.no. https://forskning.no/arkeologi-kulturhistorie-informasjonsteknologi/ny-nasjonal-hoydemodell/410538

Cope, M. & Elwood, S. (2009). Introduction. In M. Cope & S. Elwood (Ed.), *Qualitative GIS: a mixed methods approach* (pp. 1-12). Sage

Das, B. M. (2005). *Fundamentals of geotechnical engineering* (2nd ed., pp. XVI, 566). Thomson.

Dehls, J. F., Olesen, O., Olsen, L., & Harald Blikra, L. (2000*).* Neotectonic faulting in northern Norway; the Stuoragurra and Nordmannvikdalen postglacial faults. *Quaternary Science Reviews, 19*(14-15), 1447–1460. https://doi.org/10.1016/s0277-3791(00)00073-1

Department of transportation: New York. (2015). *TEST METHOD FOR THE GRAIN-SIZE ANALYSIS OF GRANULAR SOIL MATERIALS GEOTECHNICAL TEST METHOD*

GTM-20. https://www.dot.ny.gov/divisions/engineering/technical-services/technical-services-repository/GTM-20b.pdf
Earl, S., & Vancouver Island university. (2019, December 3). 9.4: *Isostasy*. Geosciences LibreTexts. https://geo.libretexts.org/Bookshelves/Geology/Book%3A_Physical_Geology_(Earle)/09%3A_Earths_Interior/9.04%3A_Isostasy
Esri. (2011). *How Slope works—ArcGIS Pro | Documentation*. Arcgis.com. https://pro.arcgis.com/en/pro-app/latest/tool-reference/spatial-analyst/how-slope-works.htm
Esri. (2016). *How Kriging works—Help | ArcGIS for Desktop*. Arcgis.com. https://desktop.arcgis.com/en/arcmap/10.3/tools/3d-analyst-toolbox/how-kriging-works.htm
Esri. (2020). *How Average Nearest Neighbor works—ArcMap | Documentation*. Arcgis.com. https://desktop.arcgis.com/en/arcmap/latest/tools/spatial-statistics-toolbox/h-how-average-nearest-neighbor-distance-spatial-st.htm
Esri. (2021a). *Clip (Analysis)—ArcGIS Pro | Documentation*. Arcgis.com. https://pro.arcgis.com/en/pro-app/latest/tool-reference/analysis/clip.htm
Esri. (2021b). *Clip Raster (Data Management)—ArcGIS Pro | Documentation*. Arcgis.com. https://pro.arcgis.com/en/pro-app/latest/tool-reference/data-management/clip.htm
Esri. (2021c). *Define feature class properties—ArcGIS Pro | Documentation*. Arcgis.com. https://pro.arcgis.com/en/pro-app/latest/help/data/feature-classes/defining-feature-class-properties.htm
Esri. (2021d). *Feature classes—ArcGIS Pro | Documentation*. Arcgis.com. https://pro.arcgis.com/en/pro-app/latest/help/data/feature-classes/feature-classes.htm
Esri. (2021e). *Frequently asked questions—ArcGIS Pro | Documentation*. Arcgis.com. https://pro.arcgis.com/en/pro-app/latest/get-started/faq.htm#anchor45
Esri. (2021f). *How Cut Fill Works ArcGIS Por | Documentation.* Arcgis.com. https://pro.arcgis.com/en/pro-app/latest/tool-reference/spatial-analyst/how-cut-fill-works.htm
Esri. (2021g). *How Hillshade works – ArcGIS Pro | Documentation*. Arcgis.com. https://pro.arcgis.com/en/pro-app/latest/tool-reference/spatial-analyst/how-hillshade-works.htm
Esri. (2021h). *Mosaic To New Raster (Data Management) | Documentation*. ArcGIS Pro. https://pro.arcgis.com/en/pro-app/latest/tool-reference/data-management/mosaic-to-new-raster.htm
Esri. (2021i). *Slope function—ArcGIS Pro | Documentation*. Arcgis.com. https://pro.arcgis.com/en/pro-app/latest/help/analysis/raster-functions/slope-function.htm
Evans, D. J. A., & Benn, D. I. (2004). *A Practical guide to the study of glacial sediments* (p. XIII, 266, 8 pl.). Arnold.
Follestad, B., Fredin, O., Olsen, L., & Reimann, C. (2013). Distribution of rock fragments, grain size and chemical elements in tills in the Lake Mjøsa area, East Norway. *Norges Geologiske Undersøkelse Bulletin*, *453*, 1–11. https://www.ngu.no/upload/Publikasjoner/Bulletin/Bulletin453_1-11.pdf
Fonstad, M. A., Dietrich, J. T., Courville, B. C., Jensen, J. L., & Carbonneau, P. E. (2013). Topographic structure from motion: a new development in photogrammetric measurement. *Earth Surface Processes and Landforms*, *38*(4), 421–430. https://doi.org/10.1002/esp.3366

Fredlund, M. D., Fredlund, D. G., & Wilson, G. W. (2000). An equation to represent grain-size distribution. *Canadian Geotechnical Journal = Revue Canadienne de Géotechnique*, *37*(4), 817–827. https://doi.org/10.1139/t00-015

Geoengineer. (2014). *Step-by-Step Guide for Grain Size Analysis*. Geoengineer.org. https://www.geoengineer.org/education/laboratory-testing/step-by-step-guide-for-grain-size-analysis

Geowizzard. (2021). *ThiessenPolygons*. Ian-Ko.com. https://www.ian-ko.com/ET_GeoWizards/ETGW12UG_WEB/etgw/thiessenPolygons.htm

Gisgeography. (2020, 24. December). *How to mosaic raster datasets*. https://gisgeography.com/mosaic-raster/

Gregersen, S. (2006). Intraplate earthquakes in Scandinavia and Greenland Neotectonics or post-glacial uplift. *J. Ind. Geophys. Union*, *10*(1), 25–30. http://iguonline.in/journal/Archives/10-1/3.pdf

Hakam, A. (2016). Laboratory Liquefaction Test of Sand Based on Grain Size and Relative Density. *Journal of Engineering and Technological Sciences, 48*, 334-344.

Hansen, L., Høgaas, F., Rindstad, B. I., Sveian, H., & Olsen, L. (2012). *GEOLOGI FOR SAMFUNNET GEOLOGY FOR SOCIETY NGU Norges geologiske undersøkelse Geological Survey of Norway Database for registrering av marin grense (MG) i Norge*. https://www.ngu.no/upload/Publikasjoner/Rapporter/2012/2012_063.pdf

Harvey, K. R. & Hill, G. J. E. (2001). Vegetation mapping of a tropical freshwater swamp in the Northern Territory, Australia: A comparison of aerial photography, Landsat TM and SPOT satellite imagery, *International Journal of Remote Sensing*, 22:15, 2911-2925

Hermanns, R.L. & Niedermann, S. (2011). Late Pleistocene–early Holocene paleoseismicity deduced from lake sediment deformation and coeval landsliding in the Calchaquíes valleys, NW Argentina, in Audemard M., F.A., Michetti, A.M., and McCalpin, J.P., eds., Geological Criteria for Evaluating Seismicity Revisited: Forty Years of Paleoseismic Investigations and the Natural Record of Past Earthquakes: *Geological Society of America Special Paper 479,* p. 181–194, doi:10.1130/2011.2479(08).

Holger, S. & Wu, P. (2011). Glacial isostatic adjustment in Fennoscandia—A review of data and modeling. *Journal of Geodynamics*, *52*(3–4), 169–204. https://doi.org/10.1016/j.jog.2011.03.002

Hughes, A. L.C., Clark, C. D. & Jordan C. J. (2010). Subglacial bedforms of the last British Ice Sheet, *Journal of Maps*, (6:1), 543-563, https://doi.org/10.4113/jom.2010.1111

Jibson, R. W. (2009). Chapter 8 Using Landslides for Paleoseismic Analysis. *In International geophysics series : a series of monographs* (Vol. 95, pp. 565–601). Academic Press. https://doi.org/10.1016/S0074-6142(09)95008-2

Kartverket. (2020a, September 18). *Kva Kartverket gjer*. Kartverket.no. https://kartverket.no/om-kartverket/kva-kartverket-gjer

Kartverket. (2020b, November 24). *Høydedata og dybdedata*. Kartverket.no. https://kartverket.no/api-og-data/terrengdata

Kunnskapsdepartementet (2020). *Grunnleggende ferdigheter - overordnet del av læreplanverket*. Udir.no. https://www.udir.no/lk20/overordnet-del/prinsipper-for-laring-utvikling-og-danning/grunnleggende-ferdigheter/

Keiding, M., Olesen, O.& Dehls, J. (2018). *Neotectonic map of Norway and adjacent areas. Geological Survey of Norway.* https://www.ngu.no/upload/Publikasjoner/Kart/Neotectonic_Map_NGU.pdf

Konert, M. & Vandenberghe, J. (1997). Comparison of laser grain size analysis with pipette and sieve analysis: a solution for the underestimation of the clay

fraction. *Sedimentology*, *44*(3), 523–535. https://doi.org/10.1046/j.1365-3091.1997.d01-38.x
Krom, M. D. (2012). Earth geology and tectonics. In J. Holden (Red.), *An introduction to physical geography and environment* (3. Edition., pp. 27-50). Pearson education limited
Lagerbäck, R. & Sundh, M. (2008). *Early Holocene faulting and paleoseismicity in northern Sweden*. Sveriges geologiska undersöking (SGU) Geological survey of Sweden. http://resource.sgu.se/produkter/c/c836-rapport.pdf
Lang, M. W. & McCarty, G. W. Lidar intensity for improved detection of inundation below the forest canopy. *Wetlands 29*, 1166–1178 (2009). https://doi.org/10.1672/08-197.1
Lee, E. M. & Jones, D. K. C. (2004). *Landslide risk assessment* (pp. X, 454). Thomas Telford.
Lee, K.L., & Fitton, J.A. (1969). Factors Affecting the Cyclic Loading Strength of Soil. In Selig, E. & Hampton, D. (Eds.), *STP450-EB Vibration Effects of Earthquakes on Soils and Foundations* (pp. 71-95). https://doi.org/10.1520/STP33637S
Liu, X. (2008). Airborne LiDAR for DEM generation: some critical issues. *Progress in Physical Geography: Earth and Environment*, *32*(1), 31–49. https://doi.org/10.1177/0309133308089496
Longley, P. A., Goodchild, M. F., Maguire, D. J. & Rhind, D. W. (2015), *Geographic information science and systems* (4. edition). John Wiley & sons.
Lukas, K. & Weibel, R. (1995, September). Assessment and improvement of methods for analytical hillshading. In *Proceedings of the 17th International Cartographic Conference* (pp. 2231-2240).
Mallet, C. & Bretar, F. (2009). Full-waveform topographic lidar: State-of-the-art. *ISPRS Journal of Photogrammetry and Remote Sensing*, *64*(1), 1–16. https://doi.org/10.1016/j.isprsjprs.2008.09.007
Mangerud, J., Birks, H. H., Halvorsen, L. S., Hughes, A. L. C., Nashoug, O., Nystuen, J. P., Paus, A., Sørensen, R. & Svendsen, J. I. (2018). The timing of deglaciation and sequence of pioneer vegetation at Ringsaker, eastern Norway – and an earthquake-triggered landslide. *Norwegian Journal of Geology* (*98)*, pp. 301–318. https://dx.doi.org/10.17850/njg98-3-03.
Michez, A., Bauwens, S., Bonnet, S. & Lejeune, P. (2016). Characterization of Forests with LiDAR Technology. *Land Surface Remote Sensing in Agriculture and Forest*, 331–362. https://doi.org/10.1016/b978-1-78548-103-1.50008-x
Mikko, M., Smith, C. A., Lund, B., Ask, M. V. S. & Munier, R. (2015) LiDAR-derived inventory of post-glacial fault scarps in Sweden, *GFF*, 137:4, 334-338, DOI: 10.1080/11035897.2015.1036360
Mitchell, J. K. & Soga, K. (2005). *Fundamentals of soil behaviour* (Vol. 3). New York: John Wiley & Sons.
MSDI. (2021, January 10). *LiDAR Mapping | MSDI | High Accuracy Drone Survey Services*. MSDI. https://www.msdi.co.id/services/lidar-mapping/
Mulargia, F., Castellaro, S. & Ciccotti, M. (2004). Earthquakes as three stage processes. *Geophysical Journal International*, *158*(1), 98–108. https://doi.org/10.1111/j.1365-246x.2004.02262.x
Mörner, N.-A. (2015) Glacial Isostasy: Regional—Not Global. *International Journal of Geosciences*, 6, 577-592. http://dx.doi.org/10.4236/ijg.2015.66045
Norges vassdrags- og energidirektorat. (2011). *Retningslinjer Flaum-og skredfare i arealplanar*. http://publikasjoner.nve.no/retningslinjer/2011/retningslinjer2011_02.pdf
NRC. (1985). *Liquefaction of Soils During Earthquakes*, National Research Council, National Academy Press, Washington, DC. https://doi.org/10.17226/19275

Nystuen, J. P. (1982). Late Proterozoic basin evolution on the Baltoscandian craton: the Hedmark Groups, Southern Norway., *NGU 375, 1 - 74*

Obermeier, S. F. (1996). Use of liquefaction-induced features for paleoseismic analysis — An overview of how seismic liquefaction features can be distinguished from other features and how their regional distribution and properties of source sediment can be used to infer the location and strength of Holocene paleo-earthquakes. *Engineering Geology*, *44*(1-4), 1–76. https://doi.org/10.1016/s0013-7952(96)00040-3

Occhietti, S., Parent, M., Lajeunesse, P., Robert, F. & Govare, É. (2011). Late Pleistocene–Early Holocene Decay of the Laurentide Ice Sheet in Québec–Labrador. *Developments in Quaternary Sciences*, 601–630. https://doi.org/10.1016/b978-0-444-53447-7.00047-7

Ojala, A. E. K., Mattila, J., Markovaara-Koivisto, M., Ruskeeniemi, T., Palmu, J.-P. & Sutinen, R. (2019). Distribution and morphology of landslides in northern Finland: An analysis of postglacial seismic activity. *Geomorphology, 326,* 190-201 https://doi.org/10.1016\/j.geomorph.2017.08.045

Olesen, O., Dehls, J., Bungum, H., Riis, F., Hicks, E., Lindholm, C., Blikra, L., Fjeldskaar, W., Olsen, L., Longva, O., Faleide, J., Bockmann, L., Rise, L., Roberts, D., Braathen, A. & Brekke, H. (2000). *Neotectonics in Norway, Final Report*. https://www.ngu.no/filearchive/156/2000_002.pdf

Olesen, O., Blikra, L. H., Braathen, A., Dehls, J. F., Olsen, L., Rise, L., Roberts, D., Riis, F., Faleide, J. I. & Anda, E. (2003). Neotectonic deformation in Norway and its implications: a review. *Norwegian Journal of Geology*, *Vol. 84*, pp. 3-34. Trondheim 2004. ISSN 029-196X. https://www.researchgate.net/publication/252150448_Neotectonics_in_Norway_-_A_review

Olesen, O., Bungum, H., Dehls, J., Lindholm, C., Pascal, C. & Roberts, D. (2013). *Neotectonics, seismicity and contemporary stress field in Norway - mechanisms and implications*. https://www.ngu.no/upload/Publikasjoner/Special%20publication/SP13_s145-173.pdf

Palmu, J-P., Ojala, A. E.K., Ruskeeniemi, T., Sutinen, R. & Mattila, J. (2015). LiDAR DEM detection and classification of postglacial faults and seismically-induced landforms in Finland: a paleoseismic database, *GFF*, *137:4*, 344-352, DOI: 10.1080/11035897.2015.1068370

Peck, R. B., Hanson, W. E. & Thornburn, T. H. (1974). *Foundation Engineering* (2.ed.). Wiley.

Poutanen, M., Dransch, D., Gregersen, S., Haubrock, S., Ivins, E. R., Klemann, V., Kozlovskaya, E., Kukkonen, I., Lund, B., Lunkka, J.-P., Milne, G., Müller, J., Pascal, C., Pettersen, B. R., Scherneck, H.-G., Steffen, H., Vermeersen, B. & Wolf, D. (2009). DynaQlim – Upper Mantle Dynamics and Quaternary Climate in Cratonic Areas. *New Frontiers in Integrated Solid Earth Sciences*, 349–372. https://doi.org/10.1007/978-90-481-2737-5_10

Ramberg, I. B. & Norsk geologisk forening. (2013). *Landet blir til : Norges geologi* (2. utg., p. 655). Norsk geologisk forening.

Rombouts, J. (2006*Application of airborne LiDAR in forestry in north america and scandinavia*. Gottenstein fellowship report. https://www.researchgate.net/publication/240639335_APPLICATION_OF_AIRBORNE_LiDAR_IN_FORESTRY_IN_NORTH_AMERICA_AND_SCANDINAVIA

Rød, J. K. (2015). *GIS: Verktøy for å forstå verden.* Vigmostad og Bjørke

Scheiber, T., Fredin, O., Viola, G., Jarna, A., Gasser, D. & Łapińska-Viola, R. (2015) Manual extraction of bedrock lineaments from high resolution LiDAR data: methodological

bias and human perception, *GFF, 137:4*, 362-372, DOI: 10.1080/11035897.2015.1085434
SGU. (2016). *Jordskred och raviner*. https://apps.sgu.se/kartvisare/kartvisare-skred.html
Simms, A. R., Lisiecki, L., Gebbie, G., Whitehouse, P. L. & Clark, J. F. (2019). Balancing the last glacial maximum (LGM) sea-level budget. *Quaternary Science Reviews*, *205*, 143–153. https://doi.org/10.1016/j.quascirev.2018.12.018
Smith, M.J. & Clark, C.D. (2005). Methods for the visualization of digital elevation models for landform mapping. Earth Surf. Process. *Landforms*, *30*: 885-900. https://doi.org/10.1002/esp.1210
Smith, C.A., Sundh, M. & Mikko, H. (2014). Surficial geology indicates early Holocene faulting and seismicity, central Sweden. *Int J Earth Sci (Geol Rundsch) 103*, 1711–1724. https://doi.org/10.1007/s00531-014-1025-6
Sollid, J. L. & Sørbel, L. (1994). Distribution of Glacial Landforms in Southern Norway in Relation to the Thermal Regime of the Last Continental Ice Sheet. *Geografiska Annaler: Series A, Physical Geography, 76(1-2)*, 25–35. doi:10.1080/04353676.1994.11880403
Sollid, J. L., Andersen, S., Hamre, N., Kjeldsen, O., Salvigsen, O., Sturød, S., Tveitå, T. & Wilhelmsen, A. (1973) Deglaciation of Finnmark, North Norway, *Norsk Geografisk Tidsskrift - Norwegian Journal of Geography, 27:4*, 233-325, DOI: 10.1080/00291951.1973.9728306
Store Norske Leksikon. (2020a, October 14). *Brumunddal*. Store Norske Leksikon. https://snl.no/Brumunddal
Store Norske Leksikon. (2020b, February 6). *Ringsaker*. Store Norske Leksikon. https://snl.no/Ringsaker
Stroeven, A. P., Hättestrand, C., Kleman, J., Heyman, J., Fabel, D., Fredin, O., Goodfellow, B. W., Harbor, J. M., Jansen, J. D., Olsen, L., Caffee, M. W., Fink, D., Lundqvist, J., Rosqvist, G. C., Strömberg, B. & Jansson, K. N. (2016). Deglaciation of Fennoscandia. *Quaternary Science Reviews*, *147*, 91–121. https://doi.org/10.1016/j.quascirev.2015.09.016
Su, Y., Guo, Q., Fry, D. L., Collins, B. M., Kelly, M., Flanagan, J. P. & Battles. J. J. (2016) A Vegetation Mapping Strategy for Conifer Forests by Combining Airborne LiDAR Data and Aerial Imagery, *Canadian Journal of Remote Sensing, 42:1,* 1-15, DOI: 10.1080/07038992.2016.1131114
Sulebak, J. R. (2014). *Landformer og prosesser: en innføring i naturgeografiske tema* (2. edition.). Vigmostad og Bjørke
Talwani, P . (2014, May 6). *Intraplate Earthquakes*. Cambridge University Press. https://www.researchgate.net/publication/263761075_Intraplate_Earthquakes
Teixeira, S. (2016). Qualitative Geographic Information Systems (GIS): An untapped research approach for social work. *Qualitative Social Work: Research and Practice*, *17*(1), 9–23. https://doi.org/10.1177/1473325016655203
Utdanningsdirektoratet. (2006). *Læreplan i geografi - fellesfag i studieførebuande utdanningsprogram (GEO1-01)*. Udir.no. https://www.udir.no/kl06/GEO1-01/Hele/Kompetansemaal/etter-vg1vg2#
Utdanningsdirektoratet. (2020/2021). *Kompetansemål - Læreplan i geografi - fellesfag i studieførebuande utdanningsprogram (GEO01-02)*. Udir.no. https://www.udir.no/lk20/geo01-02/kompetansemaal-og-vurdering/kv49
Varnes, D. J. (1958). Landslide types and processes. *Landslides and engineering practice*, *24*, 20-47.
Varnes, D. J. (1978). Slope movement types and processes. *Special report*, *176*, 11-33.

Verbovšek, T., Košir, A., Teran, M., Zajc, M. & Popit, T. (2017). Volume determination of the Selo landslide complex (SW Slovenia): integrating field mapping, ground penetrating radar and GIS approaches. *Landslides*, *14*(3), 1265–1274. https://doi.org/10.1007/s10346-017-0815-x

Wentworth, C. (1922). A Scale of Grade and Class Terms for Clastic Sediments. *The Journal of Geology, 30*(5), 377-392. Retrieved April 28, 2021, from http://www.jstor.org/stable/30063207

Wold, M. & Sandven, R. (2016). *Regler for klassifisering av jord Klassifisering i felt*. http://ngf.no/wp-content/uploads/2016/09/13.-Wold-Klassifisering-i-felt.pdf

Wolf, D. (1993). The changing role of the lithosphere in models of glacial isostasy: a historical review. *Global and Planetary Change*, *8*(3), 95–106. https://doi.org/10.1016/0921-8181(93)90017-i

Wood, M. R. (1993) A Review of the Seismotectonics of Sweden.Swedish Nuclear Fuel and Waste Management Co. (SKB) *Technical Report 93-13*. 225 pp.

Wu, P. & Johnston, P. (2000). Can deglaciation trigger earthquakes in N. America? *Geophysical Research Letters*, *27*(9), 1323–1326. https://doi.org/10.1029/1999gl011070

Chapter 9 Appendix 1

Tabell 1 Percentage of each sediment category in all samples collected. The finest sieve used in sieving by NGU was 500µ resulting in a combined class of approximately fine sand, silt and clay. The samples sieved specifically for this thesis had a lower boundary of 65µ, resulting in clay and silt combined in one class. The categorisation of sediment fraction is based upon the Wenthworth grain size classification for sediments (Wenthworth, 1922) 3

Tabell 2 Values from sieving analysis of sample 1.1.1 and Px-, Cx- and Fx-values..... 4

Tabell 3 Approximation of the D10, D30. D50, and D60 values read from the chart. Uniformity coefficient and coefficient of curvature calculated from the D values 4

Tabell 4 Values from sieving analysis of sample 1.2.1 and Px-, Cx- and Fx-values..... 5

Tabell 5 Approximation of the D10, D30. D50, and D60 values read from the chart. Uniformity coefficient and coefficient of curvature calculated from the D values 5

Tabell 6 Values from sieving analysis of sample 1.3.1 and Px-, Cx- and Fx-values..... 6

Tabell 7 Approximation of the D10, D30. D50, and D60 values read from the chart. Uniformity coefficient and coefficient of curvature calculated from the D values. 6

Tabell 8 Values from sieving analysis of sample 2.3.2 and Px-, Cx- and Fx-values..... 7

Tabell 9 Approximation of the D10, D30. D50, and D60 values read from the chart. Uniformity coefficient and coefficient of curvature calculated from the D values 7

Tabell 10 Values from sieving analysis of sample 2.1.3 and Px-, Cx- and Fx-values..... 8

Tabell 11 Approximation of the D10, D30. D50, and D60 values read from the chart. Uniformity coefficient and coefficient of curvature calculated from the D values 8

Tabell 12 Approximation of the D10, D30. D50, and D60 values read from the chart. Uniformity coefficient and coefficient of curvature calculated from the D values. 9

Tabell 13 Values from sieving analysis of sample 2.2.3 and Px-, Cx- and Fx-values..... 9

Tabell 14 Values from sieving analysis of sample 4.1.4 and Px-, Cx- and Fx-values..... 10

Tabell 15 Approximation of the D10, D30. D50, and D60 values read from the chart. Uniformity coefficient and coefficient of curvature calculated from the D values 10

Tabell 16 Values from sieving analysis of sample 80775and Px-, Cx- and Fx-values..... 11

Tabell 17 Approximation of the D10, D30. D50, and D60 values read from the chart. Uniformity coefficient and coefficient of curvature calculated from the D values. 11

Tabell 18 Values from sieving analysis of sample 80776 and Px-, Cx- and Fx-values..... 12

Tabell 19 Approximation of the D10, D30. D50, and D60 values read from the chart. Uniformity coefficient and coefficient of curvature calculated from the D values 12

Tabell 20 Values from sieving analysis of sample 80778 and Px-, Cx- and Fx-values..... 13

Tabell 21 Approximation of the D10, D30. D50, and D60 values read from the chart. Uniformity coefficient and coefficient of curvature calculated from the D values. 13

Tabell 22 Values from sieving analysis of sample 80779 and Px-, Cx- and Fx-values..... 14

Tabell 23 Approximation of the D10, D30. D50, and D60 values read from the chart. Uniformity coefficient and coefficient of curvature calculated from the D values. 14

Tabell 1 Percentage of each sediment category in all samples collected. The finest sieve used in sieving by NGU was 500µ resulting in a combined class of approximately fine sand, silt and clay. The samples sieved specifically for this thesis had a lower boundary of 65µ, resulting in clay and silt combined in one class. The categorisation of sediment fraction is based upon the Wenthworth grain size classification for sediments (Wenthworth, 1922)

		2µ	75µ	425µ	2mm	4,75mm	80mm	300mm				
				Fine	Medium	Coarse						
		Clay	Silt	Sand			Gravel	Coble	Boulder		Silt/clay	Sand	Gravel
1.1.1	Host	21.3%		31.7%	15.5%	8.2%	23.3%	-		100.0%	21.3%	55.4%	23.3%
1.2.1	Host and deposition	16.0%		29.3%	21.1%	9.9%	23.6%	-		100.0%	16.0%	60.4%	23.6%
1.3.1	Deposition	5.6%		41.2%	39.5%	12.3%	1.4%	-		100.0%	5.6%	93.0%	1.4%
2.1.3	Deposition	22.5%		42.9%	22.3%	6.0%	6.3%	-		100.0%	22.5%	71.3%	6.3%
2.2.3	Deposition	21.6%		26.1%	13.4%	10.0%	28.9%	-		100.0%	21.6%	49.5%	28.9%
2.3.2	Host	20.7%		45.6%	12.6%	5.3%	15.9%	-		100.0%	20.7%	63.5%	15.9%
4.1.4	Host	15.9%		29.6%	15.9%	11.1%	27.4%	-		100.0%	15.9%	56.7%	27.4%
OF-PUTTEN-S-20-01	-	-		30.4%	14.3%	8.7%	46.7%	-		100.0%	-	53.3%	46.7%
OF-ÅSDAL-20-01	-	-		70.3%	10.0%	4.6%	15.1%	-		100.0%	-	84.9%	15.1%
OF-ÅSDAL-20-02	-	-		62.8%	13.0%	5.6%	18.7%	-		100.0%	-	81.3%	18.7%
OF-GÅSBUSÆTRA-20-01	-	-		55.0%	16.0%	6.2%	22.8%	-		100.0%	-	77.2%	22.8%

Tabell 2 Values from sieving analysis of sample 1.1.1 and Px-, Cx- and Fx-values

	Sample #:	1.1.1	% not on the sieve	% retained on the sieve	Cumulative % retained	% finer
Sieve #	mm	(SW)gram	(1- SW/W) *100	Px= SW/W *100	Cx=Px+Px+ Px	Fx=W-Cx
S1	16	9	98.2%	1.8%	1.8%	98.2%
S2	8	52	89.8%	10.2%	11.9%	88.1%
S3	4	58	88.7%	11.4%	23.3%	76.7%
S4	2	42	91.8%	8.2%	31.5%	68.5%
S5	1	36	93%	7.1%	38.6%	61.5%
S6	0.5	43	91.6%	8.4%	47%	53.0%
S7	0.25	55	89.2%	10.8%	57.7%	42.3%
S8	0.125	60	88.3%	11.7%	69.5%	30.5%
S9	0.065	47	90.8%	9.2%	78.7%	21.3%
S10	0.001	109	78.7%	21.3%	100%	0%
W	total	511	0%	100%		
				Fineness modulus: 4.6		

Tabell 3 Approximation of the D10, D30. D50, and D60 values read from the chart. Uniformity coefficient and coefficient of curvature calculated from the D values

1.1.1	X	Y
≈D_{10}	0.008	10%
≈D_{30}	0.12	30%
≈D_{50}	0.4	50%
≈D_{60}	0.92	60%
C_u	C_c	
Uniformity coeficiant	Coefficient of cuvature	
$C_u = D_{60}/ D_{10}$	$C_c = (D_{30}^2)/ D_{10} * D_{60}$	
114.5	2.1	

Tabell 4 Values from sieving analysis of sample 1.2.1 and Px-, Cx- and Fx-values

Sieve #	Sample #: mm	1.2.1 (SW)gram	% not on the sieve (1-SW/W)*100	% retained on the sieve Px= SW/W *100	cumulative % retained Cx=Px+Px+Px	% finer Fx=W-Cx
S1	16	27	94.9%	5.1%	5.1%	94.9%
S2	8	42	92. %	8%	13.1%	86.9%
S3	4	55	89.5%	10.5%	23.6%	76.4%
S4	2	52	90.1%	9.9%	33.5%	66.5%
S5	1	58	89%	11.1%	44.6%	55.4%
S6	0.5	53	89.9%	10.1%	54.7%	45.3%
S7	0.25	59	88.8%	11.2%	65.9%	34.1%
S8	0.125	55	89.5%	10.5%	76.4%	23.6%
S9	0.065	40	92.4%	7.6%	84%	16%
S10	0.001	84	84%	16%	100%	0%
W	total	525	0%	100%		
				Fineness modulus: 5.0		

Tabell 5 Approximation of the D10, D30. D50, and D60 values read from the chart. Uniformity coefficient and coefficient of curvature calculated from the D values

1.2.1	X	Y
≈D_{10}	0.02	10%
≈D_{30}	0.20	30%
≈D_{50}	0.7	50%
≈D_{60}	1.41	60%
C_u	C_c	
Uniformity Coefficient	Coefficient of cuvature	
$C_u = D_{60}/ D_{10}$	$C_c = (D_{30}^2)/ D_{10}* D_{60}$	
Cu=d60/d10	Cc=(d30^2)/d10*d60	
94.22	1.91	

Tabell 6 Values from sieving analysis of sample 1.3.1 and Px-, Cx- and Fx-values

	Sample #:	1.3.1	% not on the sieve	% retained on the sieve	cumulative % retained	% finer
Sieve #	mm	(SW)gram	(1-SW/W)*100	Px= SW/W *100	Cx=Px+Px+Px	Fx=W-Cx
S1	16	0	100.%	0%	0%	100%
S2	8	0	100.%	0%	0%	100%
S3	4	5	98.6%	1.4%	1.4%	98.6%
S4	2	44	87.7%	12.3%	13.7%	86.3%
S5	1	103	71.2%	28.9%	42.6%	57.4%
S6	0.5	38	89.4%	10.6%	53.2%	46.8%
S7	0.25	106	70.3%	29.7%	82.9%	17.1%
S8	0.125	28	92.2%	7.8%	90.8%	9.2%
S9	0.065	13	96.4%	3.6%	94.4%	5.6%
S10	0.001	20	94.4%	5.6%	100%	0%
W	total	357	0%	100%		
				Fineness modulus: 4.8		

Tabell 7 Approximation of the D10, D30. D50, and D60 values read from the chart. Uniformity coefficient and coefficient of curvature calculated from the D values.

1.3.1	X	Y
≈D_{10}	0.1371019	10%
≈D_{30}	0.3587066	30%
≈D_{50}	0.596	50%
≈D_{60}	1.0894281	60%
C_u	C_c	
Uniformity Coefficient	Coefficient of cuvature	
$C_u = D_{60}/ D_{10}$	$C_c = (D_{30}^2)/ D_{10}* D_{60}$	
794.6%	86.1%	

Tabell 8 Values from sieving analysis of sample 2.3.2 and Px-, Cx- and Fx-values

	Sample #:	2.3.2	% not on the sieve	% retained on the sieve	cumulative % retained	% finer
Sieve #	mm	(SW)gram	(1-SW/W)*100	Px= SW/W *100	Cx=Px+Px+Px	Fx=W-Cx
S1	16	7	98.2%	1.7%	1.8%	98.2%
S2	8	31	92.2%	7.8%	9.6%	90.4%
S3	4	25	93.7%	6.3%	15.9%	84.1%
S4	2	21	94.7%	5.3%	21.2%	78.8%
S5	1	22	94.5%	5.5%	26.7%	73.3%
S6	0.5	28	93%	7.1%	33.8%	66.3%
S7	0.25	46	88.4%	11.6%	45.3%	54.7%
S8	0.125	68	82.9%	17.1%	62.5%	37.5%
S9	0.065	67	83.1%	16.9%	79.4%	20.7%
S10	0.001	82	79.4%	20.7%	100%	0%
W	total	397	0%	100%		
				Fineness modulus: 4		

Tabell 9 Approximation of the D10, D30. D50, and D60 values read from the chart. Uniformity coefficient and coefficient of curvature calculated from the D values

2.3.2	X	Y
≈D_{10}	0.01	10%
≈D_{30}	0.11	30%
≈D_{50}	0.20	50%
≈D_{60}	0.37	60%
C_u	C_c	
Uniformity Coefficient	Coefficient of cuvature	
$C_u = D_{60}/ D_{10}$	$C_c = (D_{30}^2)/ D_{10}* D_{60}$	
40.6	3.7	

Tabell 10 Values from sieving analysis of sample 2.1.3 and Px-, Cx- and Fx-values

	Sample #:	2.1.3	% not on the sieve	% retained on the sieve	cumulative % retained	% finer
Sieve #	mm	(SW)gram	(1-SW/W)*100	Px= SW/W *100	Cx=Px+Px+Px	Fx=W-Cx
S1	16	0	100%	0%	0%	100%
S2	8	10	97.9%	2.1%	2.1%	97.9%
S3	4	20	95.8%	4.2%	6.3%	93.8%
S4	2	29	94%	6%	12.3%	87.7%
S5	1	43	91%	9%	21.3%	78.8%
S6	0.5	64	86.7%	13.3%	34.6%	65.4%
S7	0.25	74	84.6%	15.4%	50%	50%
S8	0.125	74	84.6%	15.4%	65.4%	34.6%
S9	0.065	58	87.9%	12.1%	77.5%	22.5%
S10	0.001	108	77.5%	22.5%	100%	0%
W	total	480	0%	100%		
				Fineness modulus: 3.7		

Tabell 11 Approximation of the D10, D30. D50, and D60 values read from the chart. Uniformity coefficient and coefficient of curvature calculated from the D values

2.1.3	X	Y
$\approx D_{10}$	0.01	10%
$\approx D_{30}$	0.10	30%
$\approx D_{50}$	0.26	50%
$\approx D_{60}$	0.41	60%
C_u	C_c	
Uniformity Coefficient	Coefficient of cuvature	
$C_u = D_{60}/ D_{10}$	$C_c = (D_{30}^2)/ D_{10} * D_{60}$	
55.0	3.4	

Tabell 13 Values from sieving analysis of sample 2.2.3 and Px-, Cx- and Fx-values.

Sieve #	Sample #: mm	2.2.3 (SW)gram	% not on the sieve (1-SW/W)*100	% retained on the sieve Px= SW/W *100	cumulative % retained Cx=Px+Px+Px	% finer Fx=W-Cx
S1	16	21	95.9%	4.1%	4.1%	95.9%
S2	8	55	89.2%	10.8%	14.9%	85.1%
S3	4	71	86.1%	14%	28.9%	71.1%
S4	2	51	90%	10%	38.9%	61.1%
S5	1	35	93.1%	6.9%	45.8%	54.2%
S6	0.5	33	93.5%	6.5%	52.3%	47.7%
S7	0.25	42	91.8%	8.3%	60.5%	39.5%
S8	0.125	49	90.4%	9.6%	70.1%	29.9%
S9	0.065	42	91.8%	8.3%	78.4%	21.6%
S10	0.001	110	78.4%	21.6%	100%	0%
W	total	509	0%	100%		
				Fineness modulus: 4.9		

Tabell 12 Approximation of the D10, D30. D50, and D60 values read from the chart. Uniformity coefficient and coefficient of curvature calculated from the D values.

2.2.3	X	Y
≈D_{10}	0.01	10%
≈D_{30}	0.13	30%
≈D_{50}	0.6	50%
≈D_{60}	1.84	60%
C_u	C_c	
Uniformity Coefficient	Coefficient of cuvature	
$C_u = D_{60}/ D_{10}$	$C_c = (D_{30}^2)/ D_{10} * D_{60}$	
245.3	1.2	

Tabell 14 Values from sieving analysis of sample 4.1.4 and Px-, Cx- and Fx-values.

Sieve #	Sample #:	4.1.4	% not on the sieve	% retained on the sieve	cumulative % retained	% finer
	mm	(SW)gram	(1-SW/W)*100	Px= SW/W *100	Cx=Px+Px+Px	Fx=W-Cx
S1	16	7	96.8%	1.4%	1.4%	98.6%
S2	8	54	89.1%	10.9%	12.3%	87.7%
S3	4	75	84.9%	15.1%	27.4%	72.6%
S4	2	55	88.9%	11.1%	38.5%	61.5%
S5	1	41	91.7%	8.3%	46.8%	53.2%
S6	0.5	38	92.3%	7.7%	54.4%	45.6%
S7	0.25	54	89.1%	10.9%	65.3%	34.7%
S8	0.125	50	89.9%	10.1%	75.4%	24.6%
S9	0.065	43	91.3%	8.7%	84.1%	15.9%
S10	0.001	79	84.1%	15.9%	100%	0%
W	total	496	0%	100%		
				Fineness modulus: 5.1		

Tabell 15 Approximation of the D10, D30. D50, and D60 values read from the chart. Uniformity coefficient and coefficient of curvature calculated from the D values .

4.1.4	X	Y
≈D_{10}	0.02	10%
≈D_{30}	0.19	30%
≈D_{50}	0.70	50%
≈D_{60}	1.82	60%
C_u	C_c	
Uniformity Coefficient	Coefficient of cuvature	
$C_u = D_{60}/ D_{10}$	$C_c = (D_{30}^2)/ D_{10}* D_{60}$	
121.3	1.4	

Tabell 16 Values from sieving analysis of sample 80775and Px-, Cx- and Fx-values.

		80775				
	Sample #:	OF-PUTTEN-S-20-01	% not on the sieve	% retained on the sieve	cumulative % retained	% finer
Sieve #	mm	(SW)gram	(1-SW/W)*100	Px= SW/W *100	Cx=Px+Px+Px	Fx=W-Cx
S1	22	672.66	85.5%	14.5%	14.5%	85.5%
S2	19	146.42	96.9%	3.2%	17.6%	82.4%
S3	16	165.34	96.4%	3.6%	21.2%	78.8%
S4	8	641.76	86.2%	13.8%	35%	65%
S5	4	539.98	88.4%	11.6%	46.7%	53.3%
S6	2	401.91	91.3%	8.7%	55.3%	44.7%
S7	1	273.70	94.1%	5.9%	61.2%	38.8%
S8	0.5	389.34	91.6%	8.4%	69.6%	30.4%
S9	0.001	1412.26	69.6%	30.4%	100%	0%
W	total	4643.37	0%	100%		
				Fineness modulus: 4.2		

Tabell 17 Approximation of the D10, D30. D50, and D60 values read from the chart. Uniformity coefficient and coefficient of curvature calculated from the D values.

80775	X	Y
$\approx D_{10}$	0.01	10%
$\approx D_{30}$	0.48	30%
$\approx D_{50}$	3.00	50%
$\approx D_{60}$	6.28	60%
C_u	C_c	
Uniformity Coefficient	Coefficient of cuvature	
$C_u = D_{60}/ D_{10}$	$C_c = (D_{30}^2)/ D_{10} * D_{60}$	
785.2	4.6	

Tabell 18 Values from sieving analysis of sample 80776 and Px-, Cx- and Fx-values

	80776					
	Sample #:	OF-ÅSDAL-20-01	% not on the sieve	% retained on the sieve	Cumulative % retained	% finer
Sieve #	mm	(SW)gram	(1-SW/W)*100	Px= SW/W *100	Cx=Px+Px+Px	Fx=W-Cx
S1	22		100%	0%	0%	100%
S2	19		100%	0%	0%	100%
S3	16	17.53	95.4%	4.7%	4.7%	95.4%
S4	8	18.58	95.1%	4.9%	9.6%	90.4%
S5	4	20.65	94.5%	5.5%	15.1%	84.9%
S6	2	17.51	95.4%	4.7%	19.7%	80.3%
S7	1	16.55	95.6%	4.4%	24.1%	75.9%
S8	0.5	20.96	94.4%	5.6%	29.7%	70.3%
S9	0.001	264.92	29.7%	70.3%	100%	0%
S10	<					
W	total	376.70	0%	100%		
				Fineness modulus: 2.028059464		

Tabell 19 Approximation of the D10, D30. D50, and D60 values read from the chart. Uniformity coefficient and coefficient of curvature calculated from the D values

80776	X	Y
≈D_{10}	0.00	10%
≈D_{30}	0.01	30%
≈D_{50}	0.08	50%
≈D_{60}	0.20	60%
C_u	C_c	
Uniformity Coefficient	Coefficient of cuvature	
$C_u = D_{60}/ D_{10}$	$C_c = (D_{30}^2)/ D_{10}* D_{60}$	
80.00	0.34	

Tabell 20 Values from sieving analysis of sample 80778 and Px-, Cx- and Fx-values.

		80778				
	Sample #:	OF-ÅSDAL-20-02	% not on the sieve	% retained on the sieve	cumulative % retained	% finer
Sieve #	mm	(SW)gram	(1-SW/W)*100	Px= SW/W *100	Cx=Px+Px+Px	Fx=W-Cx
S1	22	117.8	94.7%	5.3%	5.3%	94.7%
S2	19	55.02	97.5%	2.5%	7.8%	92.2%
S3	16	23.43	98.9%	1.1%	8.9%	91.1%
S4	8	100.15	95.5%	4.5%	13.4%	86.6%
S5	4	116.51	94.7%	5.3%	18.7%	81.4%
S6	2	123.22	94.4%	5.6%	24.2%	75.8%
S7	1	135.29	93.9%	6.1%	30.3%	69.7%
S8	0.5	151.93	93.1%	6.9%	37.2%	62.8%
S9	0.001	1389.98	37.2%	62.8%	100%	0%
S10						
W	total	2213.29	0%	100%		
				Fineness modulus: 2.5		

Tabell 21 Approximation of the D10, D30. D50, and D60 values read from the chart. Uniformity coefficient and coefficient of curvature calculated from the D values.

80778	X	Y
≈D_{10}	0.00	10%
≈D_{30}	0.02	30%
≈D_{50}	0.14	50%
≈D_{60}	0.38	60%
C_u	C_c	
Uniformity Coefficient	Coefficient of cuvature	
$C_u = D_{60}/ D_{10}$	$C_c = (D_{30}^2)/ D_{10} * D_{60}$	
140.00	0.32	

Tabell 22 Values from sieving analysis of sample 80779 and Px-, Cx- and Fx-values.

		80779				
	Sample #:	OF-GÅSBUSÆTRA-20-01	% not on the sieve	% retained on the sieve	cumulative % retained	% finer
Sieve #	mm	(SW)gram	(1-SW/W) *100	Px= SW/W *100	Cx=Px+Px+Px	Fx=W-Cx
S1	22	166.2	94.4%	5.6%	5.6%	94.4%
S2	19	58.37	98%	2%	7.6%	92.4%
S3	16	71.76	97.6%	2.4%	10%	90%
S4	8	203.75	93.1%	6.9%	16.8%	83.2%
S5	4	178.63	94%	6%	22.8%	77.2%
S6	2	183.73	93.8%	6.2%	29%	71%
S7	1	202.93	93.2%	6.8%	35.9%	64.1%
S8	0.5	272.29	90.8%	9.2%	45%	55%
S9	0.001	1634.31	45%	55%	100%	0%
S10						
W	total	2971.96	0%	100%		
				Fineness modulus: 2.7		

Tabell 23 Approximation of the D10, D30. D50, and D60 values read from the chart. Uniformity coefficient and coefficient of curvature calculated from the D values.

80779	X	Y
≈D_{10}	0.00	10%
≈D_{30}	0.03	30%
≈D_{50}	0.30	50%
≈D_{60}	0.77	60%
C_u	C_c	
Uniformity Coefficient	Coefficient of cuvature	
$C_u = D_{60}/ D_{10}$	$C_c = (D_{30}^2)/ D_{10} * D_{60}$	
241.71	0.36	

Einar T T Rufsvoll

Landslides in Brumunddalen Area, Norway; Evidence of Post-Glacial Earthquakes - A GIS and Field Study

NTNU
Norwegian University of
Science and Technology